Tests of the Charged Weak Current in Correlated Hadronic τ Decays Using L3 at LEP

James A. Gerald

A thesis submitted to

The Johns Hopkins University

in conformity with the requirements for the degree of

Doctor of Philosophy

Baltimore, MD

1995

Abstract

With a sample of 86,000 $Z \to \tau^+\tau^-(\gamma)$ events collected with the L3 detector at LEP in 1991, 1992, and 1993, we have measured the hadronic chirality parameter (ξ_h) using a subsample of 22,500 events with a π and/or ρ in the final state. We exploit for this analysis the energy spectra of the pion, the decay dynamics of the ρ, and correlations between selected $\pi - \pi$, $\pi - \rho$, and $\rho - \rho$ final states.

We measure $\xi_\pi = -1.005 \pm 0.095 \pm 0.034$ and $\xi_\rho = -0.935 \pm 0.067 \pm 0.020$. Assuming universality, with $\xi_\pi = \xi_\rho \equiv \xi_h$, we obtain $\xi_h = -0.960 \pm 0.051 \pm 0.012$.

Thesis Advisor: Professor Aihud Pevsner

I perceive I have not really understood any thing,
not a single object, and that no man ever can,
Nature here in sight of the sea taking advantage of me
to dart upon me and sting me,
Because I have dared to open my mouth to sing at all.

Walt Whitman

Contents

List of Figures

List of Tables

Chapter 1

Motivation

The construction of the Large Electron-Positron collider (LEP) at CERN has opened many new experimental windows for direct tests of the parity violating nature of the weak currents in the Standard Model (SM) [1]. One such window is the process $e^+e^- \to \mathrm{Z} \to \tau^+\tau^-$, which allows one to directly probe the neutral weak current through the coupling of the Z to the $\tau^+\tau^-$ pair. The charged weak current may also be studied through the correlations in the subsequent decays of the two τ leptons. In particular, by using the hadronic decays of the τ lepton and dropping the assumption of lepton universality, one may measure the average τ neutrino helicity. In the SM, this is a maximally parity violating quantity equal to -1. A result in agreement with the SM supports the notion of lepton universality.

The first clear evidence for parity violation predates the Standard Model. This evidence resulted from an experiment conducted by C. S. Wu *et al.* [2] in 1956 in which they observed asymmetries in the angular distribution of the beta rays from polarized Co^{60} decays. The $\tau - \theta$ puzzle had been the hot topic of debate, centering around the identification of two particles with the same mass and lifetime

but opposite parity [3–8]. After Wu's experiment, this puzzle quickly ceased to exist, and the final states in $K \to \pi\pi$ and $K \to \pi\pi\pi$ were acknowledged as the products of a single particle [9]. The experiment above was soon followed by others [10–12], leading to wide spread acceptance that parity was not a conserved quantity in weak interactions.

Another set of experiments were quickly put together, providing evidence that the neutrino was left-handed [13–15] and flavored [16]. Over a decade later, the discovery of the J/ψ [17, 18] in 1974 and its interpretation as a $c\bar{c}$ pair lead to a picture of the universe consisting of two families of fermions: (u, d, e, ν_e) and (c, s, μ, ν_μ).

In 1975 M. L. Perl *et al.* [19] discovered evidence for yet a third lepton (now dubbed the τ particle) and presumably, through inference, a third neutrino (ν_τ). Another quark (b) in the new generation of particles was soon discovered [20]. With the construction of the DORIS storage ring at DESY and CESR at Cornell, the production of these two fermions and a study of their properties through the reaction $e^+e^- \to \gamma \to f^+f^-$ began in earnest.

The search for the quark partner of the b (the top quark t), the vector gauge bosons of the weak interactions (Z and $W^\pm$), and the Higgs boson (H) proceeded with the construction of the $Sp\bar{p}S$ at CERN. There two collaborations reported the first observations of the decay of the Z and $W^\pm$ [21, 22] in 1982. Both the top and the Higgs remained unobserved, motivating the construction of SLAC at Stanford, LEP at CERN, and the Tevatron at Fermi Lab to search for these last two SM particles and improve the measurements of the Z and $W^\pm$properties.

At Fermi Lab, the top quark has now been discovered [23, 24], and the search for the Higgs continues at all three accelerators. In the mean time, LEP has

been operating at the Z-peak since 1990 and delivering luminosities which allow for precision measurements of the SM parameters. In particular, the production of 86,000 $\tau^+\tau^-$ pairs at the L3 detector at LEP through 1993 makes possible an accurate measurement of the τ neutrino helicity.

This measurement we present in this thesis. We begin with a brief review of the theoretical framework of the SM in Chapter 2. An explanation of the experimental technique used in making the measurement follows in Chapter 3. We described the L3 detector in Chapter 4 and how we discriminate between the different final states of the τ with it in Chapter 5. The measurement of the ν_τ helicity is presented in Chapter 6 and the conclusion of this work in Chapter 7.

Chapter 2

A Theoretical Overview

A complete review of electroweak theory in the SM is a task beyond the scope of this work. We present here a simple overview of the fundamental particles involved and of the electroweak theory in the SM. This is followed by a discussion of polarization in the production of τ pairs at the Z peak and chirality in the decay of the τ. Finally we end with a brief note on radiative corrections.

2.1 Elementary Particles

Within the framework of the SM, the "periodic" table of elementary particles is now almost complete. The three generations of particles listed in table 2.1 seem to be on solid footing with all members present. Direct measurements of the number of light neutrinos from Z decays at LEP [25] support there being only three families within the context of the SM. The gauge bosons of table 2.2 have all been observed with the exception of the Higgs.

Electroweak interactions between the fundamental particles are mediated by

Quarks			Q_f	T_L^3	T_R^3
u	c	t	$\frac{2}{3}$	$\frac{1}{2}$	0
d[1]	s	b	$-\frac{1}{3}$	$-\frac{1}{2}$	0
Leptons			Q_f	T_L^3	T_R^3
e	μ	τ	-1	$-\frac{1}{2}$	0
ν_e	ν_μ	ν_τ	0	$\frac{1}{2}$	–

Table 2.1: The spin $\frac{1}{2}$ fermions, their charge (Q_f), and the third component of weak isospin for their left (T_L^3) and right-handed (T_R^3) components.

the gauge bosons of table 2.2. The weak interactions were initially interpreted as being point–like [26] in low energy interactions. A casual glance at the SM propagator for either the Z or $W^{\pm}$ reveals why. For a virtual $W^{\pm}$ boson, we have the propagator [27–29]

$$\frac{i}{k^2 - m_W^2 + i,\, {}_W m_W} \left(-g^{\mu\nu} + \frac{k^\mu k^\nu}{m_W^2} \right), \tag{2.1}$$

where k^μ represents the four-momenta transferred between particles by the $W^{\pm}$. For small k^2, the second term vanishes, resulting in a point–like interaction.

Precision tests at high k^2 have now been performed both at SLAC and LEP in measurements of the couplings to the Z. The extension of LEP energies to those needed for $W^{\pm}$ pair production will increase our knowledge of the SM couplings. It may also allow us to place a more definite limit on or make a direct measurement of the Higgs mass. If this last element in the gauge boson table is not found at LEP, then the next generation collider, the Large Hadron Collider, may provide the experimental grounds for its detection.

[1]Strictly speaking, the mass eigenstates listed here are not electroweak eigenstates with the

Boson	Charge	Mass	Spin	Propagator
γ	0	0 GeV	1	$-ieQ_f\gamma^\mu$
Z	0	91.2 GeV	1	$\frac{i}{k^2-m_Z^2+i\Gamma_Z m_Z}\left(-g^{\mu\nu}+\frac{k^\mu k^\nu}{m_Z^2}\right)$
$W^\pm$	±1	80.2 GeV	1	$\frac{i}{k^2-m_W^2+i\Gamma_W m_W}\left(-g^{\mu\nu}+\frac{k^\mu k^\nu}{m_W^2}\right)$
H	0	> 60 GeV	0	$\frac{i}{k^2-m_H^2+i\Gamma_H m_H}$

Table 2.2: The electroweak gauge bosons and Higgs.

2.2 Weak Couplings

Weak interactions in an early form were proposed by Fermi as an explanation of β–decay [9, 26, 30]. The theory he developed modeled the decay

$$n \rightarrow p\, e^-\bar{\nu}_e \tag{2.2}$$

as the product of two currents. In terms of the Dirac spinors p, e, n, and $\bar{\nu}_e$ for the proton, neutron, electron and neutrino respectively, this product was

$$T = G_F\,(\bar{n}\gamma^\mu p)\,(\bar{\nu}_e\gamma_\mu e)\,. \tag{2.3}$$

Here G_F is the weak coupling constant, which must be measured.

As was shown by C. S. Wu *et al.* [2], however, the weak charged current does not couple equally to left and right-handed fermions, leading to parity violation. In the context of the SM, the weak charged current is formulated to be maximally parity violating in that it couples exclusively to left-handed fermions. To a lesser extent, the weak neutral current is also parity violating, with unequal couplings for left and right-handed charged fermions.

isospin shown. One must include the weak mixing angles via the CKM matrix to obtain the proper states d', s', and b' [27–29].

In figure 2.1, the Feynman diagrams for $W^{\pm}$ and Z couplings to leptons are shown. For the $W^{\pm}$, we have the vertex term [27, 28]

$$-i\frac{g}{\sqrt{2}}\gamma^{\mu}\frac{1-\gamma_5}{2}. \tag{2.4}$$

For the Z vertex, the coupling to the $\ell\bar{\ell}$ pair is

$$-i\frac{g}{\cos\theta_W}\left\{T_L^3\gamma^{\mu}\frac{1-\gamma_5}{2}-\sin^2\theta_W Q_f\gamma^{\mu}\right\}, \tag{2.5}$$

where the T_L^3 and Q_f are to be taken from table 2.1. The weak mixing angle, θ_W, can be defined by

$$\sin^2\theta_W = 1-\frac{m_W^2}{m_Z^2}, \tag{2.6}$$

and from the low energy limit on the couplings in β-decay, we have the relationship to the Fermi constant

$$\frac{G_F}{\sqrt{2}} = \frac{g^2}{8m_W^2}. \tag{2.7}$$

With the addition of one other constraint, namely,

$$e = g\sin\theta_W = \sqrt{4\pi\alpha}, \tag{2.8}$$

we may express the weak couplings in the SM at tree level in terms of three measurable quantities. One common choice is α[2], G_F, and m_Z. The current values for these quantities are listed in table 2.3. Expressed in terms of these three quantities, $\sin^2\theta_W$ is

$$\sin^2\theta_W = \frac{1}{2}-\sqrt{\frac{1}{4}-\frac{1}{m_Z^2}\left(\frac{\pi\alpha}{\sqrt{2}G_F}\right)}. \tag{2.9}$$

One obtains

$$\sin^2\theta_W = 0.2329 \tag{2.10}$$

[2] α must be measured at $q^2 = m_W$ and is thus not the familiar 1/137.

Parameter	Value
α^{-1}	128.2 ± 0.12 at $q^2 = m_W$
G_F	$(1.16639 \pm 0.00002) \times 10^{-5}$ GeV^{-2}
m_Z	91.187 ± 0.007 GeV

Table 2.3: Measured parameters of the SM from which the weak couplings may be determined [39].

by plugging in the values from the table.

The Z vertex term of equation (2.5) may also be written in terms of its vector and axial–vector components. Here we make the identifications

$$g_V^f = T_L^3 - 2Q_f \sin^2\theta_W \tag{2.11}$$

and

$$g_A^f = T_L^3. \tag{2.12}$$

The Z vertex term we now write as

$$-i\frac{g}{\cos\theta_W}\left\{\gamma^\mu \frac{g_V^f - g_A^f\gamma_5}{2}\right\}. \tag{2.13}$$

The ratio of vector to axial–vector couplings is then

$$\frac{g_V^\ell}{g_A^\ell} = 1 - 4\sin^2\theta_W \tag{2.14}$$

for charged leptons.

2.3 τ Production and Decay

The production of τ–pairs through the process $e^+e^- \to \mathrm{Z} \to \tau^+\tau^-$ at $\sqrt{s} \approx m_Z$ at LEP and SLD has opened a new window on the SM couplings of the weak currents.

This has been exploited by all experiments at LEP using τ's specifically [32–37] to measure g_V^τ/g_A^τ and g_V^e/g_A^e modulo an overall sign ambiguity. Using the left-right production asymmetry at SLD [38], measurements of g_V^e/g_A^e with an unambiguous sign have also been performed.

We present here an outline of measurable quantities of interest to us. Specifically, assuming the neutral weak current involved in τ production takes place only through a massive Z boson via V and A couplings, we show how one may measure the ratio g_V^τ/g_A^τ. Then assuming that the subsequent τ decay proceeds through an off–shell $W^\pm$ to a hadronic final state, we show how one may simultaneously measure the ratio of the vector and axial–vector couplings of the τ to the charged weak current, g_V^c/g_A^c.

2.3.1 Polarization in τ Production

The branching fractions and partial widths for Z decays are listed in table 2.4 [39]. Even though the branching fraction for $Z \to \tau^+\tau^-$ is relatively small (3.36%), the 2.56 million Z's recorded by L3 during the years 1990 through 1993 yield approximately 86,000 τ–pairs.

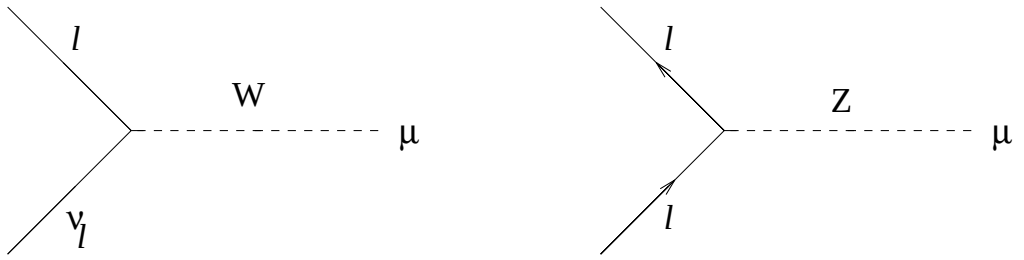

Figure 2.1: Feynman diagrams for $W^\pm$ and Z couplings to leptons.

Fermion pair	$\Gamma_{f\bar{f}}$ (MeV)	$\Gamma_{f\bar{f}}/\Gamma_Z$
e^+e^-	83.83±0.30	3.366±0.008 %
$\mu^+\mu^-$	84.15±0.77	3.367±0.013 %
$\tau^+\tau^-$	83.68±0.44	3.360±0.015 %
$q\bar{q}$	1740.7±5.9	69.90±0.15 %
invisible	498.2±4.2	20.01±0.16 %
total	2490±7	

Table 2.4: The partial widths and decay rates for the Z boson [39].

The Born cross–section for τ production near the Z peak for a given τ^- helicity state h_τ ($h_\tau = \pm 1$) is [40]

$$\sigma_{Born}(s; h_\tau) = F_0(s) - h_\tau F_1(s). \tag{2.15}$$

The form factors F_0 and F_1 are

$$F_0(s) = \frac{4\pi\alpha^2}{3s}\left(Q_e^2 Q_\tau^2 + 2\mathrm{Re}\chi(s) Q_e Q_\tau g_V^e g_V^\tau + |\chi(s)|^2 (g_V^{e\,2} + g_A^{e\,2})(g_V^{\tau\,2} + g_A^{\tau\,2})\right) \tag{2.16}$$

and

$$F_1(s) = \frac{4\pi\alpha^2}{3s}\left(2\mathrm{Re}\chi(s) Q_e Q_\tau g_V^e g_A^\tau + |\chi(s)|^2 (g_V^{e\,2} + g_A^{e\,2}) 2 g_V^\tau g_A^\tau\right), \tag{2.17}$$

where $\sqrt{s}$ is the center–of–mass energy and the dependence on s is given by

$$\chi(s) = \frac{s}{s - m_Z^2 + i s, _Z/m_Z}. \tag{2.18}$$

The first term in equation 2.16 arises from the process $e^+e^- \to \gamma \to \tau^+\tau^-$. The second term arises from $\gamma\cdot$Z interference, and the third is from the $e^+e^- \to$ Z $\to \tau^+\tau^-$ process of interest here.

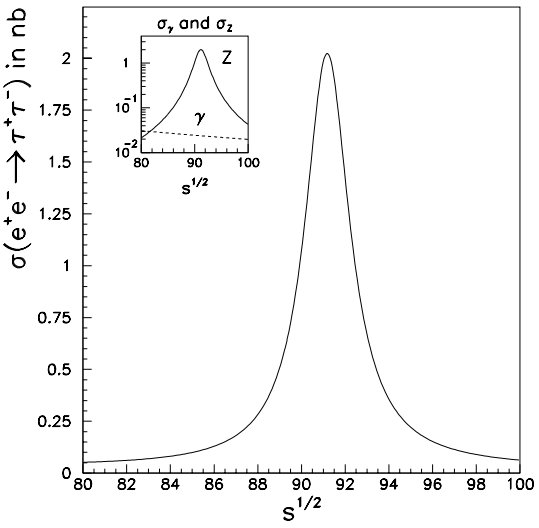

Figure 2.2: The Born cross–section for $e^+e^- \to \tau^+\tau^-$ with the contributions from the Z, γ and Z–γ interference. Here we have assumed $m_Z = 91.2$, , $_Z = 2.5$, and $\sin^2\theta_W = 0.2329$. The inset shows the contributions from the Z and γ separately. The contribution from the interference term is less than 1% over the range shown.

In figure 2.2, we show the total Born cross–section for $e^+e^- \to \tau^+\tau^-$ as a function of $\sqrt{s}$. The contribution from γ exchange and that from Z exchange are plotted separately in the inset. The contribution from the interference term is less than 1% over the range shown. The cross–section from γ exchange becomes approximately 10% of the total at $m_Z \pm$, $_Z$.

The τ polarization, $\mathcal{P}_\tau$, is defined as the production asymmetry between τ^- leptons with positive ($h_\tau = +1$) and negative ($h_\tau = -1$) helicity. The τ^- and τ^+ leptons's helicity states are almost completely anti–correlated in each event with corrections on the order of m_τ^2/m_Z^2; thus, we define $\mathcal{P}_\tau^- = -\mathcal{P}_\tau^+ \equiv \mathcal{P}_\tau$. From

equation (2.15) above, we have

$$\mathcal{P}_\tau = \langle h_\tau \rangle = \frac{\sigma(s;+1) - \sigma(s:-1)}{\sigma(s;+1) + \sigma(s:-1)} = -\frac{F_1(s)}{F_0(s)}. \tag{2.19}$$

In the limit $\sqrt{s} \approx m_Z$ the polarization becomes

$$\mathcal{P}_\tau = -\frac{g_V^\tau g_A^\tau}{{g_V^\tau}^2 + {g_A^\tau}^2} \tag{2.20}$$

where the small contribution from γ exchange has been ignored.

2.3.2 Chirality in Correlated Hadronic τ Decays

The decay structure for a hypothetical heavy lepton was first explored by Yung-Su Tsai [42] a few years before the first observations of the τ by M. Perl *et al.* [19]. Tsai and others [43–46] have shown that hadronic decays of the $\tau^\pm$ lepton may all be written in the form

$$\frac{d,_i}{dx_{h_i}} \propto F_i(x_i) \pm h_{\tau^\pm} \xi_i G_i(x_i), \tag{2.21}$$

where $h_{\tau^\pm}$ is the $\tau^\pm$ helicity and ξ_i is the hadronic chirality parameter for the generic hadronic final state i ($i = \pi$ or ρ). In addition, the $F_i(x_i)$ and $G_i(x_i)$ satisfy the following conditions:

$$\int F_i(x_i) dx_i = 1 \tag{2.22}$$

and

$$\int G_i(x_i) dx_i = 0. \tag{2.23}$$

In the SM, ξ_i is assumed to be exactly -1, in keeping with the purely $V-A$ nature of the charged weak current. Writing the coupling of the τ^- to the W^-

vertex with more general V and A couplings[3] , we have

$$\bar{\nu}_\tau(k_\tau, s'_\tau)\left(\frac{-ig}{\sqrt{2}}\gamma_\nu\frac{(g_V^c - g_A^c\gamma^5)}{2}\right)\tau(p_\tau, s_\tau). \tag{2.24}$$

After some matrix algebra, this yields

$$\xi_i = -\frac{2g_V^c g_A^c}{(g_V^c)^2 + (g_A^c)^2}. \tag{2.25}$$

For massless neutrinos, we interpret this as the average neutrino helicity.

For $\tau^- \to \pi^-\nu_\tau$, the form of the functions $F_i(x_i)$ and $G_i(x_i)$ is particularly simple [42, 44–46], with

$$F_\pi(x_\pi) = 1 \tag{2.26}$$

and

$$G_\pi(x_\pi) = 2x_\pi - 1. \tag{2.27}$$

$x_\pi = E_\pi/E_{beam}$ is the normalized pion energy. The functions F_π and G_π are shown in figure 2.3. For the case of $\tau^- \to \rho^-\nu_\tau$, the distributions F_ρ and G_ρ are more complicated. These we present later in section 3.2.

As can clearly be seen in equation (2.21), it is impossible to disentangle the τ polarization from the hadronic chirality.[4] Thus we turn to correlated decays.

In the case of correlated decays, we form the double–sided decay distribution

$$\frac{d^2, _{ij}}{dx_i dx_j} \propto F_i F_j + \xi_i\xi_j G_i G_j - h_{\tau^-}[\xi_i G_i F_j + \xi_j G_j F_i], \tag{2.28}$$

where we have made use of $h_{\tau^-} = -h_{\tau^+}$. From the above distribution, we can disentangle polarization and chirality up to a sign ambiguity. Aside from exploiting

[3]Except where explicitly stated otherwise, the charge conjugate states are implied throughout this work.

[4]An exception to this is the decay $\tau^- \to a_1\nu_\tau$ [47], in which the dynamics of the a_1 decay allow the τ helicity to be reconstructed event–by–event.

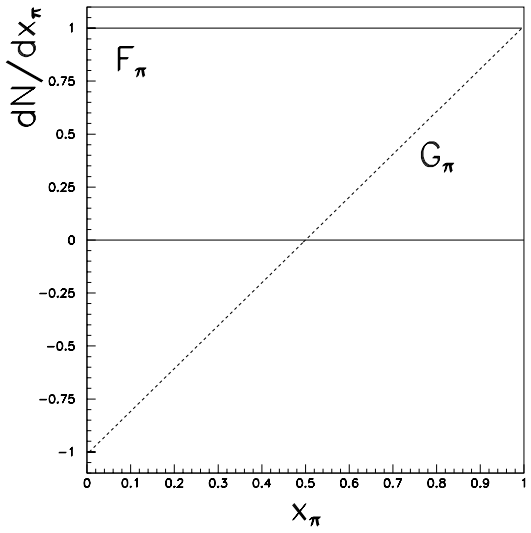

Figure 2.3: The pion decay distributions F_π and G_π versus the normalized pion energy x_π.

the a_1 dynamics, there is no way to resolve this ambiguity with a single measurement.

However, from the SLD measurement of the left–right production asymmetry [38], we know the sign of g_V^e/g_A^e is positive. From the LEP measurements of the forward–backward polarization asymmetry [33–37], we know that g_V^e/g_A^e and g_V^τ/g_A^τ have the same sign, and thus $\mathcal{P}_\tau$ is negative. Thus, using the above distributions, we may unambiguously assign a sign to ξ_h.

2.4 Radiative Corrections

Radiative corrections fall into three basic categories. There are (a) vertex corrections, (b) propagator corrections due to additional terms such as a $t\bar{t}$ loop or Higgs loop, and (c) corrections due to initial and final state radiation of real photons.

The first two categories are lumped together by defining $\sin^2\theta_W$ in terms of the measured values of g_V^τ and g_A^τ at $\sqrt{s} = m_Z$. Thus the meaning of equation (2.14) is reversed, and we define the effective weak mixing angle from

$$1 - 4\sin^2\theta_W^{eff} = \frac{g_V^\ell}{g_A^\ell}. \tag{2.29}$$

Corrections to the propagator and vertex are absorbed into this parameter.

Final state radiation effects are not explicitly taken into account simply because they are simulated in the Monte Carlo and the soft photons produced are usually collinear with the τ decay product and, in a sense, reabsorbed when the final state hadronic energy is measured. Initial state radiation, however, lowers the average observed energy by lowering the center–of–mass of the $e^+e^- \rightarrow Z$ interaction. In addition, initial state photons are emitted along the beam direction and go unobserved. The effect is to push the overall polarization slightly towards more positive values.

Chapter 3

Experimental Technique

Since the discovery of the muon and recognition that it was a heavy lepton [50], attempts have been made to study the differences between electrons and muons. The couplings of the muon to the electron were parameterized by Michel [51] as a set of measurable quantities commonly referred to as the Michel parameters. The measurement of these parameters was the work of decades [52–60], with the conclusion that both the electron and the muon coupled to the weak charged current through a purely $V-A$ interaction.

Ideally, one would like to conduct the same set of tests on the $\tau-\mu$ and $\tau-e$ couplings. Unfortunately this cannot be done. While the muon lifetime of $\tau_\mu \approx 2\times10^{-6}$ s allows one to have muon beams or cool them and bring them to rest with a fixed polarization in a magnet, the τ lifetime of $\tau_\tau \approx 3\times10^{-13}$ s [39] does not. Even at LEP energies, the mean τ decay length is only $\gamma\beta c\tau_\tau \approx 2.3$ mm.

Some tests of the $V-A$ nature of τ decays can be conducted, however, through the final state observables in semi–leptonic (*i.e.* hadronic) and leptonic (*i.e.* electrons and muons) decays of the τ. In the leptonic modes, the Michel parameters

may all be expressed in terms of the chirality parameter under the assumption that the τ decay proceeds only through V and A couplings. Unfortunately, the presence of two undetected neutrinos greatly reduces the sensitivity[1] of the measurement to ξ_h. Thus we do not consider them here.

The two hadronic decays considered here are the $\tau^- \to \pi^-\nu_\tau$ and $\tau^- \to \rho^-\nu_\tau$, with the subsequent decay $\rho^- \to \pi^-\pi^0$. These two channels represent roughly 35% of all τ decays and are the two most sensitive to polarization and chirality. These decays carry polarization information in their final state dynamics. In addition, due to the correlation introduced by the Z decaying into two τ leptons with opposite helicities (modulo $\mathcal{O}(m_\tau^2/m_Z^2)$ corrections), information on the hadronic chirality may be obtained through observing correlations in the dynamics on opposite sides[2] of the event as discussed in section 2.3.2.

Below we discuss the five distinct classes of events used in this measurement. The first is π–X, in which there is a single identified pion on one side of the event and the other side was identified as neither a pion nor a rho. The second is π–π, in which both sides of the event were explicitly identified as pions. The third, ρ–X, is similar to the first, and the fourth and fifth are ρ–ρ and π–ρ.

[1] We quantify sensitivity in section 3.4.

[2] The sides of an event are defined by a plane perpendicular to the thrust axis which passes through the vertex.

3.1 Polarization and Chirality in $\tau^- \to \pi^- \nu_\tau$ and $\tau^+\tau^- \to \pi^+\pi^-\bar{\nu}_\tau\nu_\tau$

The simple kinematics of the decay $\tau^- \to \pi^-\nu_\tau$ make it the most sensitive to polarization and chirality. The spin–0 π^- is mono-energetic in the τ rest frame, and the neutrino carries off all of the angular momentum. Thus we present here a more detailed description of $\tau^- \to \pi^-\nu_\tau$ decay in the absence of radiative corrections.

First consider the four possible amplitudes presented in figure 3.1. The spin of the τ and its neutrino are represented by the large, open arrows. Parts (a) and (c) are the $V-A$ terms of the SM, i.e. the neutrino is left–handed. Parts (b) and (d) represent the two polarization states for right–handed neutrinos. The decay distribution in the τ rest frame for each of the configurations is given by

$$|\mathcal{M}_{+-}|^2 = |\mathcal{M}_{-+}|^2 = \cos^2\frac{\theta}{2}, \tag{3.1}$$

for sub-figures (a) and (d) and

$$|\mathcal{M}_{++}|^2 = |\mathcal{M}_{--}|^2 = \sin^2\frac{\theta}{2}, \tag{3.2}$$

for sub-figures (b) and (c). Here θ is the angle between the line–of–flight of the τ in the lab frame and the π in the τ rest frame, and the first subscript denotes the helicity of the τ^- while the second the helicity of the neutrino.

In the τ rest frame, the total decay distribution is given by

$$\frac{dN}{d\cos\theta} \propto f_\tau^+ \cdot f_{\nu_\tau}^- |\mathcal{M}_{+-}|^2 + f_\tau^+ \cdot f_{\nu_\tau}^+ |\mathcal{M}_{++}|^2 + f_\tau^- \cdot f_{\nu_\tau}^- |\mathcal{M}_{--}|^2 + f_\tau^- \cdot f_{\nu_\tau}^+ |\mathcal{M}_{-+}|^2, \tag{3.3}$$

where $f_\tau^{+(-)}$ is the fraction of τ's with positive (negative) helicity and $f_{\nu_\tau}^{+(-)}$ is the fraction of neutrinos with positive (negative) helicity. The average τ polarization

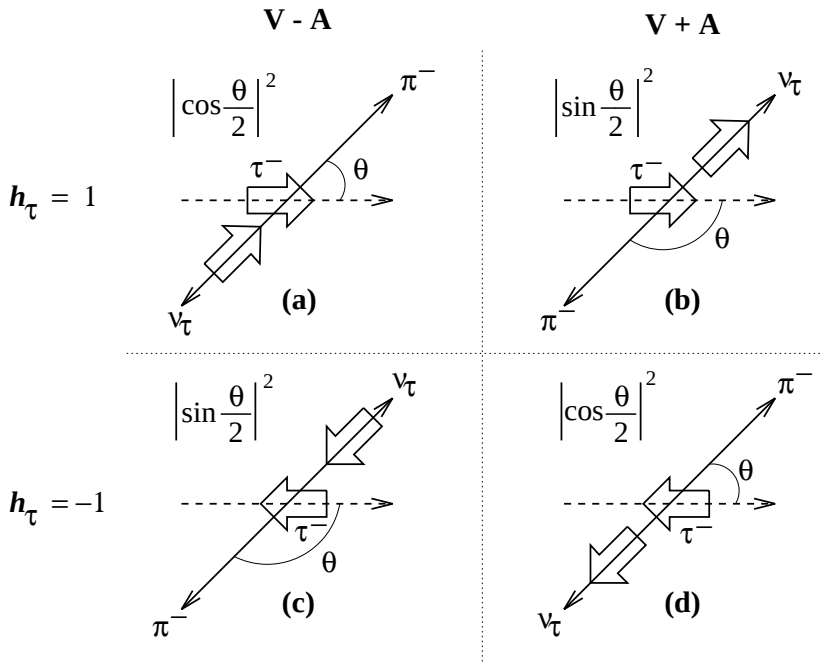

Figure 3.1: The polarization and chirality amplitudes for $\tau^- \to \pi^-\nu_\tau$ are shown for each combination of τ and neutrino helicity. In the figure, the large arrows indicate the spin of the τ or ν_τ. The dashed arrow indicates the direction of the τ in the lab frame. The solid arrows indicate the directions of the π and ν_τ in the τ rest frame. The angular distribution of the π is given for each combination.

is then

$$\mathcal{P}_\tau = f_\tau^+ - f_\tau^-. \tag{3.4}$$

Similarly, the average τ neutrino helicity is given by

$$\xi_\pi = f_{\nu_\tau}^+ - f_{\nu_\tau}^-. \tag{3.5}$$

From equation (3.4) and the condition that $f_\tau^+ + f_\tau^- = 1$, we obtain

$$f_\tau^+ = \frac{1 + \mathcal{P}_\tau}{2} \tag{3.6}$$

and

$$f_\tau^- = \frac{1-\mathcal{P}_\tau}{2}. \tag{3.7}$$

The fractions $f_{\nu_\tau}^+$ and $f_{\nu_\tau}^-$ may also be defined in a similar way in terms of ξ_π.

Expressing the decay rate above as a function of $\mathcal{P}_\tau$ and ξ_π, we have

$$\frac{1}{N}\frac{dN}{d\cos\theta} \approx \frac{1}{2}\left(1 - \mathcal{P}_\tau \xi_\pi \cos\theta\right). \tag{3.8}$$

In the lab frame, the quantity $\cos\theta$ may be written as [30]

$$\cos\theta = \frac{2x - \frac{m_\pi^2}{m_\tau^2} - 1}{(1-\frac{m_\pi^2}{m_\tau^2})(1-\frac{m_\tau^2}{E_{beam}^2})}, \tag{3.9}$$

where $x = E_\pi / E_{beam}$ is the normalized pion energy in the lab frame. However, since $m_\tau \ll m_Z$ and $m_\pi \ll m_\tau$, the above simplifies to the familiar decay distribution

$$\frac{1}{N}\frac{dN}{dx} \approx 1 - \mathcal{P}_\tau \xi_\pi (2x-1). \tag{3.10}$$

As before, we define $F_\pi(x) = 1$ and $G_\pi(x) = 2x - 1$.

When both τ leptons decay to π's, π_1 and π_2 with energies x_1 and x_2 respectively, the correlated decay distribution is

$$\frac{1}{N}\frac{dN}{dx_1 dx_2} \approx 1 - \mathcal{P}_\tau \xi_\pi \left(2x_1 + 2x_2 - 2\right) + \xi_\pi^2 (2x_1 - 1)(2x_2 - 1). \tag{3.11}$$

As discussed earlier, the two–dimensional distribution above provides sensitivity to the chirality parameter that the one–sided distribution does not. Shown in figure 3.2 are two possible distributions. In the distribution on the left, both τ's always decay via a $V-A$ current. In the distribution on the right, the second τ decays via a $V+A$ interaction.

From these distributions it may be seen that the two pions tend to both have either low or high energy for SM couplings. For pure $V+A$ interactions on both

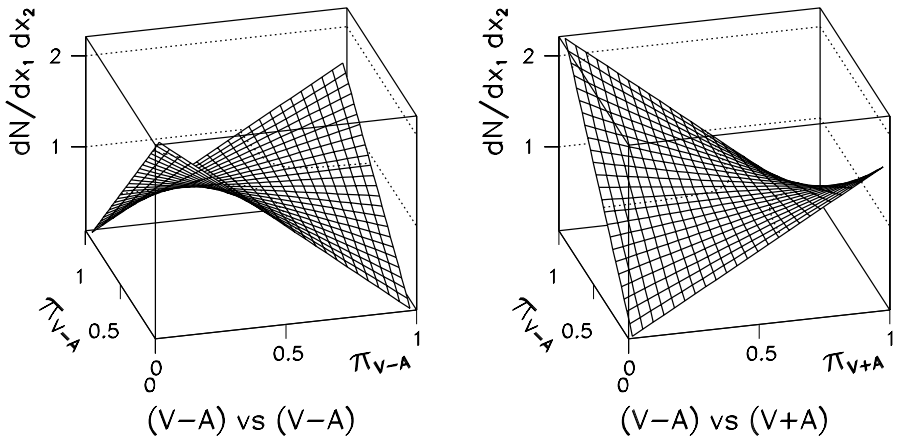

Figure 3.2: Correlated π–π spectra for $V-A$ on $V-A$ and $V-A$ on $V+A$. The figure on the left represents the SM π–π spectrum, while the figure on the right represents the spectrum for decays in which one of the τ's decayed via a $V+A$ current. For these figures, $\mathcal{P}_\tau = -0.15$ and $|\xi_\pi| = 1$.

sides, the result would be the same. A mixture of $V-A$ and $V+A$ causes events to migrate away from the corners in which both pions have about the same energy towards those in which their energies are maximally different.

3.2 Polarization and Chirality in $\tau^- \to \rho^- \nu_\tau$ and $\tau^+\tau^- \to \rho^+\rho^-\bar{\nu}_\tau\nu_\tau$

The kinematics of the decay $\tau^- \to \rho^-\nu_\tau$ is not as simple as that of the $\tau^- \to \pi^-\nu_\tau$ decay. The spin–1 ρ^- may be either transversely or longitudinally polarized. As shown in figure 3.3, this leads to eight possible decay configurations. The total

decay rate for each ρ polarization may be written as [46,61]

$$\frac{dN^T}{d\cos\theta} \propto \frac{m_\tau^2}{m_\rho^2}\left(1 - \mathcal{P}_\tau \xi_\rho \cos\theta\right), \tag{3.12}$$

for the transverse components and

$$\frac{dN^L}{d\cos\theta} \propto 2\left(1 + \mathcal{P}_\tau \xi_\rho \cos\theta\right), \tag{3.13}$$

for the longitudinal components.[3] Here θ is the angle between the τ flight direction in the lab frame and the ρ flight direction in the τ rest frame. The total decay rate for both polarizations is then

$$\frac{1}{N}\frac{dN}{d\cos\theta} = 1 - \alpha \mathcal{P}_\tau \xi_\rho \cos\theta, \tag{3.14}$$

where the factor α, given by

$$\alpha = \frac{m_\tau^2 - 2m_\rho^2}{m_\tau^2 + 2m_\rho^2} \approx 0.46, \tag{3.15}$$

suppresses the sensitivity to both τ polarization and chirality.

Ideally, if one could separate the ρ decays on the basis of ρ polarization, the sensitivity to τ polarization and chirality would be much better. One method of doing so is to reconstruct the decay angle ψ between the ρ^- flight direction and the π^- and π^0 in the ρ^- rest frame (see figure 3.4). For transversely polarized ρ's, the pions tend to have momenta directed along and opposite to the ρ spin, thus maximizing their energy difference in the lab frame. Conversely, for longitudinally polarized ρ's, the pions tend to be transverse to the ρ flight direction, minimizing their energy difference. Thus the new variable, $\cos\psi$, provides some sensitivity to which polarization state the ρ was in when it decayed and recovers much of the information lost by a mixture of the two states, increasing the sensitivity by approximately a factor of 2.

[3] Due to a difference in interpretation, reference [46] interchanges dN^T and dN^L.

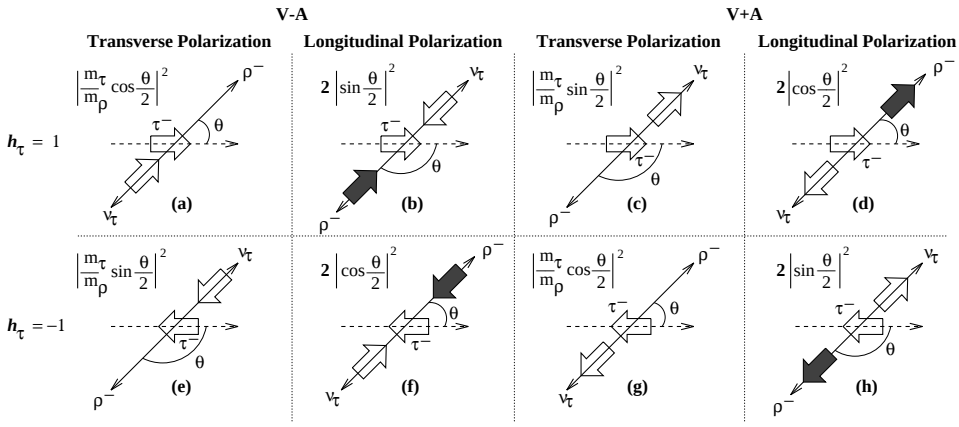

Figure 3.3: The relative decay amplitudes for $\tau^- \to \rho^- \nu_\tau$ for both helicity states of the ρ and τ are shown. The large open arrows indicate the spin of the leptons, while the large filled arrow indicates the spin of the spin–1 ρ. The four cases shown for each τ polarization are for the ρ polarization transverse to its line–of–flight and along its line–of–flight and for $V-A$ and $V+A$ couplings.

In terms of measurable energies and momenta in the lab frame, the decay angles of figures 3.3 and 3.4 are given by [41,46]

$$\cos\theta = \frac{4m_\tau^2}{m_\tau^2 - m_\rho^2}\frac{E_{\pi^-} + E_{\pi^0}}{E_{beam}} - \frac{m_\tau^2 + m_\rho^2}{m_\tau^2 - m_\rho^2} \tag{3.16}$$

and

$$\cos\psi = \frac{m_\rho}{\sqrt{m_\rho^2 - 4m_\pi^2}}\frac{E_{\pi^-} - E_{\pi^0}}{|\vec{P}_{\pi^-} + \vec{P}_{\pi^0}|}. \tag{3.17}$$

The decay amplitude in terms of both $\cos\theta$ and $\cos\psi$ may be written in the form [61]

$$\frac{1}{N}\frac{dN}{d\cos\theta d\cos\psi} = (1 - \mathcal{P}_\tau\xi_\rho)W^+(\cos\theta,\cos\psi) + (1 + \mathcal{P}_\tau\xi_\rho)W^-(\cos\theta,\cos\psi). \tag{3.18}$$

These distributions are illustrated in figure 3.5. For more details on the exact form of $W^\pm$, please see appendix B.

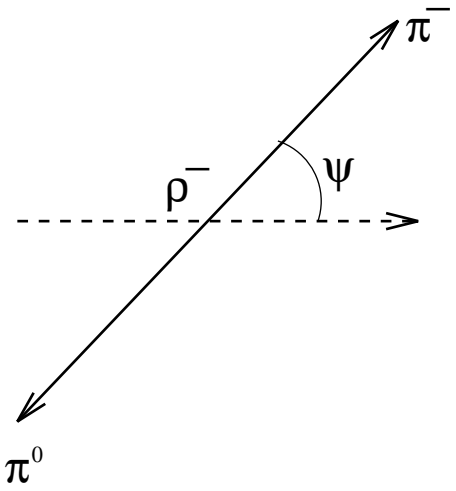

Figure 3.4: The definition of the decay angle ψ in the ρ rest frame. The dashed arrow points in the direction of flight of the ρ.

The above distribution, though complicated, lends itself well to the measurement of τ polarization and has been used for such [33, 35, 37]. For the correlated spectra to be exploited here, however, fitting with this two dimensional distribution on one side would require a three–dimensional fit in the case of π–ρ final states and a four–dimensional fit in the case of ρ–ρ final states. We avoid this complication by turning to the single variable ω_ρ, defined by [61]

$$\omega_\rho(\cos\theta, \cos\psi) = \frac{W^+(\cos\theta, \cos\psi) - W^-(\cos\theta, \cos\psi)}{W^+(\cos\theta, \cos\psi) + W^-(\cos\theta, \cos\psi)}, \tag{3.19}$$

for which the decay distribution may be written as

$$\frac{1}{N}\frac{dN}{d\omega_\rho} = \hat{W}(\omega_\rho)\left(1 - \mathcal{P}_\tau \xi_\rho \omega_\rho(\cos\theta, \cos\psi)\right), \tag{3.20}$$

where

$$\hat{W}(\omega_\rho) = \int \left(W^+ - W^-\right) \delta\left(\omega_\rho - \frac{W^+ - W^-}{W^+ + W^-}\right) d\cos\theta d\cos\psi. \tag{3.21}$$

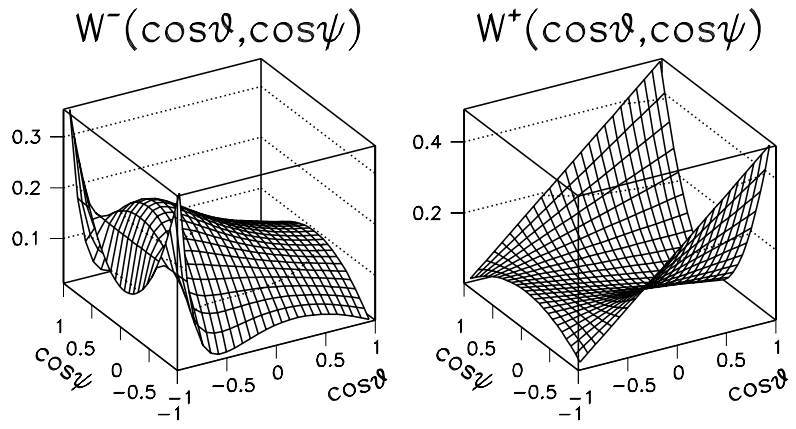

Figure 3.5: The decay distributions for W^- and W^+ in terms of the ρ kinematic variables $\cos\theta$ and $\cos\psi$.

Equation (3.20) is now in the familiar form

$$\frac{1}{N}\frac{dN}{d\omega_\rho} = F_\rho(x_\rho) - \mathcal{P}_\tau \xi_\rho G_\rho(x_\rho), \tag{3.22}$$

where x_ρ is simply the variable ω_ρ and F_ρ and G_ρ are given by

$$F_\rho(\omega_\rho) = \hat{W}(\omega_\rho) \tag{3.23}$$

and

$$G_\rho(\omega_\rho) = \omega_\rho \hat{W}(\omega_\rho). \tag{3.24}$$

In figure 3.6, ω_ρ as a function of the decay angles θ and ψ is shown, along with the functions F_ρ and G_ρ. In principle, this variable provides the same sensitivity as θ and ψ.

As with the pion, it is the double–sided distributions in the ρ which provide the sensitivity to chirality. For the ρ, the decay distribution is again in the general

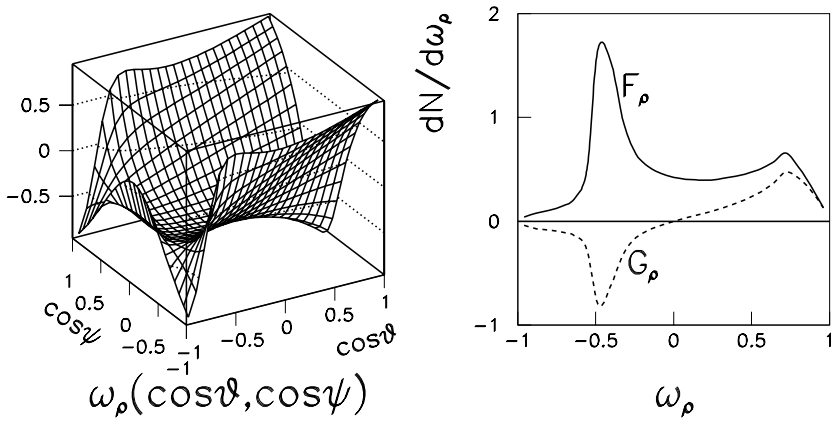

Figure 3.6: The single variable ω_ρ as a function of $\cos\theta$ and $\cos\psi$ and the decay distribution F_ρ and G_ρ for the ρ in terms of ω_ρ.

form

$$\frac{1}{N}\frac{dN}{d\omega_1 d\omega_2} \approx F_\rho(\omega_1)F_\rho(\omega_2) - \mathcal{P}_\tau\xi_\rho\left(F_\rho(x_1)G_\rho(\omega_2) + G_\rho(\omega_1)F_\rho(\omega_2)\right) \qquad (3.25)$$

$$+\xi_\rho^2 G_\rho(\omega_1)G_\rho(\omega_2).$$

Shown in figure 3.7 are two possible distributions for the ρ. In the distribution on the left, both τ's always decay via a $V-A$ current. In the distribution on the right, the second τ decays via a $V+A$ interaction.

3.3 Polarization and Chirality in $\tau^+\tau^- \to \rho^\pm\pi^\mp\bar{\nu}_\tau\nu_\tau$

The two–dimensional distribution of the decay rate for π–ρ final states must also be considered here. With the necessary functions in hand (F_π, G_π, F_ρ, and G_ρ), it

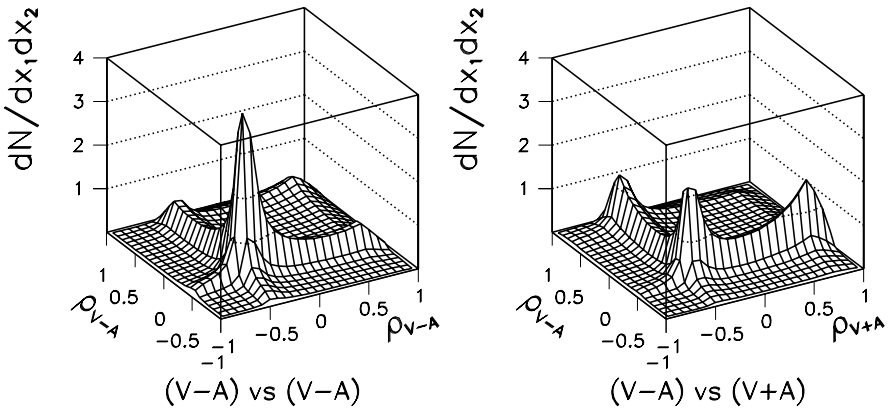

Figure 3.7: Correlated $\rho - \rho$ spectra for $V - A$ on $V - A$ and $V - A$ on $V + A$. For these figures, $\mathcal{P}_\tau = -0.15$ and $|\xi_\rho| = 1$.

is quickly constructed from the general form

$$\frac{1}{N}\frac{dN}{dx_\pi d\omega_\rho} \approx F_\pi(x_\pi)F_\pi(\omega_\rho) - \mathcal{P}_\tau\left(\xi_\rho F_\pi(x_\pi)G_\pi(\omega_\rho) + \xi_\pi G_\pi(x_\pi)F_\pi(\omega_\rho)\right) \qquad (3.26)$$

$$+\xi_\pi\xi_\rho G_\pi(x_\pi)G_\pi(\omega_\rho).$$

In figure 3.8, we show two different distributions. In the first, both the π and ρ were the result of a strictly $V - A$ decay of the τ. In the second, the ρ results from a purely $V + A$ current, i.e. $\xi_\rho = +1$.

3.4 Sensitivities

The sensitivities to $\mathcal{P}_\tau$ and ξ_h in the decay distributions of the previous sections may be quantified in the following manner. First we define the sensitivity in terms

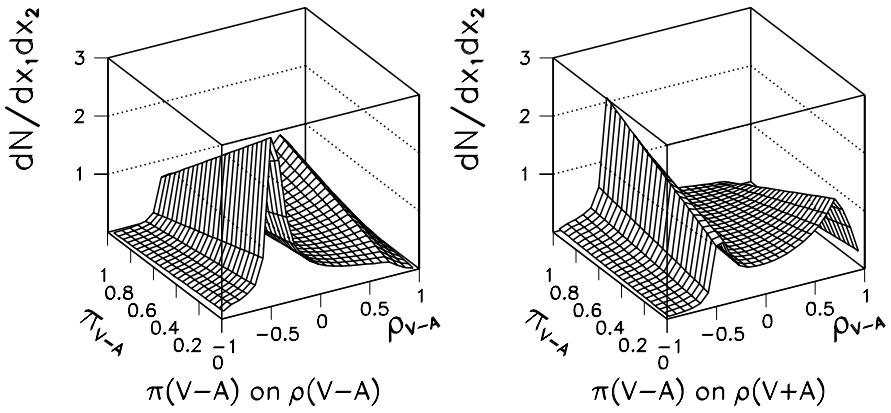

Figure 3.8: Correlated $\pi - \rho$ spectra for $V - A$ on $V - A$ and $V - A$ on $V + A$. For these figures, $\mathcal{P}_\tau = -0.15$, $\xi_\pi = -1$, and $\xi_\rho = -1(+1)$ for the picture on the left (right).

of the weight of a given measurement:

$$S^2 = \frac{1}{N\sigma^2}, \tag{3.27}$$

where N is the number of events sampled and S the sensitivity. Since $\sigma \propto 1/\sqrt{N}$, the sensitivity is independent of the number of events.

Now consider the unbinned likelihood $\mathcal{L}(\mathcal{M})$, defined by

$$\mathcal{L}(\mathcal{M}) = \prod_{i=1}^{N} \mathcal{W}(x_i), \tag{3.28}$$

where $\mathcal{M}$ is the quantity to be measured and $\mathcal{W}(x_i)$ the probability density for the ith event as a function of $\mathcal{M}$ and the variable space x. The desired value $\hat{\mathcal{M}}$ is that which maximizes the log of the likelihood. In particular, $\hat{\mathcal{M}}$ is the solution

to [62, 76]

$$0 = \frac{\partial \ln \mathcal{L}}{\partial \mathcal{M}} = \sum_{i=1}^{N} \frac{1}{\mathcal{W}(x_i)} \frac{\partial \mathcal{W}(x_i)}{\partial \mathcal{M}}. \tag{3.29}$$

The error on the measurement above may be estimated from

$$\frac{1}{\sigma^2} = -\left. \frac{\partial^2 \mathcal{L}}{\partial \mathcal{M}^2} \right|_{\hat{\mathcal{M}}} = \sum_{i=1}^{N} \left(\frac{1}{\mathcal{W}^2(x_i)} \left(\frac{\partial \mathcal{W}(x_i)}{\partial \mathcal{M}} \right)^2 - \frac{1}{\mathcal{W}(x_i)} \frac{\partial^2 \mathcal{W}(x_i)}{\partial \mathcal{M}^2} \right) \Bigg|_{\hat{\mathcal{M}}}. \tag{3.30}$$

As N becomes very large, the number of points in a small space $\triangle x_j$ around point x_j is approximately $N\mathcal{W}(x_j)\triangle x_j$. By evaluating W in the above sum at x_j, we may write

$$\frac{1}{\sigma^2} = N \sum_{j=1}^{N_x} \left(\frac{1}{\mathcal{W}(x_j)} \left(\frac{\partial \mathcal{W}(x_j)}{\partial \mathcal{M}} \right)^2 - \frac{\partial^2 \mathcal{W}(x_j)}{\partial \mathcal{M}^2} \right) \triangle x_j, \tag{3.31}$$

where the N_x subspaces $\triangle x_j$ span the space x and do not overlap. In the limit $N_x \to \infty$, the above sum becomes

$$S^2 = \frac{1}{N\sigma^2} = \int \left(\frac{1}{\mathcal{W}(x)} \left(\frac{\partial \mathcal{W}(x)}{\partial \mathcal{M}} \right)^2 - \frac{\partial^2 \mathcal{W}(x)}{\partial \mathcal{M}^2} \right) dx. \tag{3.32}$$

Examples of the sensitivity to $\mathcal{P}_\tau$ and ξ_h are given for both one and two–dimensional distributions in the sections below.

3.4.1 Single–Sided Distributions

For the single–sided decay distributions, we have the generic form

$$\mathcal{W}_h(x; \mathcal{P}_\tau, \xi_h) = F_h(x_h) - \mathcal{P}_\tau \xi_h G(x_h), \tag{3.33}$$

where $h = \pi, \rho$. For a fixed value of ξ_h, the sensitivity to $\mathcal{P}_\tau$ is given by

$$S^2_{\mathcal{P}_\tau} = \int \frac{\xi_h^2 G_h^2(x_h)}{F_h(x) - \mathcal{P}_\tau \xi_h G_h(x_h)} dx_h. \tag{3.34}$$

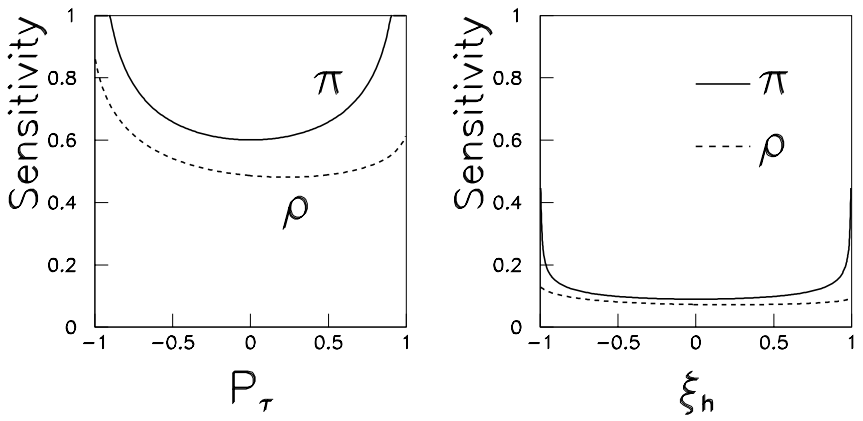

Figure 3.9: Sensitivity for the π and ρ single–sided distributions. The plot on the right is that for $\mathcal{P}_\tau$ with $\xi_h = -1$. The plot on the left is for ξ_h with $\mathcal{P}_\tau = -0.15$.

Similarly, the sensitivity to ξ_h for a fixed value of $\mathcal{P}_\tau$ is

$$S^2_{\xi_h} = \int \frac{\mathcal{P}^2_\tau G^2_h(x_h)}{F(x_h) - \mathcal{P}_\tau \xi_h G_h(x_h)} dx_h = \frac{\mathcal{P}^2_\tau}{\xi^2_h} S^2_{\mathcal{P}_\tau}. \tag{3.35}$$

For values of $\mathcal{P}_\tau$ and ξ_h near the standard model, the sensitivity to a measurement of $\mathcal{P}_\tau$ is approximately a factor of 7 larger than a measurement of ξ_h. This difference is illustrated in figure 3.9.

3.4.2 Double–Sided Distributions

In the double–sided distributions, the decay density assuming universality (*i.e.* $\xi_\pi = \xi_\rho \equiv \xi_h$) has the following form:

$$\mathcal{W}(x_1, x_2; \mathcal{P}_\tau, \xi_h) = F_1(x_1)F_2(x_2) - \mathcal{P}_\tau \xi_h \left(F_1(x_1)G_2(x_2) + F_2(x_2)G_1(x_1)\right) \tag{3.36}$$

$$+\xi^2_h G_1(x_1)G_2(x_2).$$

Here the subscripts 1 and 2 denote either a π or ρ and x_ρ is understood to mean ω_ρ. For a fixed value of ξ_h, the sensitivity to τ polarization is then given by

$$S^2_{\mathcal{P}_\tau} = \iint \frac{\xi_h^2 (F_1 G_2 + F_2 G_1)^2}{\mathcal{W}(x_1, x_2; \mathcal{P}_\tau, \xi_h)} dx_1 dx_2. \tag{3.37}$$

Due to the ξ_h^2 term in the decay density, the sensitivity to ξ_h does not have quite as simple a form as that above. In particular, we have

$$S^2_{\xi_h} = \iint \left(\frac{\left(2\xi_h G_1 G_2 - \mathcal{P}_\tau (F_1 G_2 + F_2 G_1)\right)^2}{\mathcal{W}(x_1, x_2; \mathcal{P}_\tau, \xi_h)} - 2 G_1 G_2 \right) dx_1 dx_2. \tag{3.38}$$

The last term in the integral integrates to 0 by virtue of equation (2.23). Thus we simplify the above expression to

$$S^2_{\xi_h} = \iint \frac{\left(2\xi_h G_1 G_2 - \mathcal{P}_\tau (F_1 G_2 + F_2 G_1)\right)^2}{\mathcal{W}(x_1, x_2; \mathcal{P}_\tau, \xi_h)} dx_1 dx_2. \tag{3.39}$$

The sensitivity as a function of $\mathcal{P}_\tau$ and as a function of ξ_h is shown in figure 3.10. Note that for values near the standard model, the sensitivity in the two–dimensional distributions to ξ_h is almost as large or larger, as in the case of $\pi - \pi$, than the sensitivity to $\mathcal{P}_\tau$.

Clearly it is the two–dimensional distributions which will determine the measured value of ξ_h. Thus one should pay particular attention to regions in the space (x_1, x_2) that are the most sensitive. These regions are clearly defined in the plots of figure 3.11. They are where one would intuitively expect them to be based on the changes seen in figures 3.2, 3.7, and 3.8 when one decay is changed from $V - A$ to $V + A$.

3.5 The Measurement of $\mathcal{P}_\tau$ and ξ_h

To measure of $\mathcal{P}_\tau$ and ξ_h, we first determine the distributions F_i and G_i in bins of x_i for each decay mode using a full detector simulation. The data is binned in the

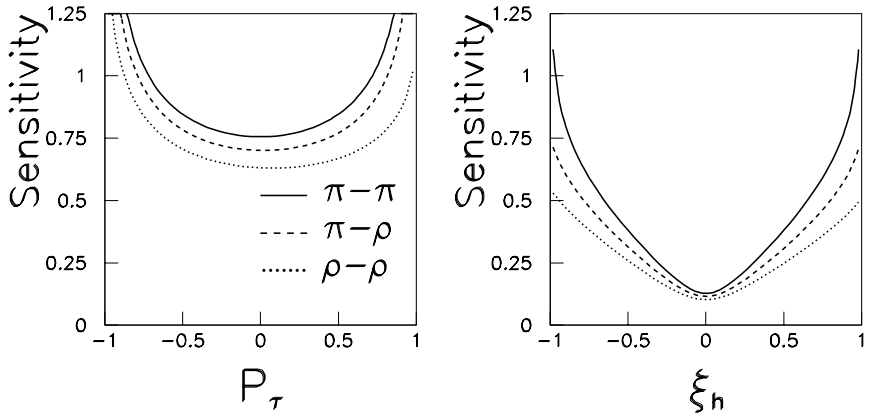

Figure 3.10: Sensitivity for the $\pi-\pi$, $\pi-\rho$ and $\rho-\rho$ double–sided distributions. The plot on the right is that for $\mathcal{P}_\tau$ with $\xi_h = -1$. The plot on the left is for ξ_h with $\mathcal{P}_\tau = -0.15$.

same manner, and we form the total likelihood

$$\mathcal{L}(\mathcal{P}_\tau, \xi_h) = \mathcal{L}_{\pi X} \cdot \mathcal{L}_{\rho X} \cdot \mathcal{L}_{\pi\pi} \cdot \mathcal{L}_{\pi\rho} \cdot \mathcal{L}_{\rho\rho}, \tag{3.40}$$

which is simply the product of the likelihoods for each channel.

The likelihood for a given channel is given by

$$\mathcal{L} = \prod_j P(m_j; \mu_j), \tag{3.41}$$

where j runs over all of the bins in the channel. We have denoted the probability of observing m_j events in data given the expected number of events μ_j from Monte Carlo as $P(m_j; \mu_j)$. Assuming Poisson statistics may be applied,

$$P(m_j; \mu_j) = \frac{\mu_j^{m_j}}{m_j!} e^{-\mu_j}. \tag{3.42}$$

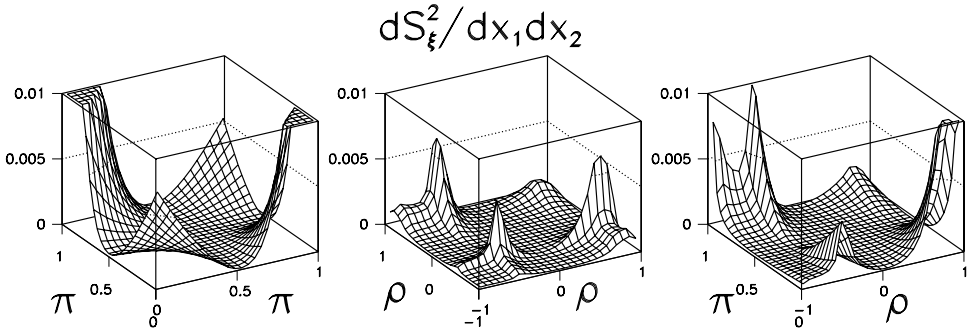

Figure 3.11: Sensitivity for the $\pi - \pi$, $\pi - \rho$ and $\rho - \rho$ double–sided distributions to chirality versus x_1 and x_2. These plots were constructed for $\mathcal{P}_\tau = -0.15$ and $\xi_h = -1$.

The expected number of events is given by the distributions of equations (3.10), (3.11), (3.22), (3.25), and (3.26) normalized to the number of events observed in the data.

To obtain the values of $\mathcal{P}_\tau$ and ξ_h which fit the data best, we wish to maximize the likelihood $\mathcal{L}(\mathcal{P}_\tau, \xi_h)$. In practice, for numerical simplicity, we perform the equivalent operation of minimizing the negative of the log of the likelihood. This minimization is performed using the numerical minimization package MINUIT [63].

3.6 Systematic Errors

We present here an outline of the most important systematic errors which influence this measurement. Some of them, given a perfect simulation of the underlying physics and detector response, would simply disappear. Others are related to fluctuations in the data which disappear slowly with increased statistics. In chapter 6,

we present our estimate of each of the following systematic errors.

3.6.1 Selection

Systematic errors due to the selection procedure, described later in chapter 5, arise primarily through differences between the real detector and the simulated detector. In general, selection efficiency falls off at both high and low energies due to cuts tuned primarily to reject non–τ background. Since these in general fall into sensitive regions, differences in Monte Carlo efficiencies and efficiencies in data could introduce a shift in the measured value. For example, a preference in the data for the selection of high energy pions would bias the measurement of polarization towards more positive values.

3.6.2 Background

There are two types of backgrounds in the actual measured spectra for each of the channels above. The first is non–τ background, arising primarily from misidentified Bhabha events ($e^+e^- \rightarrow Z(\gamma) \rightarrow e^+e^-$), dimuons events ($e^+e^- \rightarrow Z \rightarrow \mu^+\mu^-$), two–photon events ($e^+e^- \rightarrow e^+e^-f^+f^-$), and the occasional misidentified cosmic ray. The second type of background is due to misidentified τ events. Systematic errors due to both of these backgrounds result from incorrect estimations in the level and make–up of each background.

Non–τ Background

Background from Bhabhas, dimuons, two–photon events, and cosmic rays are each identified based on their global event characteristics in real data. Monte Carlo for

these backgrounds has been used only to cross–check the procedure. These backgrounds can fake the τ events of interest here in many ways, though their effect is seen primarily in the one–dimensional decay spectra. The probability that these backgrounds fake a τ event on both sides falls off roughly as the fraction of contamination in the one–dimensional distributions squared. Since the contamination in the one–dimensional distributions is roughly 1%, the expected background in the two–dimensional distributions is roughly 0.01%.

An electron in a Bhabha event may fake a pion by either showering late in the electromagnetic calorimeter and having energy leak over into the hadronic calorimeter or by simply missing the electromagnetic calorimeter all together. Since the BGO crystals make up only 98% of the surface of the BGO barrel, with the other 2% consisting of support structure and gaps, the second possibility above is not as low as one might initially estimate. The probability of faking a rho is much lower due to the more complex rho kinematics. Because Bhabhas tend to fake high energy pions, they are a potentially dangerous source of polarization bias. This background is identified primarily through looking for an energetic electron on the other side.

A muon may fake a pion by showering in the hadron calorimeter. It may also fake a rho by first radiating a photon and then showering in the calorimeter. This background tends to fall into the least sensitive region for pions and be relatively flat across the ω_ρ spectrum. As with electrons, this background is identified by looking for an energetic muon on the other side.

Two–photon events are a problem primarily in the pion channel. There they fake low energy $\tau^- \to \pi^-\nu_\tau$ events, introducing a bias towards more negative (positive) values if under (over) estimated. Because their distribution in the acolinearity

between tracks in opposite hemispheres is relatively flat and because real τ events are grouped at small values of acolinearity, this background may be removed primarily through a cut on acolinearity. The contamination in the τ spectrum is estimated from a sample of rejected events.

Low energy cosmic ray events may mimic a pion by passing through one–half of the detector as showering in the hadron calorimeter and stopping on the other side. High energy cosmic rays often leave behind showers as well; however, they tend to exit the detector, leaving a clearly identifiable track in the muon chambers on both sides of the event. Requiring that the track simply pass within 2 mm of the primary event vertex reduces this background to an easily manageable level. Unfortunately, like two–photon events, this background tends to fall at the very low energy end of the pion spectra.

τ Background

Background from other τ decays is estimated directly from the $\tau^+\tau^-$ Monte Carlo. Even given a perfect simulation of the detector response, infinite Monte Carlo statistics, and an exact description of the physics occurring in nature, statistical fluctuations in data would keep systematics from this background from disappearing. In addition to fluctuations in the fraction of each final state present in the data, statistical shifts in the average polarization and chirality in these backgrounds must also be considered, since this background does carry information on polarization and chirality.

3.6.3 Calibration

Systematic errors arise from uncertainties in the calibration of each subdetector. For this measurement, the most important are the absolute momentum scale of the central tracking, the response of the electromagnetic calorimeter to an electromagnetic shower, the response of the electromagnetic calorimeter to a hadronic shower, and the response of the hadronic calorimeter to a hadronic shower. All of these relate to the overall energy scale of the detector. Based on estimates from real data and well known physical processes, we evaluate this systematic by varying the energy response in each of the above cases within the limits of the uncertainty of the calibration.

3.6.4 Radiative Corrections

We correct for initial state radiation from calculations made using the ZFITTER program [48, 49]. In addition, ZFITTER provides corrections due to γ–exchange and γZ–interference in the propagator. These are applied as a systematic shift in the overall τ polarization.

Chapter 4

The L3 Detector at LEP

4.1 The Large Electron Positron Storage Ring

Encompassing an area roughly one-fourth the size of Washington, D.C., the Large Electron Positron storage ring (LEP) straddles the French-Swiss border just west of Geneva, Switzerland at a depth varying between 50 and 150 meters below the surface. Shown in figure 4.1, the LEP ring was the major addition to the CERN accelerator complex in the 1980's.

The circumference of 26.7 km was chosen to provide an initial center-of-mass energy of $\sqrt{s} \approx 90$ GeV, with magnet upgrades eventually extending the energy range up to 200 GeV in 1996. The physical motivations for these design energies were the top quark, then estimated to be as low as 20 GeV, and the massive gauge bosons, Z and $W^{\pm}$, estimated to be below 100 GeV. The existence of a heavy top at 176 GeV [23,24] has only placed more emphasis on the Z and $W^{\pm}$.

In reality, the LEP ring is not a circle. It consists of eight bending sections connected by eight straight sections. The bending sections, each 2840 m in length,

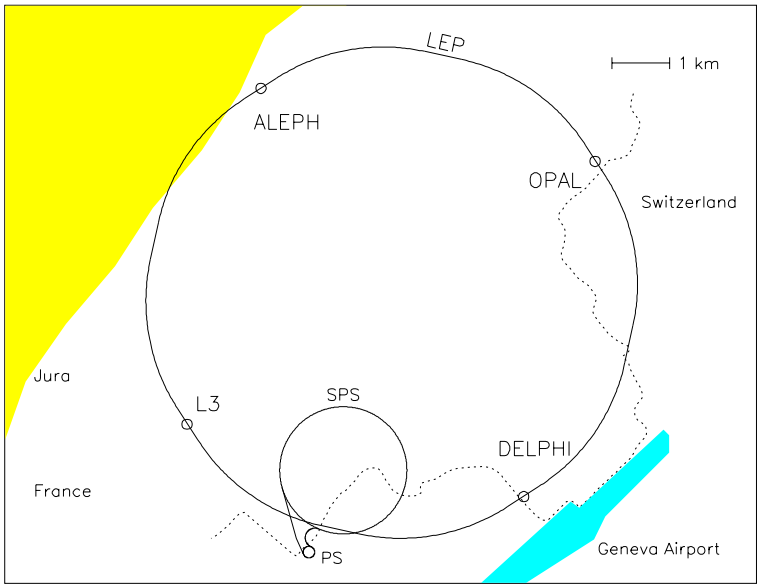

Figure 4.1: The LEP Storage Ring

house the dipole magnets for steering the beam around the ring. The straight sections are each 490 m in length. Four of these eight sections contain the LEP experiments, ALEPH, DELPHI, L3, and OPAL. The sections containing L3 and Opal also have accelerating radio frequency cavities that ramp the beams up to the nominal energy. In addition they compensate for the energy lost to synchrotron radiation during each circuit of the beam.

The larger components of the injection system for the LEP ring are also shown in figure 4.1. They are the Super Proton Synchrotron (SPS) and the Proton Synchrotron (PS). Unlike US labs, which have started from scratch with each accelerator complex, the CERN complex has continuously used older machines to support new ones. The only major new components of the injection system built

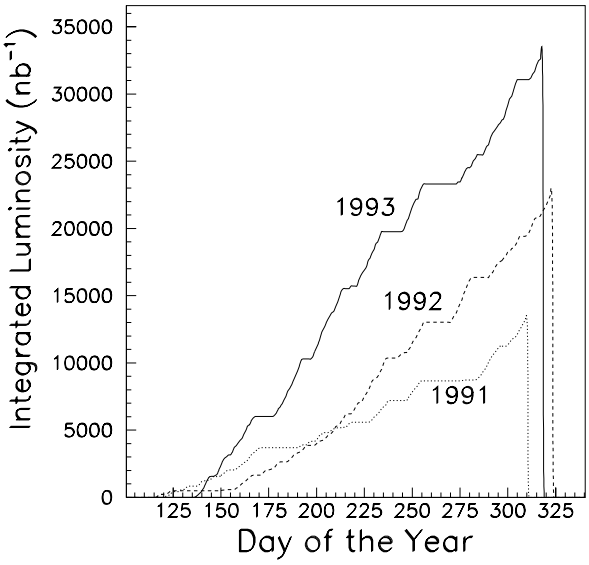

Figure 4.2: L3 Integrated Luminosity for 1991-93

for LEP were the short LEP Injector Linac (LIL) and the small Electron Positron Accumulator (EPA) ring. A detailed description of the whole LEP apparatus may be found in the LEP design reports [64].

Through 1992, the LEP ring operated in 4×4 bunch mode. In this mode, four bunches of circulating electrons collide with four bunches of counter circulating positrons at each of the LEP experiments. In 1993, 8×8 bunch mode operation began, with each bunch in a pretzel orbit that allowed the electron and positron bunches to pass each other at the midpoints between experiments. The integrated luminosity accumulated by L3 versus the day of the year is show for 1991 through 1993 in figure 4.2.

4.2 The L3 Detector

The L3 detector has been designed to optimize the energy resolution on electrons, photons, muons, and jets produced in e^+e^- collisions at energies up to 200 GeV. Its general design is similar to other multi-purpose e^+e^- detectors, as may be seen in figures 4.3 through 4.5. An emphasis has been placed, however, on electrons, photons, muons, and jets. The motivation for this emphasis was in part the Linde–Weinberg lower limit on the Higgs mass for a top mass below 80 GeV (see figure 4.6) [65]. Thus in looking at the L3 detector in detail, one finds the size and shape of the central tracking being dictated by the electromagnetic calorimetry, rather than the reverse.

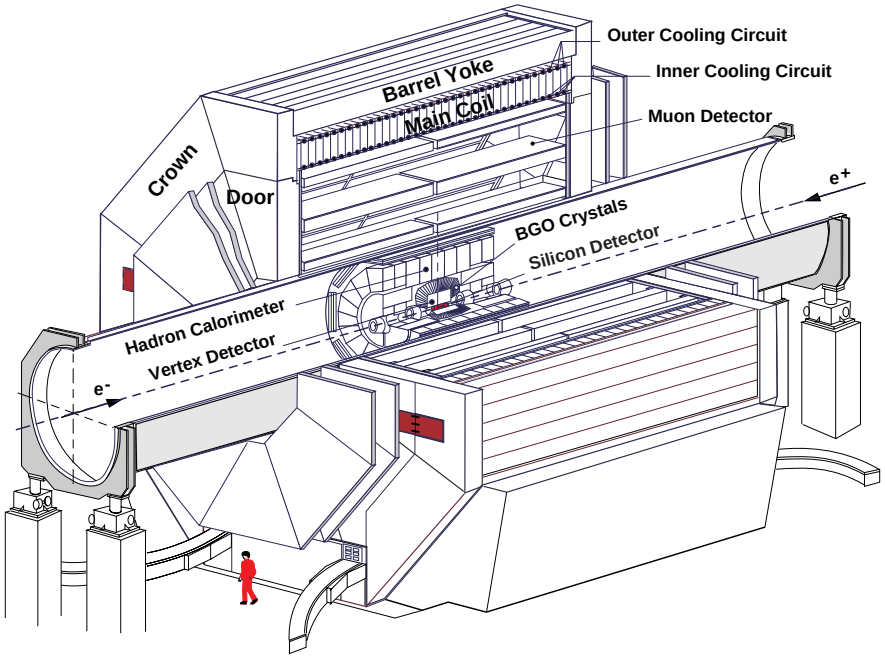

Figure 4.3: The L3 Detector.

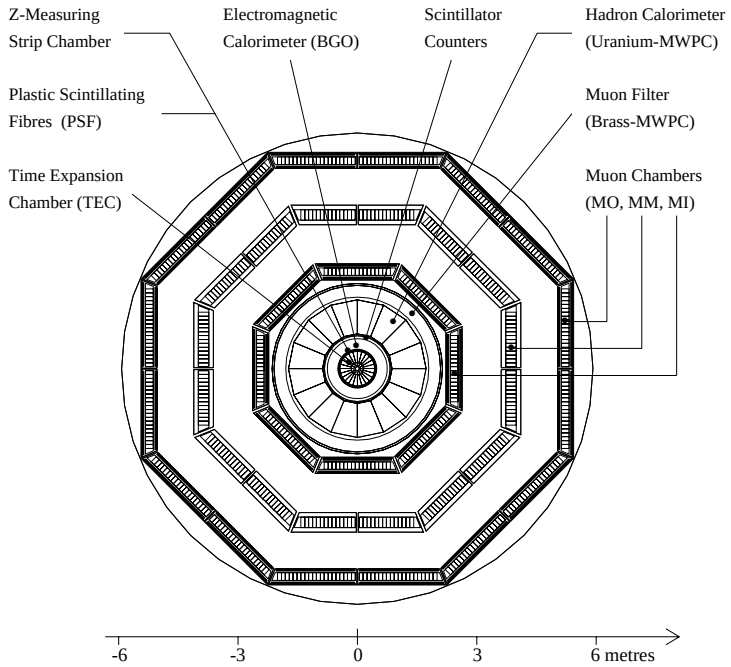

Figure 4.4: The L3 Detector in r - ϕ.

A detailed description of the L3 detector is provided in [66]. Here we briefly describe those features relevant to the charge current measurement. In figure 4.3, one can see the general layout, with the central tracking, electromagnetic calorimetry, and hadronic calorimetry installed inside a 32 m long support tube. The muon spectrometer is mounted on the outside of the tube. The support tube adjusts automatically to keep subdetectors aligned parallel to the beam. All subdetectors are contained inside the 0.5 Tesla magnet, which rests on the floor of the experimental hall.

The coordinate system of the L3 detector is defined by the direction of the e^- beam and the perpendicular to the earth, with the z-axis taken to be the e^- beam direction and the y-axis taken to be 'up'. The x-axis is then just the third axis of

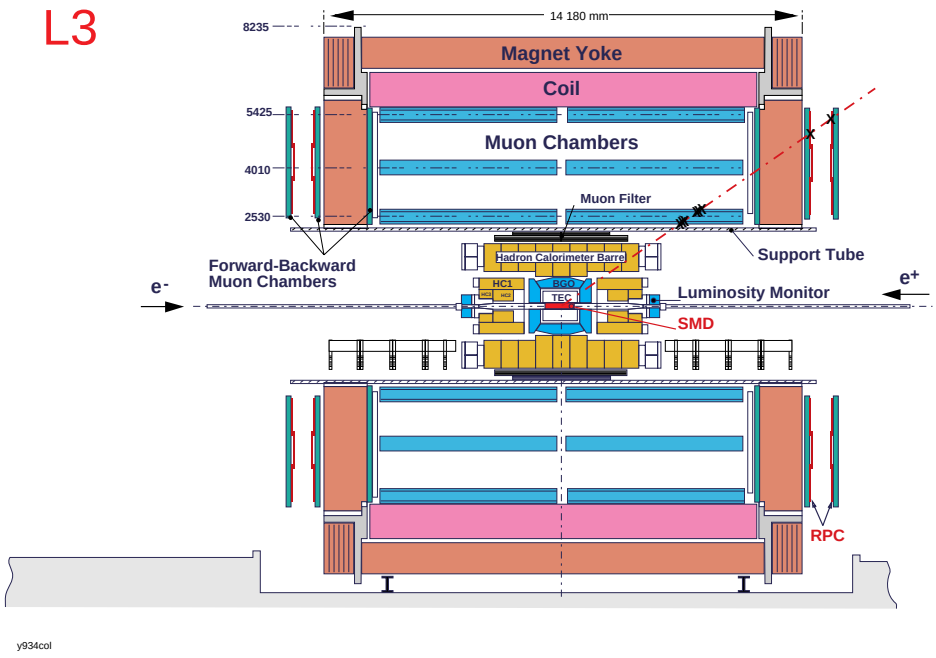

Figure 4.5: The L3 Detector in r - z.

the right-handed coordinate system. More appropriately, the L3 coordinate system usually is presented in the standard polar form (r,θ,ϕ), where θ is the polar angle with respect to the z-axis, and ϕ is the azimuthal angle. A plan perpendicular to the beam axis is denoted as a 'transverse' plane.

4.2.1 Magnet

The magnet is an octagonal aluminum coil, inside an iron return yoke. The inner diameter and length of the magnet are 12 m. Within this volume, the 30,000 Amp conventional magnet provides a uniform 0.5 Tesla field parallel to the beam. This magnetic field is mapped inside the support tube with hall probes and outside the

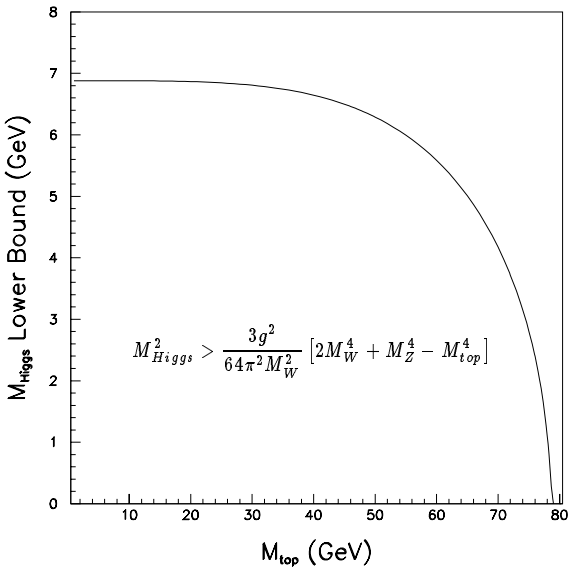

Figure 4.6: The Linde–Weinberg Lower Limit on the Higgs Mass.

support tube with magneto-resistors mounted on the muon spectrometer.

4.2.2 Central Tracking

The central tracking consists of a Silicon Micro vertex Detector (SMD), a Time Expansion Chamber (TEC), a Z-chamber, and Forward Tracking Chambers (FTC). Since the SMD did not become fully operational until 1994, it is not included in the discussion here. The TEC and Z-chamber are shown in figure 4.7, along with the Plastic Scintillating Fiber system (PSF) introduced in 1991 for calibration purposes. For more information than the brief description included here, see [67].

The TEC consists of 12 inner sectors and 24 outer sectors contained within a

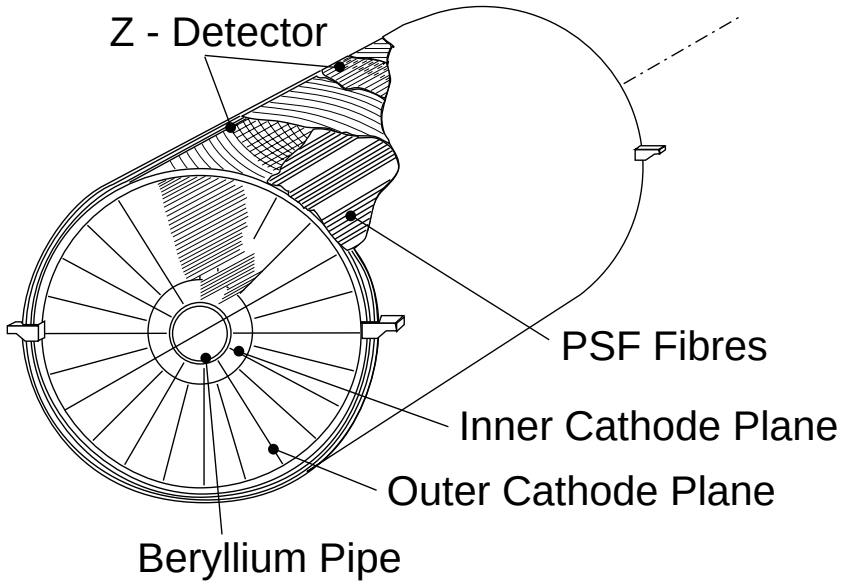

Figure 4.7: The Time Expansion Chamber (TEC)

single gas volume. Each sector is defined by a set of cathode wires running parallel to the z-axis, as shown in figures 4.7 and 4.8. In the middle of each sector, again running parallel to the z-axis, is an amplification region, shown in figure 4.9, which is defined by two grounded grids and a set of alternating anode and focus wires. There are 8 anodes in each inner sector and 54 anodes in each outer sector.

The anode wires are divided into groups which serve three different purposes: (a) standard anodes read out at one end only for an r–ϕ measurement, (b) charge division anodes are read out at both ends for an r–ϕ and a z measurement (2 in each inner sector and 9 in each outer sector), and (c) left-right ambiguity anodes have the grid on either side of them instrumented to determine from which half-sector the track drifted (14 in each outer sector).

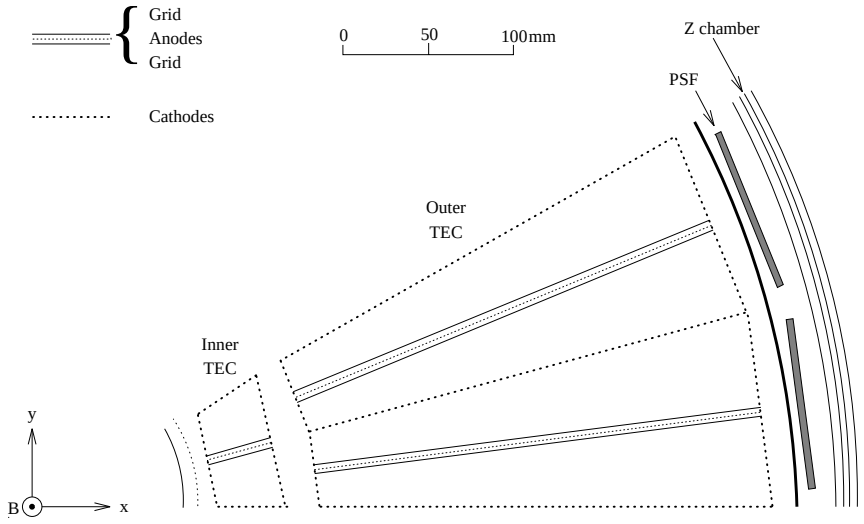

Figure 4.8: One Inner and Two Outer TEC Sectors

The gas mixture (80% carbon dioxide and 20% iso-butane at 1.2 bar) and cathode voltage were chosen to obtain a low drift velocity of $6\mu m/ns$. This maximizes the single wire resolution, within the timing constraint of $11\mu s$ between events with LEP in 8×8 mode. The average single wire resolution is $60\mu m$ on the inner wires and $50\mu m$ on the outer wires. Such accuracy becomes absolutely necessary in light of the small 31.7 cm lever arm of the TEC and the low magnetic field, resulting in a $B\ell^2$ of only 0.05 T·m. The measured transverse momentum resolution, using muons and the momentum measured in the muon spectrometer as a reference, has been determined to be $\sigma_{p_t}/p_t^2 = 0.018(GeV/c)^{-1}$.

With the charge division anodes providing a z resolution of only a few centimeters, the primary source of z information comes from the precise measurement made in the Z-chamber. This chamber consists of four layers with cathode-strip readout. Two layers run perpendicular to the beam direction, providing only a z

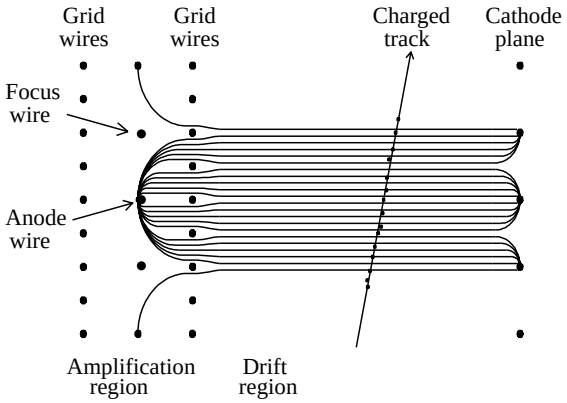

Figure 4.9: The TEC Amplification and Drift Regions

measurement with no ϕ information. The other two layers are formed from helices tilted at $\pm 69°$ with respect to the z axis. These layers provide both a z and ϕ measurement and resolve the ambiguity in the other layers. The measured Z-chamber resolution for $|cos(\theta)| < 0.5$ is $400\mu m$, degrading to $1200\mu m$ near the end of the chamber at $|cos(\theta)| = 0.74$.

The FTC aids in measuring the charge of tracks in the forward and backwards regions of the TEC. It consists of drift chambers placed between the TEC end-flange and the BGO endcap. These chambers measure x and y for charged tracks with a resolution of $200\mu m$. The FTC resolution suffers in part from scattering in the 4 cm thick aluminum end-flange of the TEC.

4.2.3 Electromagnetic Calorimeter

The electromagnetic colorimeter provides and excellent energy and spatial resolution. The 10734 BGO crystals from which the calorimeter is constructed cover the polar angles $11.6° < \theta < 38°$ (1527 crystals), $42° < \theta < 138°$ (7680 crystals), and $142° < \theta < 168.4°$ (1527 crystals) [68]. The length of each crystal is about 24 cm, which corresponds to approximately 22 radiation lengths and one interaction length.

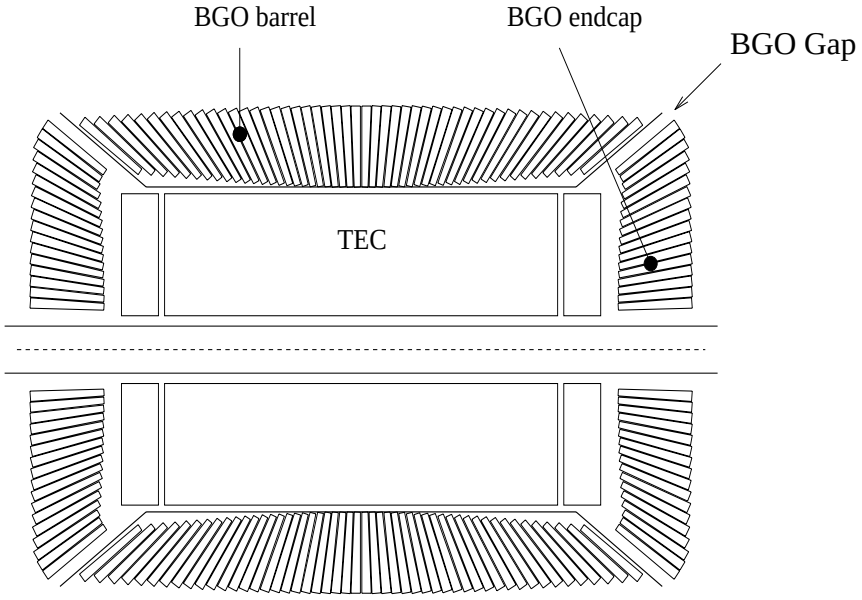

Figure 4.10: An r - z View of the Electro-magnetic Calorimeter (BGO)

As shown in figure 4.10, each crystal is aligned in a projective geometry so that it points towards the nominal event vertex. The truncated pyramidal geometry of an individual crystal is shown in figure 4.11. Two 1.5 cm^2 photo diodes are used

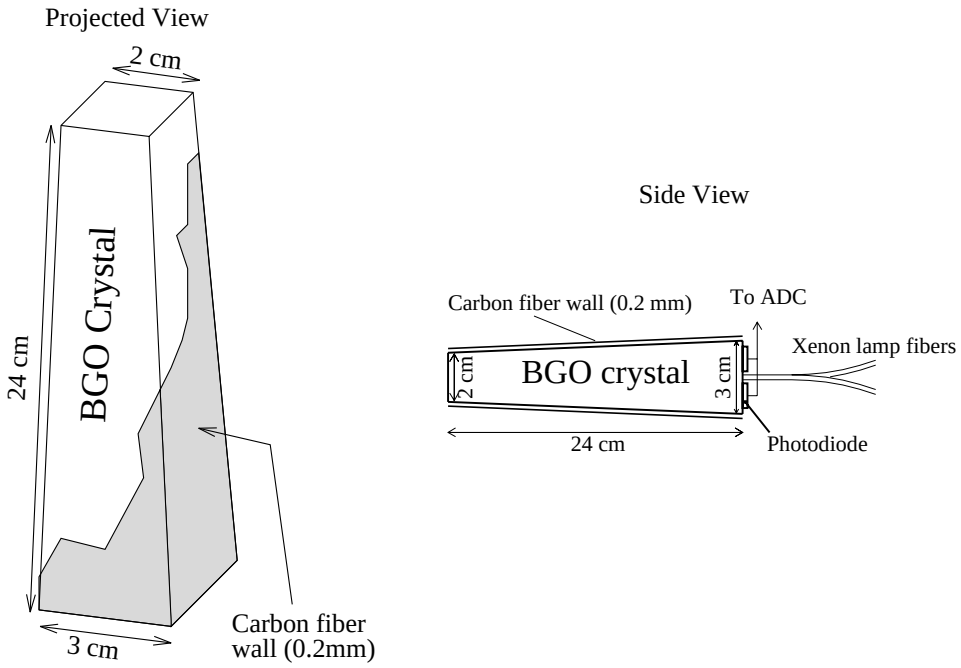

Figure 4.11: A BGO Crystal

to read out each crystal with a quantum efficiency of roughly 70%. The energy resolution for 100 MeV electrons and photons is about 5%. Above 1 GeV, the resolution improves to about 1.4%. Due to the relatively small Molière radius (2.3 cm), the spatial resolution above 2 GeV is better than 1 mm.

Between LEP fills, the transparency of the BGO crystals is measured using xenon light carried to each crystal via optical fibers. This and Bhabha scattering information are used to maintain an absolute energy calibration to within 0.9%. The quality of the energy measurement may be seen from the reconstructed π° and η mass plots shown in figure 4.12.

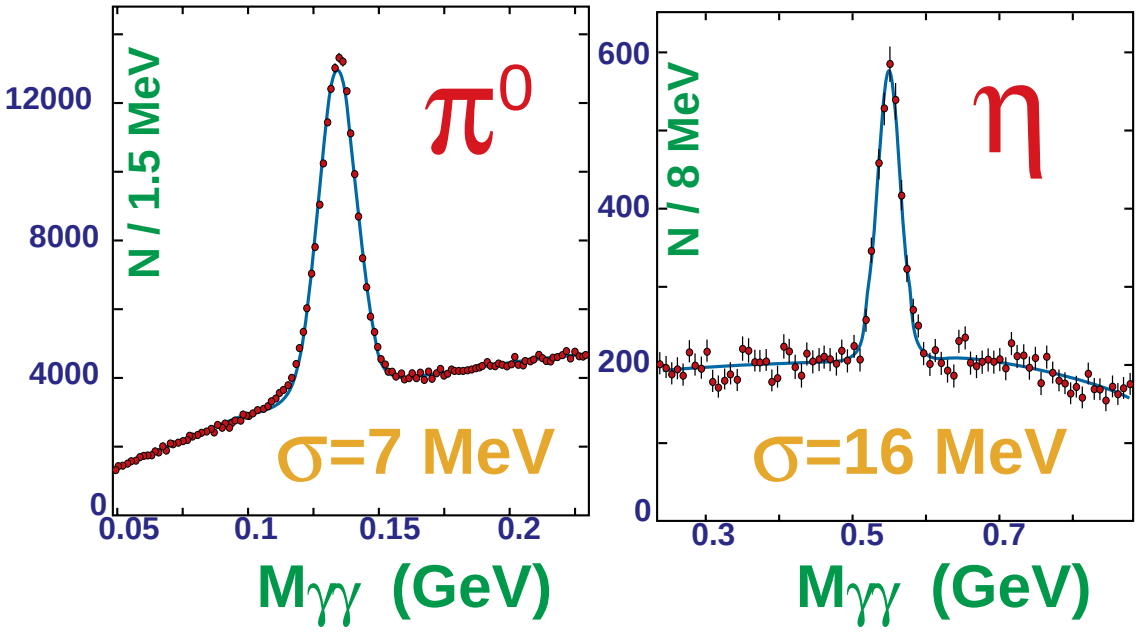

Figure 4.12: Measured $\gamma\gamma$ Mass Spectra from L3 at LEP.

4.2.4 Scintillation Counters

The L3 scintillation counters are clearly shown in figure 4.13, along with the elements of the calorimetry and the TEC. The scintillators lie between the electromagnetic and the hadronic calorimetry and consist of 30 single plastic counters. They cover $|cos(\theta)| < 0.83$ and have and azimuthal coverage of 93%.

The scintillators provide a trigger for hadronic events based simply on the hit multiplicity and serve to reject cosmic muons on-line based on both timing with the interaction and time-of-flight across the detector. For cosmic muons which pass near the interaction region, the time-of-flight results in approximately a 6 ns difference in time of the scintillator hits. For muons coming from e^+e^- collisions,

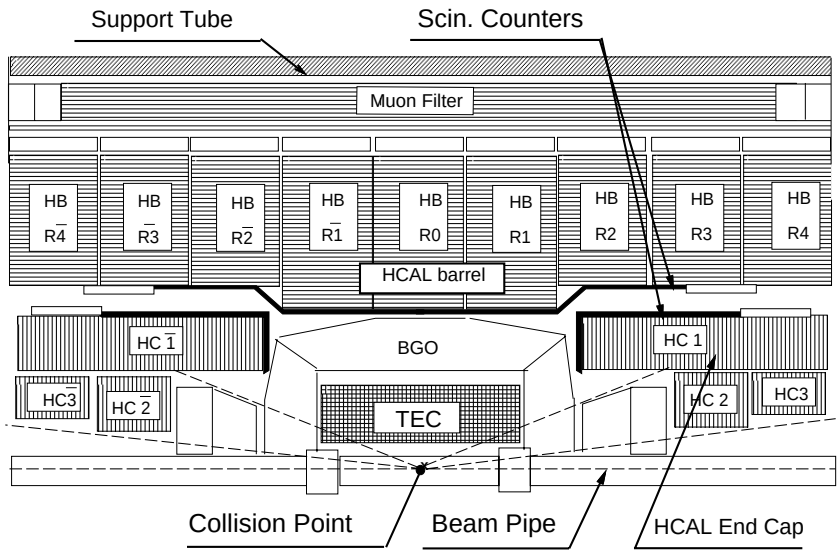

Figure 4.13: The HCAL, Muon Filter, and Scintillator Counters

there should be no difference. The scintillator timing resolution, determined from $e^+e^- \to \mu^+\mu^-$ to be better than 0.5 ns, is shown in figure 4.14. [69]

4.2.5 Hadron Calorimeter and Muon Filter

The hadron calorimeter (HCAL) depends on the total absorption of showering particles in uranium plates and the measurement of the deposited energy with proportional chambers. The HCAL also aids in the identification of muons, which leave minimal ionization matching to projected TEC and muon chamber tracks. In addition to the HCAL, there is a muon filter constructed of brass plates (65% Cu + 35% Zn) and proportional chambers which sits between the HCAL and muon

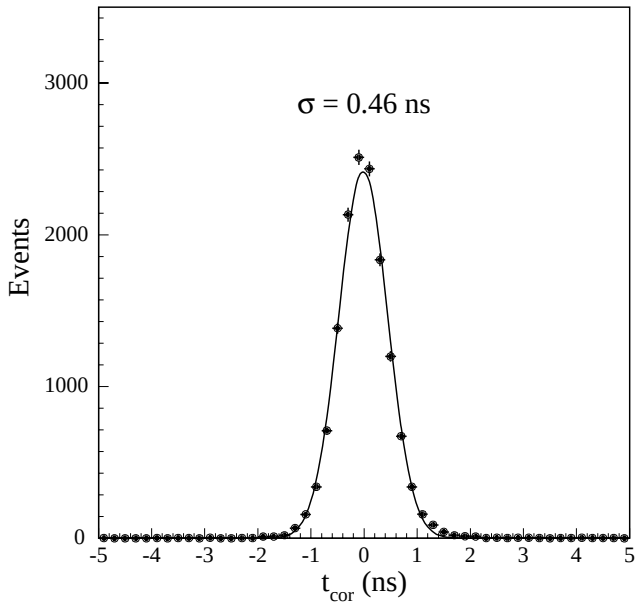

Figure 4.14: Scintillator timing from $e^+e^- \to \mu^+\mu^-$.

spectrometer. [69]

As shown in figures 4.13 and 4.15, the HCAL barrel is divided into 16 sections in ϕ, 6 short sections, and 3 long sections in z. This barrel region covers the angular region $35° < \theta < 145°$ with 7968 proportional wire chambers containing a total of 370 000 wires.

In each section of the HCAL barrel, the chambers are grouped into 5(4) for measuring ϕ and 5(4) for measuring z in each of the long(short) sections. The wires in each module are grouped into 9 readout towers for each orientation, with constant coverage in either ϕ or θ typically on the order of $\triangle\phi = 2°$ and $\triangle\theta = 2°$. The thickness of the barrel region is at least 6 nuclear absorption lengths.

The endcaps of the HCAL, also shown in figures 4.13 and 4.15, cover the angular

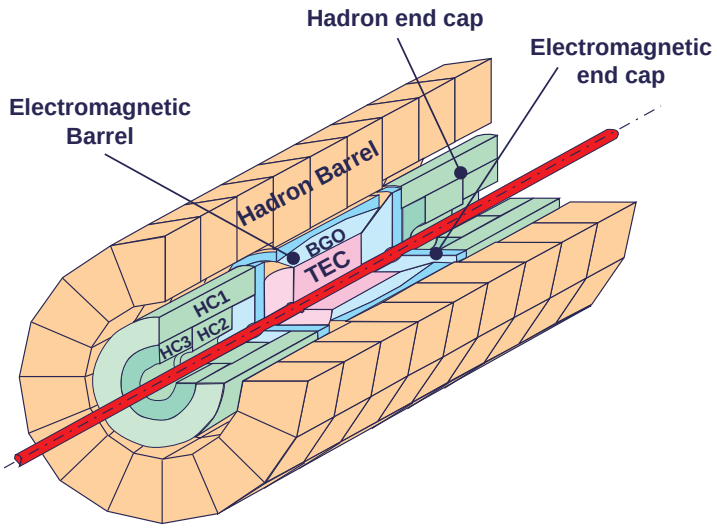

Figure 4.15: A L3 Hadron Calorimeter (HCAL)

regions $5.5° < \theta < 35°$ and $145° < \theta < 174.5°$. Each consists of three rings which are split into half-rings, resulting in twelve separate modules. This design aids in easy removal of the endcaps to obtain access to the inner portions of the L3 detector.

The endcaps are constructed of stainless steel containers filled with alternating layers of brass proportional chambers and 5.5 mm thick depleted uranium plates. The wires are grouped into 3960 towers covering regions of $\triangle\phi = 2°$ and $\triangle\theta = 2°$. In total, the HCAL endcaps represent between 6 and 7 absorption lengths.

The muon filter, located outside the HCAL barrel, as shown in figure 4.13, is divided into eight sections in ϕ, corresponding to the octal geometry of the muon chamber system described later in section 4.2.6. Each section consists of 6 brass

absorber plates, each 1 cm thick, interleaved with 5 proportional wire chambers. Beyond these are a set of absorber plates 1.5 cm thick which match the circular curvature of the support tube. In total, the muon filter represents another 1.03 absorption lengths.

The fine segmentation of the hadronic calorimetry allows the determination of a jet axis with an angular resolution of approximately 2.5°. In addition, the energy resolution for jets is on the order of 10% while that for single π's is better than 20%.

4.2.6 Muon Spectrometer

The muon spectrometer, as may be seen in figure 4.5, consists of two halves with a gap at $z = 0$. Each of these halves is divided into eight independent units dubbed octants. As may be seen in figures 4.16 and 4.17, these octants are divided into three layers of wire chambers: an inner chamber, and two middle chambers, and two outer chambers. The inner and outer chambers each provide up to 16 points on a track, while the middle chamber provides 24. In addition to "P" chambers, the inner and out chambers have on their inner and outer sides a set of "Z" chambers. Together, the P and Z chambers yield a measurement of the momentum vector of the track.

Due to the size of the muon spectrometer, the small magnetic field is compensated for by the large lever arm of 2.9 m, yielding a $B\ell^2$ of 4.21 $T \cdot m^2$. This yields a momentum resolution of $\sigma_p/p \approx 2.5\%$ at $p = 45 GeV/c$. One major systematic, alignment between octants, becomes irrelevant for muons above $3 GeV$, which stay within one octant. Within an octant, the alignment system sets the position of each chamber to better than 30 μm.

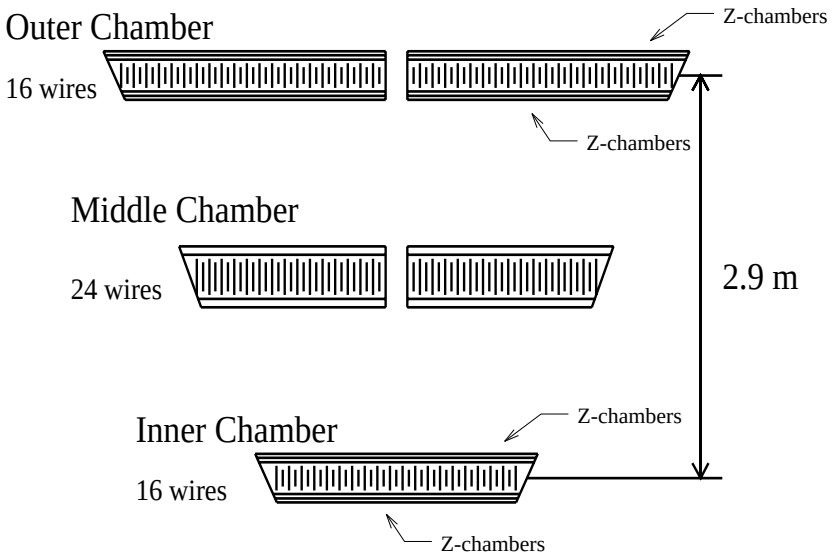

Figure 4.16: A Muon Spectrometer Octant (MUCH).

The muon spectrometer covers the range $|cos(\theta)| < 0.71$ with all three layers. The inner two layers extend this range to $|cos(\theta)| < 0.8$; however, beyond 0.71 the momentum resolution necessarily degrades due to the lack of hits in the outer layer.

4.2.7 Luminosity Monitor

The luminosity monitor, half of which is shown in figure 4.18, consists of two BGO electromagnetic calorimeters and two sets of proportional wire chambers, located in symmetric positions on either end of the detector. It covers the angular region 35 mrad $< \theta <$ 70 mrad. This region is dominated by $e^+e^- \rightarrow e^+e^-$ via t-channel photon exchange. Comparison of the measured rate of events in the luminosity monitor to the theoretical calculation provides a measurement of the luminosity

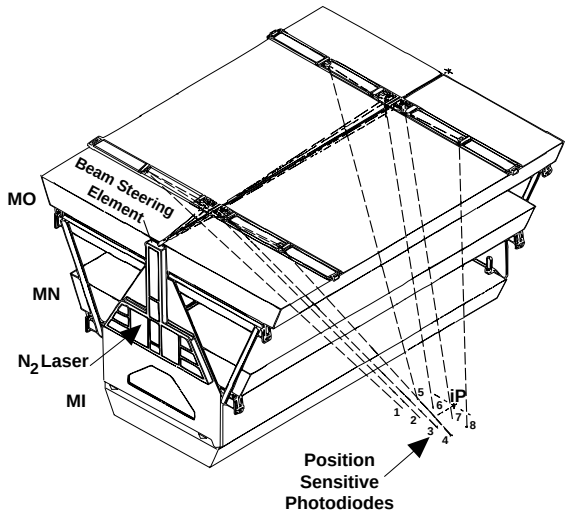

Figure 4.17: Half of a MUCH Octant in Perspective.

delivered to the L3 detector.

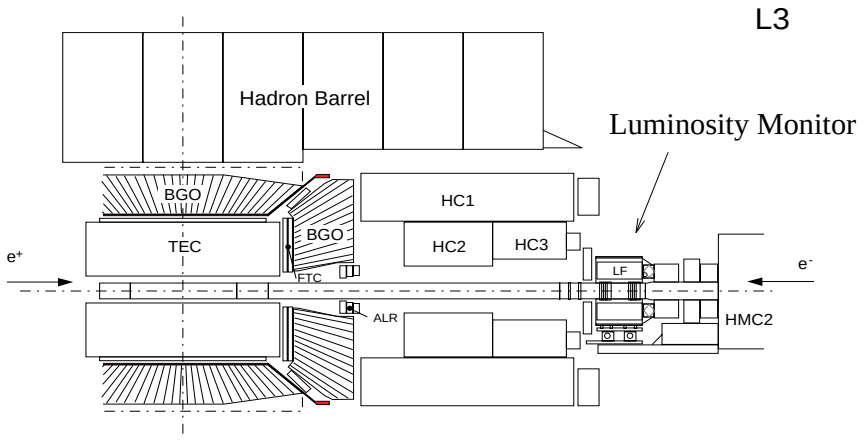

Figure 4.18: L3 Tracking and Calorimetry with Luminosity Monitor Shown.

4.2.8 Trigger

With LEP running in 4×4 bunch mode, the beams cross each 22 μs and every 11 μs in 8×8 bunch mode. The L3 detector typically requires 100 ms to fully digitize an event and write it to tape. Thus a fast, efficient trigger is needed to maximize the number of physically significant events written to tape and minimize the dead time due to beam gas events, cosmics, and events with no detectable particles.

In order to accomplish this goal, the L3 trigger has three levels which must be passed. The first, or level-1 trigger, performs a logical OR of triggers from individual subdetectors. The level-2 trigger coordinates information from more than one subdetector, while the level-3 trigger does the same in greater detail. Both the level-2 and level-3 triggers, however, pass on any event in which more than one subdetector triggered at level-1. The total event rate written to tape after the level-3 trigger is approximately 3 Hz. These triggers are described in more detail below.

Level-1 Trigger

The level-1 trigger is based on five separate subdetector groups: the TEC, the calorimetry, the scintillators, the muon chambers, and the luminosity monitor. Level-1 logically OR's these five groups, resulting in a typical trigger rate of less than 8 Hz. With a positive result from level-1, the fine digitization electronics begin operation. The five subdetector triggers are described below.

TEC Trigger: The TEC trigger selects events with two or more charged tracks. It begins by logically ORing 14 anode wires in each of the 24 outer TEC sectors.

If an outer sector has detected a track, the TEC trigger examines the event more closely, requiring there be at least two tracks with minimum transverse energy of 150 MeV and an acolinearity of less than 60°. The trigger rate varies with beam conditions but is typically between 1 and 4 Hz[1].

Calorimetric Trigger: The level-1 calorimetric trigger is designed to select events which deposit energy in the electromagnetic or hadronic calorimeter. These include e^+e^-, $\tau^+\tau^-$, $q\bar{q}$, and $\nu\bar{\nu}\gamma$.

The inputs to the trigger are the analog sums of several groups of BGO crystals or hadronic calorimeter towers. The BGO barrel and endcap are grouped into $32\phi \times 15\theta$ super blocks. The HCAL is split into two radial layers. The inner (outer) layer is grouped into $16\phi \times 11\theta$ ($16\phi \times 13\theta$) super blocks. The inner layer represents about one absorption length.

Events are selected if (a) the total HCAL energy exceeds 25 GeV, (b) the total BGO energy exceeds 25 GeV, (c) the HCAL barrel energy exceeds 15 GeV, (d) the BGO barrel energy exceeds 8 GeV, or (e) a single cluster is identified with at least 6 GeV of energy. If a triggered TEC track matches to the cluster in (e) above, then the threshold is lowered to 2.5 GeV. If the cluster is a single, isolated electromagnetic bump, the threshold is lowered to 1 GeV to accept single photon events. Typical rates for this trigger are 1 to 2 Hz.

Scintillator Trigger: The scintillator trigger is used at level one to select high multiplicity events. There must be at least 5 hits spread over 90°, which are all within 30 ns of the beam crossing. The rate for this trigger is approximately 0.1 Hz.

[1]Provided that LEP delivers "stable" beams.

Muon Trigger: The level-1 muon trigger requires that there be at least one loosely constructed track in the muon chambers. The track must have interacted with at least 2 of the 3 P layers and at least 3 of the 4 Z layers. The transverse momentum of the track must be at least 1 GeV. With the requirement that at least one scintillator hit be within 15 ns of the beam crossing, this trigger rejects almost all cosmics. The trigger rate from the muon chambers is then typically 1 Hz.

Luminosity Trigger: Like the calorimetric trigger, the luminosity trigger divides the luminosity monitor into 16ϕ blocks and triggers on any one of the following: back-to-back depositions with better than 15 GeV, total energy on one side greater than 25 GeV and greater than 5 GeV on the other side, or total energy in either end greater than 30 GeV. Typical trigger rates are 1.5 Hz, but as with the TEC trigger, this varies with beam conditions.

Level-2 Trigger

Level-2 decisions are based on the coarse information available at level-1, the level-1 decisions made, and more processed data. It's task is to reject background events, such as calorimetric noise, beam-gas events, beam-wall interactions, and synchrotron radiation, by coordinating information from more than one subdetector. Any event with more than one level-1 trigger is simply passed on to the level-3 trigger. The level-2 trigger rate is typically 6 Hz.

Level-3 Trigger

The level-3 trigger applies criteria based on the full detector information. As with level-2, events with more than one level-1 trigger are simply passed on and written to tape. Events with only one level-1 trigger invoke selection criteria based on the detector which triggered the event. For example, the calorimeter algorithm redetermines the event energies based on more detailed information. This allows energy thresholds to be more finely tuned. Luminosity triggers are simply passed on. Muon triggers are required to have a scintillator hit within 10 ns of the beam crossing and must be within 60° of the scintillator hit. Tracks resulting in a TEC trigger must at this level be correlated with at least 100 MeV of calorimetric energy, pass quality tests, and point to a common vertex. The final event rate from the level-3 trigger varies between 2 and 3 Hz.

4.2.9 Off-line Event Reconstruction

The off-line event reconstruction takes place in several stages. First, the information from each subdetector is reconstructed and subdetector objects are determined. Then from these subdetector objects, higher level objects are constructed which characterize the kinematics of a given event. At this point, only kinematic variables have been determined. Particle identification is left up to the various analysis groups.

Reconstructed events are written to tape in several formats. The most comprehensive is the Master Data REconstruction (MDRE) format, which includes all of the reconstructed objects as well as the information needed to perform the reconstruction again. The second largest format is the Data SUmmary (DSU) format,

which includes the reconstructed objects and information needed to reconstruct some of the objects. Many analyses depend on this, since things like the HCAL energy observed in a cluster depend on your assumption about what particle deposited the energy. The shortest format is the Data "aVaNti"[2] (DVN), which contains only the higher level reconstructed objects. This format is useful for a quick feasibility study for many analyses, but does not contain enough information for all analyses. [70]

4.2.10 Detector Simulation

The L3 detector simulation takes places in three steps. First one chooses the appropriate event generator. The event generator determines the final state kinematics for a given type of physics. As an example, consider the τ event in figure 4.19 below. The event generator determines the kinematics for all particles involved in the event up to the final state. The kinematics of the event are then passed to the L3 simulation program.

The simulation program takes an event and propagates it through an "ideal" L3 detector. It takes into account multiple scattering by particles in the detector material, bremsstrahlung, shower simulation, etc. It also determines the ideal response of each detector element, producing an event in the same format expected from data. This information, along with the additional information known from the generator, is passed on to the reconstruction program.

Given a simulated event, the reconstruction program behaves somewhat differently than it does for a real data event. The simulated events have, up to this point, passed through a perfect L3 detector. The reconstruction program inserts

[2] Italian for 'go ahead,' perhaps here with the connotation of doing something quickly.

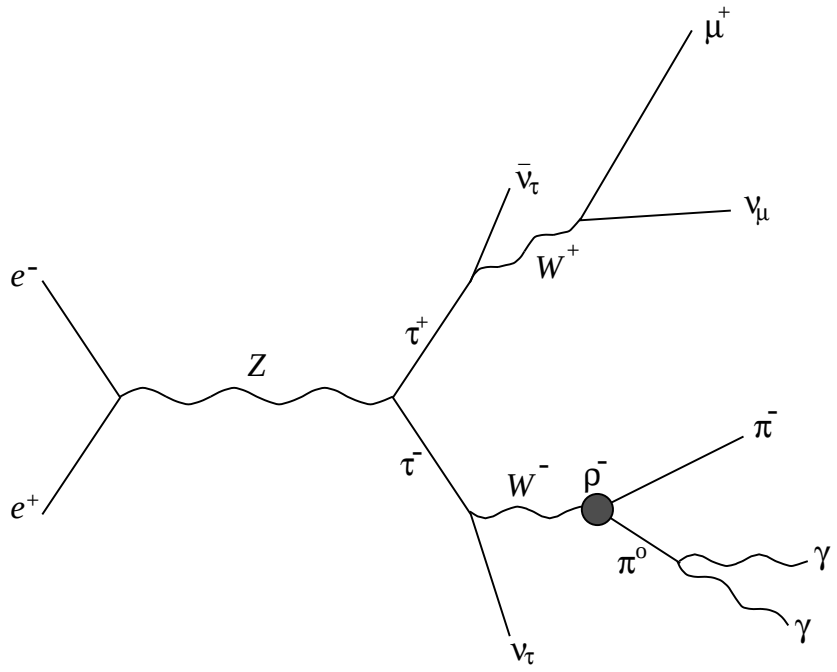

Figure 4.19: A τ Event Showing the Final State Particles.

known problems into the event reconstruction such as bad crystals in the BGO, detection efficiency in the muon chambers, high voltage trips in the TEC, and energy scales in the HCAL. All of these corrections are determined through an iterative process in which simulated data is compared to real data.

The end result is a detector simulation which makes possible searches for rare processes, or "new physics," as well as more direct measurements of the parameters of the standard model.

Chapter 5

Event Selection

Particle identification in τ decays at L3 takes place in three separate steps. The first uses global event characteristics to reject hadronic Z decays, cosmic ray events, two–photon events, and beam gas events. The result is a sample of dilepton events with no bias towards any particular flavor, *i.e.* e^+e^-, $\mu^+\mu^-$, and $\tau^+\tau^-$.

In the second step, each event is divided into two hemispheres by a plane perpendicular to the thrust axis. Particle identification then proceeds independently in each hemisphere. The result is the classification of each hemisphere as either a $\tau^- \to e^-\bar{\nu}_e\nu_\tau$, $\tau^- \to \mu^-\bar{\nu}_\mu\nu_\tau$, $\tau^- \to \pi^-\nu_\tau$, $\tau^- \to \rho^-\nu_\tau$, or $\tau^- \to a_1^-\nu_\tau$ decay. At this point, the other two possible dilepton event types, e^+e^- and $\mu^+\mu^-$, have not explicitly been rejected.

The third step in particle identification again uses global event characteristics to reject the non–τ backgrounds. The primary sources for these are e^+e^-, $\mu^+\mu^-$, two–photon, and cosmic ray events.

The sample of events of interest here are those in which at least one hemisphere was selected as either $\tau^- \to \pi^-\nu_\tau$ or $\tau^- \to \rho^-\nu_\tau$. In this chapter, we describe

the preselection procedure, the identification of π's and ρ's, and the final cuts to eliminate non–τ backgrounds.

5.1 Lepton Flavor Blind Preselection

The lepton flavor blind preselection consists primarily of removing non–dilepton events form the data sample. These non–τ events consist primarily of the following:

- Beam gas.
- Cosmic rays.
- Two–photon events.
- $Z \rightarrow q\bar{q} \rightarrow$ hadrons.

The rejection of these events is achieved through the global event characteristics typical of each.

Beam gas events typically consist of many tracks which curl up within the central tracking. In addition, these tracks in general do not pass through the nominal interaction point. These events are rejected by the combination of cuts which reject the other non–τ event types.

A cosmic ray event is shown in figure 5.1. Since cosmic rays originate from sources other than the experiment, they are completely uncorrelated with the production of Z bosons. Most cosmic rays are rejected by requiring that the scintillator hits due to the cosmic ray are within 2 ns of the expected crossing time. Additional cosmic rays are rejected by initially requiring that they pass within 10 mm of the nominal event vertex. In the final selection detailed in section 5.3, this cut is tightened to 2 mm.

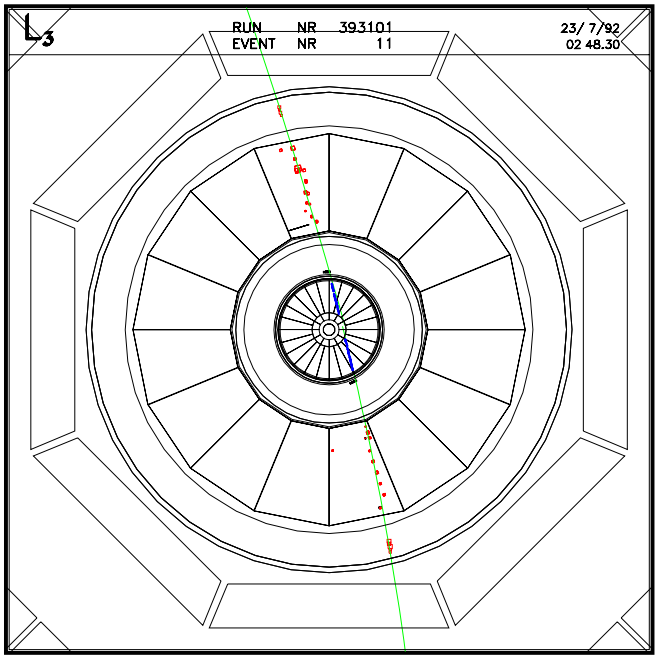

Figure 5.1: A cosmic ray event.

Two–photon events arise from the process $e^+e^- \rightarrow e^+e^-f^+f^-$, where f^+f^- is any fermion pair. The e^+e^- pair in the final state of the above interaction are, in fact, the initial state electron–positron pair. They are typically scattered at very low angles and proceed down the beam pipe undetected. The fermion pair produced from the two–photon interaction also tends to have a total momentum directed along the beam axis, as illustrated in figure 5.2. These events are suppressed by requiring that

- at least one TEC track have a measured momentum above 0.5 GeV.
- the transverse momentum imbalance between the two sides must be greater than 1 GeV if the total calorimetric energy is less than 15 Gev.

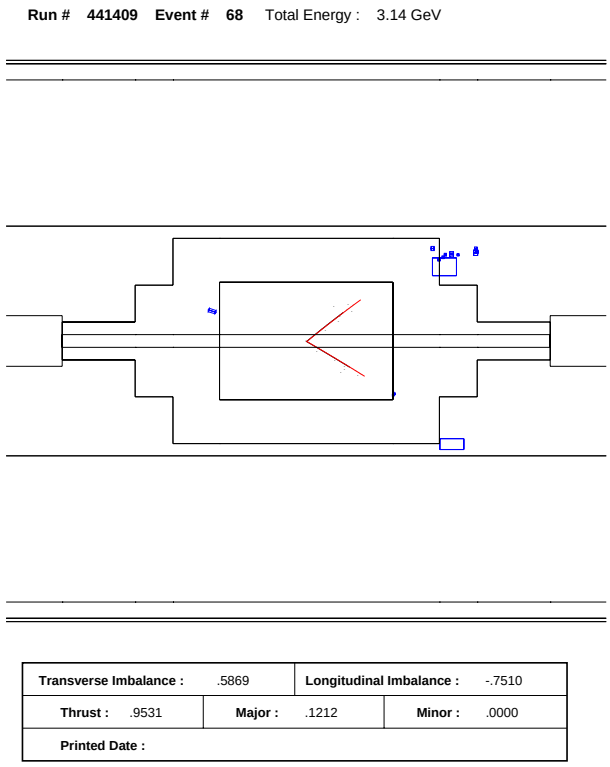

Figure 5.2: A two–photon event.

- the opening angle between the two tracks be greater than 1.7 radians.

The second cut above removes very few $Z \rightarrow \tau^+\tau^-$ events, because the neutrinos in τ events with little visible energy typically cause the momentum on each side to be unbalanced. The last cut above is tightened to 2.8 radians in the final selection.

Hadronic decays of the Z are characterized by many tracks spread out over a large region in the detector. For comparison to a τ event, consider figures 5.3 and 5.4. Thus $Z \rightarrow q\bar{q} \rightarrow$ hadrons events are rejected by requiring the following:

- no more than 6 TEC tracks in an event.
- no more than 5 TEC tracks in either hemisphere.

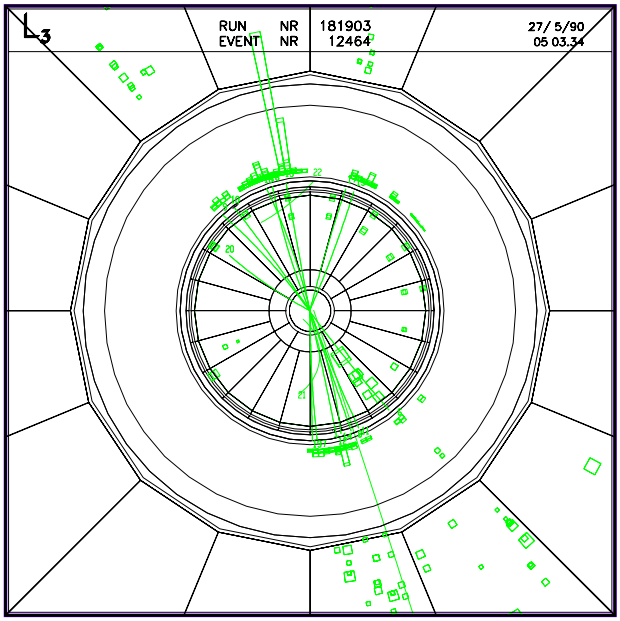

Figure 5.3: A typical hadronic event.

- no more than 20 BGO clusters.
- the maximum angle between any TEC track and the thrust axis for the event must be less than 20°.

Estimates form Monte Carlo studies indicate that these cuts remove 99.9% of all $Z \rightarrow$ harons events and reject less than 2% of all dilepton events.

After all of these cuts, the preselected sample contains roughly 98% of all leptonic decays of the Z as well as $e^+e^- \rightarrow \gamma \rightarrow \ell^+\ell^-$ events and $e^+e^- \rightarrow e^+e^-$ events occurring through photon exchange. The backgrounds from cosmics, two–photon events, and hadronic Z decays is approximately 5%.

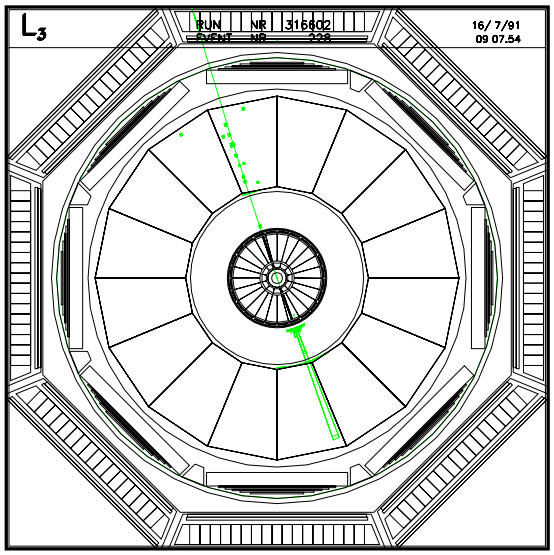

Figure 5.4: A $\tau^+\tau^- \to e\mu$ event.

5.2 Particle Identification

Events which pass all preselection cuts are divided into hemispheres by a plane perpendicular to the thrust axis. Particle identification then proceeds separately in each hemisphere using only information from the hemisphere being considered. This method allows the non–τ background to pass through to the final step, where global event characteristics are used to both suppress the background and estimate the fraction remaining.

The identification of pions, rhos, and other tau decay products depends on the measured track momentum, the distribution of energy in the BGO and HCAL, and the response of the muon chambers. The expected response of each portion

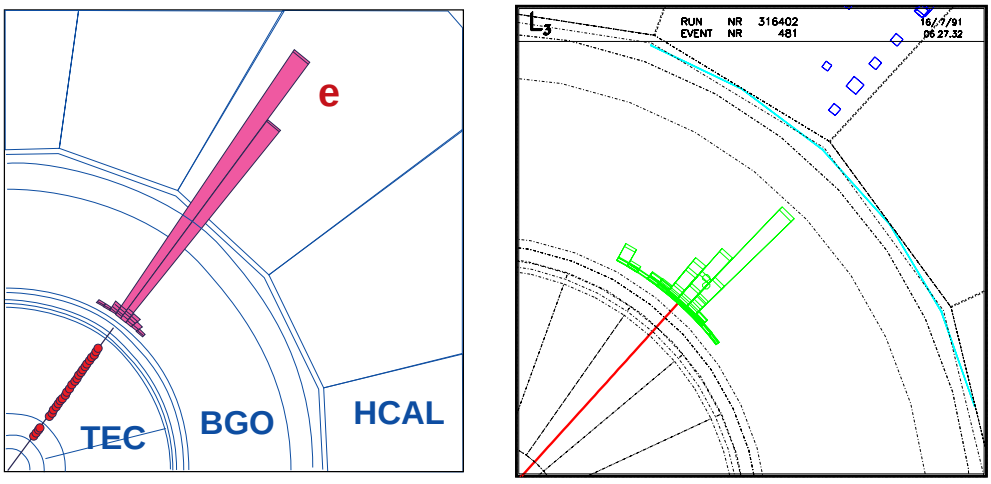

Figure 5.5: A comparison of an electromagnetic shower on the left and a hadronic showers on the right in the BGO.

of the detector to different particle types has been determined through test beam studies. [71] For the one–pronged hadronic decays of the τ, our understanding of the calorimetric response is crucial. Below we describe the essential differences between the calorimetric responses to hadrons and electrons or photons, and how we extract neutral π^0 clusters from the hadronic shower.

5.2.1 Electromagnetic and Hadronic Showers

Figure 5.5 illustrates the differences between electromagnetic showers in the BGO from electrons and photons and hadronic showers from pions. Narrow, symmetric profiles are typical of electrons, while broad, asymmetric profiles typify hadrons.

To differentiate between the two, an electromagnetic chi–squared (χ^2_{em}) is formed

for each shower. It is defined by

$$\chi^2_{em} = \sum_{i=1}^{6} \left[\frac{F_i^{meas} - F_i^{pred}}{\sigma_i^{pred}} \right]^2 , \tag{5.1}$$

where F_i^{meas} is the measured fraction of the total energy in the i–th most energetic crystal, F_i^{pred} is the predicted fraction based on test beam data and bhabha studies, and σ_i^{pred} is the width of the observed variation about F_i^{pred} in test data. The overall shower shape was found to be relatively independent of energy above 1 GeV. As illustrated in figure 5.6, the expected fraction of electromagnetic energy in a given crystal is determined by distributing that energy in concentric rings about the impact point of the charged track. For true electromagnetic showers, χ^2_{em} is on the order of 10. For hadronic showers in the BGO, a typical value is 150.

Based on Monte Carlo studies, hadronic shower profiles may be constructed in a similar manner. The ability to predict the shape of both types of showers forms the basis of the separation of electromagnetic and hadronic showers discussed below.

5.2.2 π^0 Extraction from Hadronic τ Decays

The ability to distinguish between the following one–pronged hadronic decays of the τ: $\tau^- \to \pi^-\nu_\tau$, $\tau^- \to \rho^-\nu_\tau$ ($\rho \to \pi\pi^0$), and $\tau^- \to a_1^-\nu_\tau$ ($a_1 \to \pi\pi^0\pi^0$), depends on separating overlapping hadronic and electromagnetic showers. The large boost of the τ causes the decay products to fall within a tight cone only 40–100 mrad wide.

The algorithm for separating the clusters incorporates information from the TEC track and BGO crystals in a 30° half–cone around the charged track. Figure 5.7 illustrates the following iterative procedure used to determine the hadronic and electromagnetic content of each shower:

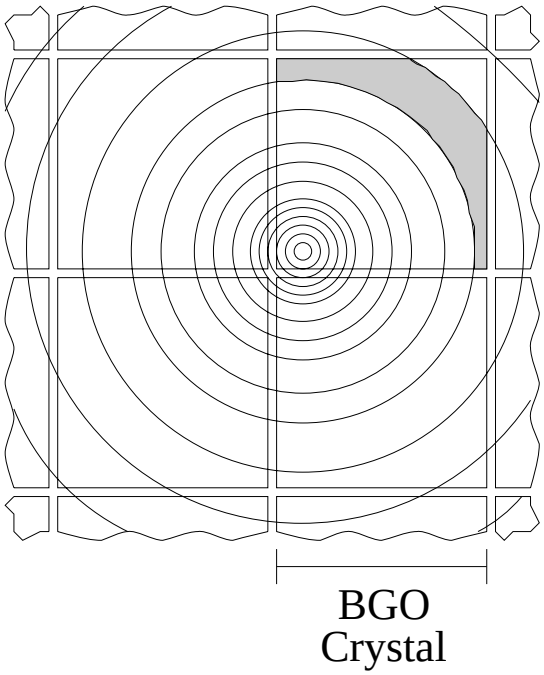

Figure 5.6: Expected energy in the BGO is estimated using concentric rings.

1. The TEC track impact point in the BGO is assumed to be the charged hadron impact point (figure 5.7(a)).

2. The hadronic shower profile is normalized to the energy in the central crystal determined by the track impact point, and the expected energy in the surrounding crystals is estimated as in figure 5.6. This yields the first estimate of the hadronic shower (figure 5.7(b)).

3. The estimated hadronic energy in each crystal is subtracted from the shower, and any remaining local maxima become photon cluster candidates (figure 5.7(c)).

4. The impact point and energy of photon candidates are determined by fitting

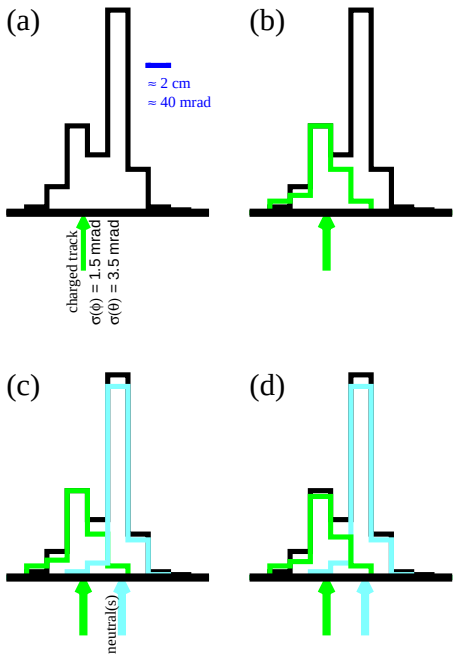

Figure 5.7: Charged and neutral shower separation in the BGO. (a) Charged hadron energy is estimated from track momentum. (b) Charged hadron energy is subtracted. (c) Remaining energy estimates that deposited by any neutral particles. (d) An iterative procedure is used to get the best overall fit.

the observed energy distributions with electromagnetic shower profiles. If the fit performs better using two profiles, the cluster is split.

5. The photon cluster candidates thus formed are now subtracted from the total BGO shower and a new estimate of the hadronic shower normalization is obtained (figure 5.7(d)).

Steps 2 through 5 of this procedure are iterated until the estimated energies in each cluster is stable to within 1%. Typically three to four iterations are required.

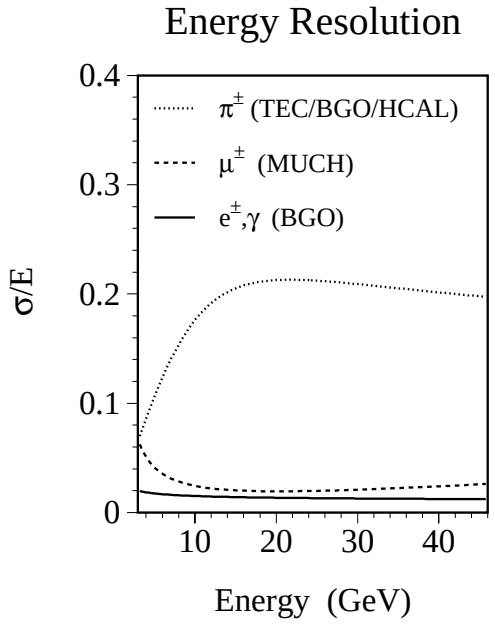

Figure 5.8: The single pion energy resolution obtained using tracking and calorimetric information along with muon and electron energy resolution.

After the final iteration, any remaining energy is grouped with the hadronic shower. This is then combined with any observed HCAL energy to form the total calorimetric response to the hadron. Computation of the total hadronic energy then uses a combination of the total hadronic shower energy and the measured track momentum. At low transverse momentum, the tracking information dominates the measurement of hadronic energy, while at high transverse momentum, the calorimetry dominates the measurement. Figure 5.8 illustrates the resulting single pion energy resolution.

Based on the electromagnetic shower shapes obtained through the above procedure, π^0 candidates are formed from the following:

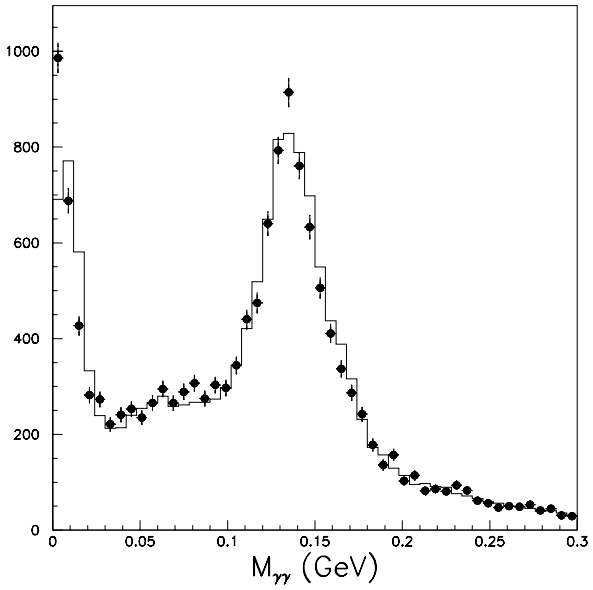

Figure 5.9: The reconstructed mass of π^0 candidates from both one and two clusters. The dots are data and the solid line the Monte Carlo prediction.

- any single cluster with more than 1 GeV total energy and a $\chi^2_{em} < 20$.
- any split cluster for which the invariant mass of the two photons is within 50 MeV of the π^0 mass.
- any two clusters for which the invariant mass of the two photons is within 40 MeV of the π^0 mass.

Figure 5.9 illustrates the resulting reconstructed π^0 mass for both data and Monte Carlo.

5.3 Final Selection and Background Estimation

The final step in the identification of pions and rhos combines all of the information from a hemisphere in making the identification. To reject non–τ backgrounds, information from the opposite hemisphere is used. For the measurement of the τ neutrino helicity, this selection process has been restricted to the fiducial volume defined by $|\cos\theta| < 0.7$.

5.3.1 Selection of $\tau^- \to \pi^-\nu_\tau$

The selection of an event in a hemisphere as $\tau^- \to \pi^-\nu_\tau$ begins with rejecting any decays identified as $\tau^- \to e^-\bar{\nu}_e\nu_\tau$ or $\tau^- \to \mu^-\bar{\nu}_\mu\nu_\tau$. In essence this means the following must be true:

- the χ^2_{em} that the calorimetric energy deposited was purely electromagnetic must be bad.
- the calorimetric response must not be in agreement with a minimum ionizing particle signature.
- there must be no track in the muon chambers matched to a track in the TEC.

The first item rejects electrons, while the second and third reject muons, while allowing for the occasional punch–through. The nine interaction lengths of material in the barrel do not guarantee that all pions will be stopped before entering the muon chamber system. Pions which do punch–through, however, typically scatter and are of very low momentum, so that the track in the MUCH does not align

with the track in the TEC. In such cases, the measured momentum in the MUCH is added to the calorimetric energy in determining the total pion energy.

Any remaining events are considered pion candidates. These events must then pass the following selection criteria:

- the shower in the BGO must be asymmetric and consistent with a π^-.
- the total hadronic shower energy including the BGO and HCAL must be consistent with the track momentum.
- no neutral particles with energy greater than 0.5 GeV and no must have been reconstructed.

Here the first two cuts are positive selection cuts for $\tau^- \to \pi^- \nu_\tau$ while the third rejects $\tau^- \to \rho^- \nu_\tau$ and $\tau^- \to a_1^- \nu_\tau$ events. The primary background for $\tau^- \to \pi^- \nu_\tau$ events is $\tau^- \to \rho^- \nu_\tau$ events in which the π^0 was very soft and lost in the hadronic shower.

At this point, the final cuts against non–τ backgrounds are made. These cuts are illustrated in figure 5.10. Knowing the shape of the relevant background removed by each cut, one may estimate the number of background events remaining in the sample from the number removed by the cut. To reject non–τ backgrounds which fake pions, we require the following:

- for the rejection of bhabhas,

  the track in the opposite hemisphere must point into a good region of the BGO.

  the reconstructed electron energy in the opposite hemisphere together with any other electromagnetic deposits must be less than 42 GeV.

- for the rejection of dimuons,

  there must be no muon track in the opposite hemisphere with energy greater than 42 GeV.

  if there is no muon track, the HCAL response must not be that of a minimum ionizing particle.

- for the rejection of two–photon events,

  the opening angle between the tracks on either side of the event must be greater than 2.8 radians.

- for the rejection of cosmic rays,

  the scintillator timing must match with the beam crossing.

  the shortest distance between the track and the nominal vertex must be lest than 2 mm.

This set of cuts rejects bhabhas which occasionally fake pions by either passing through a crack between BGO crystals and showering in the HCAL or by showering very late and having significant energy deposits in the HCAL. Similarly it rejects muons which stop and shower in the HCAL, faking pions. It rejects two–photon events which fake $\tau^- \to \pi^-\nu_\tau$ events in a variety of ways, included producing real $\tau^+\tau^-$ pairs one or more of which may decay to a pion. It rejects cosmic rays which fake $\tau^- \to \pi^-\nu_\tau$ events by passing through the detector and stopping in the HCAL. The total non–τ background in events with only one selected pion is 3.4% consisting of 0.8% from bhabhas, 0.3% from dimuons, 1.7% from two–photon events, and 0.6% from cosmic rays. For events in which both τ decays are identified as pions, the total non–τ background drops to 0.6%.

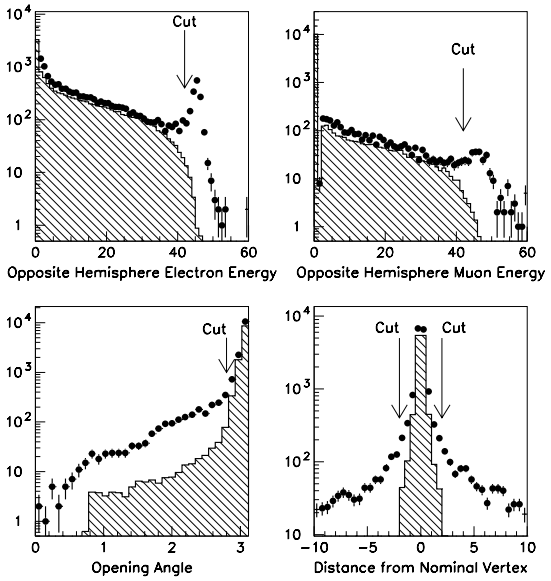

Figure 5.10: The final selection cuts to eliminate non–τ backgrounds from selected pions. The dots are data and the shaded region the signal.

After all of these cuts, the final $\tau^- \to \pi^- \nu_\tau$ sample is obtained. The overall efficiency of these cuts obtained from Monte Carlo in the fiducial volume is 74%. The background from other τ decays, estimated from Monte Carlo, is 13.9% when a single side is identified as a pion and 26.5% when both sides have been identified as a pion.

5.3.2 Selection of $\tau^- \to \rho^- \nu_\tau$

As with the pion, the first step in the selection of an event in a hemisphere as $\tau^- \to \rho^- \nu_\tau$ is to reject any decays identified as either $\tau^- \to e^- \bar{\nu}_e \nu_\tau$ or $\tau^- \to \mu^- \bar{\nu}_\mu \nu_\tau$.

Since this process was detailed in the previous section, we do not reiterate it here. The remaining events are considered to be rho candidates. To be selected as a rho, an event must satisfy the following criteria:

- there must be one or more clusters in BGO consistent with the presence of a single π^0.
- the total hadronic energy in the BGO and HCAL must be consistent with the track momentum.
- the invariant mass of the reconstructed $\pi^-\pi^0$ system must be between 0.45 and 1.20 GeV.

Here the first cut rejects $\tau^- \to a_1^-\nu_\tau$ events, which comprise the largest background for the $\tau^- \to \rho^-\nu_\tau$ channel.

Again the final cuts against non–τ backgrounds are made at this point. These cuts are illustrated for the rho in figure 5.11. As with the pion, the number of events removed by each cut is used to estimate the background remaining in the selected events. The cuts are as follows:

- for the rejection of bhabhas,

  the track in the opposite hemisphere must point into a good region of the BGO.

  the reconstructed electron energy in the opposite hemisphere together with any other electromagnetic deposits must be less than 42 GeV.

- for the rejection of dimuons,

  there must be no muon track in the opposite hemisphere with energy greater than 42 GeV.

if there is no muon track, the HCAL response must not be that of a minimum ionizing particle.

- for the rejection of two–photon events,

  the opening angle between the tracks on either side of the event must be greater than 2.8 radians.

- for the rejection of cosmic rays,

  the scintillator timing must match with the beam crossing.

  the shortest distance between the track and the nominal vertex must be lest than 2 mm.

The total non–τ background remaining after these cuts is estimated from data to be 0.8% for events with a single hemisphere identified as a rho. The contributions to this are 0.4% from bhabhas and 0.4% from dimuons. Two–photon events and cosmics contribute a negligible background. For events in which both decays are identified as rho's, the non–τ background is negligible.

Events passing all of the above cuts are considered to be rhos. The overall selection efficiency, estimated from Monte Carlo, is 70%. The contribution from other τ decays is estimated at 11.7% for events with a single rho, and at 22.4% for events with two identified rhos. Figure 5.12 illustrates the reconstructed rho mass along with the fraction contributed from misidentified τ decays.

For events with one hemisphere identified as a pion and the other as a rho, the total contribution from misidentified τ decays is 24.6%. The contribution from non–τ background is negligible. A selected π–ρ event is shown in figure 5.13.

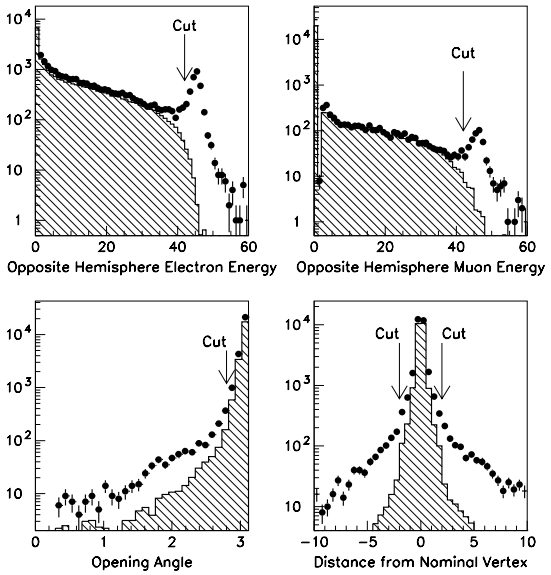

Figure 5.11: The final selection cuts to eliminate non–τ backgrounds from selected rhos. The shaded areas are the desired signal from Monte Carlo. The dots are data.

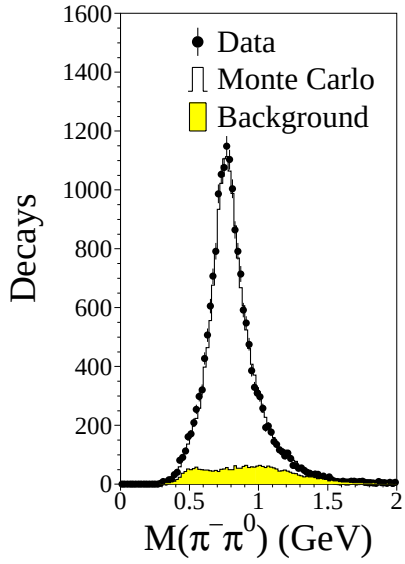

Figure 5.12: The reconstructed rho mass from selected events. The background shown is from other τ decays. The cut on the invariant rho mass has not been used in selecting events for this plot.

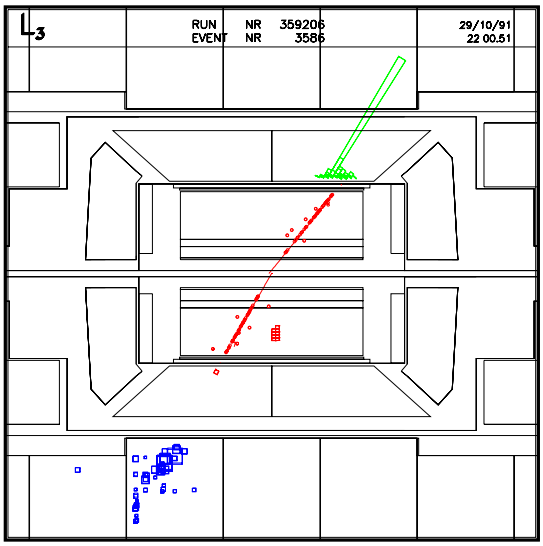

Figure 5.13: An event with a π in the lower left–hand portion of the figure and a ρ opposite to it.

Chapter 6

The Measurement of τ Polarization and Neutrino Helicity

In the previous chapter, we detailed the identification of individual τ decays as either $\tau^- \to \pi^-\nu_\tau$ or $\tau^- \to \rho^-\nu_\tau$. Each event is then classified as one of the following categories: π–X, ρ–X, π–π, π–ρ, and ρ–ρ, where X denotes any decay not explicitly identified as either a π or a ρ.

In this chapter, we present the result of the τ neutrino helicity measurement. We begin with a description of how the data and Monte Carlo distributions are each built up event–by–event. Then we describe the likelihood function used to determine the best fit for the set of quantities $\mathcal{P}_\tau$, ξ_π and ξ_ρ, and for the set $\mathcal{P}_\tau$ and ξ_h in all five distributions simultaneously. Next we present the measurement both with and without universality in $\tau^- \to \pi^-\nu_\tau$ and $\tau^- \to \rho^-\nu_\tau$ decays. Last we describe the evaluation of the systematic errors associated with the measurement, and present the final result.

6.1 Fitting Method

6.1.1 Event Binning

For each event selected in data, the values of the normalized energy x_π for pions and/or the variable ω_ρ for rhos is entered into the appropriate histogram. For example, events in data identified as π–ρ would be entered into a two–dimensional histogram with 14 bins in x_π and 20 bins in ω_ρ. Events identified as either π–π or ρ–ρ are binned such that the hemisphere with the larger value of x_π or ω_ρ is always considered first. This essentially folds the histograms across a diagonal. Built into the binning scheme used here is a basic assumption that τ decays are CP invariant.

From Monte Carlo, we build up the desired distributions $F_i(x_i)$ and $G_i(x_i)$ $(i = \pi, \rho)$ described in Chapter 3 by considering each hemisphere separately. The fully simulated Monte Carlo yields directly the following linear combinations of F_i and G_i:

$$H_i^+(x_i) = \frac{1 - \mathcal{P}_\tau^{MC}}{2}(F_i(x_i) + G_i(x_i)) \tag{6.1}$$

and

$$H_i^-(x_i) = \frac{1 + \mathcal{P}_\tau^{MC}}{2}(F_i(x_i) - G_i(x_i)), \tag{6.2}$$

which correspond to the two helicity states of the τ^-. The value $\mathcal{P}_\tau^{MC}$ is the τ polarization used in creating the Monte Carlo sample and determines the relative weights of the two samples above.

Since the actual τ decay products are known event–by–event, these histograms are divided into twelve groups denoted by $H_i^{\pm j}$, where the subscript i labels the event as being selected as either a π or ρ and the superscript j labels the τ decay as actually being a π, ρ, or some *other* τ decay. Similarly, we define twelve

distributions denoted by $F_i^j(x_i)$ and $G_i^j(x_i)$. These are given by

$$F_i^j(x_i) = \frac{H_i^{+j}(x_i)}{1 - \mathcal{P}_\tau^{MC}} + \frac{H_i^{-j}(x_i)}{1 + \mathcal{P}_\tau^{MC}} \tag{6.3}$$

and

$$G_i^j(x_i) = \frac{H_i^{+j}(x_i)}{1 - \mathcal{P}_\tau^{MC}} - \frac{H_i^{-j}(x_i)}{1 + \mathcal{P}_\tau^{MC}}. \tag{6.4}$$

It is these final distributions, represented by a set of histograms, which form the basis for the likelihood function of the next section.

6.1.2 The Likelihood Function

Based on the application of Poisson statistics in each bin, we form the total, binned likelihood of observing the set of parameters ($\mathcal{P}_\tau$,ξ_π,ξ_ρ) as the product of the individual likelihoods of each of the five data distributions. The total likelihood is then

$$\mathcal{L}(\mathcal{P}_\tau, \xi_\pi, \xi_\rho) = \mathcal{L}_{\pi X} \cdot \mathcal{L}_{\rho X} \cdot \mathcal{L}_{\pi\pi} \cdot \mathcal{L}_{\pi\rho} \cdot \mathcal{L}_{\rho\rho}. \tag{6.5}$$

To take advantage of existing numerical packages for minimization and to avoid the computationally difficult task of multiplying the probabilities bin–by–bin together, we in fact minimize the negative log of the likelihood. This is equivalent to maximizing the likelihood. Thus we seek minimum of the quantity

$$-\ln \mathcal{L}(\mathcal{P}_\tau, \xi_\pi, \xi_\rho) = -\ln \mathcal{L}_{\pi X} - \ln \mathcal{L}_{\rho X} - \ln \mathcal{L}_{\pi\pi} - \ln \mathcal{L}_{\pi\rho} - \ln \mathcal{L}_{\rho\rho} \tag{6.6}$$

as a function of the variables $\mathcal{P}_\tau$, ξ_π, and ξ_ρ.

The likelihood for any given channel may be written as

$$\mathcal{L} = \prod_j P(m_j; \mu_j), \tag{6.7}$$

where j runs over all of the bins in the channel. We have denoted the probability of observing m_j events in data given the expected number of events μ_j from Monte Carlo as $P(m_j;\mu_j)$. Applying Poisson statistics,

$$P(m_j;\mu_j) = \frac{\mu_j^{m_j}}{m_j} e^{-\mu_j}. \tag{6.8}$$

For clarity, in the channels for which both hemispheres have been identified, we rewrite this as

$$P(m_{ij};\mu_{ij}) = \frac{\mu_{ij}^{m_{ij}}}{m_{ij}} e^{-\mu_{ij}}, \tag{6.9}$$

where the subscript i now runs over all bins along one axis and the j runs over all bins along the other. For the π–π and ρ–ρ distributions, $j \leq i$.

For the π–X distributions, the expected number of events in the j–th bin is given by

$$\begin{aligned} \mu_j &= N_{\pi X}\Big[(F_\pi^\pi(j) - \mathcal{P}_\tau \xi_\pi G_\pi^\pi(j)) + (F_\pi^\rho(j) - \mathcal{P}_\tau \xi_\rho G_\pi^\rho(j)) \\ &+ \Big(F_\pi^{other}(j) + \mathcal{P}_\tau G_\pi^{other}(j)\Big) + f_\pi^{non-\tau}(j)\Big], \end{aligned} \tag{6.10}$$

where $N_{\pi X}$ is the total number of events selected as π–X and $f_\pi^{non-\tau}(j)$ is the expected non–τ background fraction in the j–th bin. Similarly, for the ρ–X distributions, we have

$$\begin{aligned} \mu_j &= N_{\rho X}\Big[\Big(F_\rho^\pi(j) - \mathcal{P}_\tau \xi_\pi G_\rho^\pi(j)\Big) + \Big(F_\rho^\rho(j) - \mathcal{P}_\tau \xi_\rho G_\rho^\rho(j)\Big) \\ &+ \Big(F_\rho^{other}(j) + \mathcal{P}_\tau G_\rho^{other}(j)\Big) + f_\rho^{non-\tau}(j)\Big]. \end{aligned} \tag{6.11}$$

Note that in both equations, the background from τ decays other than the π or ρ is assumed to be produced through strictly $V-A$ currents.

The expected number of events in a given bin of the two–dimensional histograms has many more terms, both because of the correlations between the two

hemispheres of the event and because of the increased number of combinations of correctly and incorrectly identified decays. For the π–π, π–ρ, and ρ–ρ events, the expected number of events in the i–th pion bin and the j–th rho bin is given by

$$\mu_{ij} = N_{ab} \sum_{h_1} \sum_{h_2} \left[c_{ij}^{ab} \left(F_\pi^{h_1}(i) F_\rho^{h_2}(j) - \mathcal{P}_\tau (\xi_{h_2} F_\pi^{h_1}(i) G_\rho^{h_2}(j) + \xi_{h_1} G_\pi^{h_1}(i) F_\rho^{h_2}(j)) \right. \right. \quad (6.12)$$

$$\left. \left. + \xi_{h_1} \xi_{h_2} G_\pi^{h_1}(i) G_\rho^{h_2}(j) \right) + f_{\pi\rho}^{non-\tau}(i,j) \right],$$

where h_1 and h_2 are summed over π, ρ, and *other* τ decays and the chirality parameter for $\xi_{other} = -1$. The value of N_{ab} corresponds to the number of events selected for the decay being considered. For the π–ρ distribution, $c_{ij}^{\pi\rho} = 1$; however, for the π–π and ρ–ρ distributions,

$$c_{ij}^{\pi\pi} = c_{ij}^{\rho\rho} = \begin{cases} 1 & i = j. \\ 2 & i \neq j. \end{cases} \quad (6.13)$$

In this way, the likelihood function takes into account the fact that the π–π and ρ–ρ distributions in data have been folded across the diagonal.

To obtain the likelihood functions for the fit with universality between the π and the ρ, the above equations are simply rewritten with $\xi_\pi \equiv \xi_\rho = \xi_h$. The result of both fits is reported in the section below.

6.2 The Measurement

Here we report the result of performing the minimization of the negative, of the log, of the likelihood function described above. The minimization is carried out through the interactive package MINUIT [63] over both parameter spaces, $(\mathcal{P}_\tau, \xi_\pi, \xi_\rho)$ and $(\mathcal{P}_\tau, \xi_h)$. Then, with the central values in hand, the evaluation of the major systematic uncertainties in the measurement is presented.

Decay Mode	No. of Events
π–X	6498
ρ–X	12544
π–π	404
π–ρ	1472
ρ–ρ	1561

Table 6.1: The number of events selected in each decay mode.

6.2.1 The Fit With and Without π/ρ Universality

Initially we make the assumption that the τ neutrino helicity when $\tau^- \to \pi^-\nu_\tau$ and the τ neutrino helicity when $\tau^- \to \rho^-\nu_\tau$ may not be the same. Thus we assume that ξ_π and ξ_ρ are not necessarily equal and treat them both as free parameters. Performing the fit for all three parameters, $\mathcal{P}_\tau$, ξ_π, and ξ_ρ using our selected sample of events as listed in table 6.1, we obtain

$$\mathcal{P}_\tau = -0.162 \pm 0.017, \tag{6.14}$$

$$\xi_\pi = -1.005 \pm 0.095, \tag{6.15}$$

and

$$\xi_\rho = -0.935 \pm 0.067. \tag{6.16}$$

The total χ^2 of the fit is 1.013 for 614 degrees of freedom. The correlation coefficients between the parameters are given in table 6.2.

The assumption, however, that ξ_π and ξ_ρ need not be the same is not well motivated. In fact, one would expect to obtain the same average neutrino helicity in both decays, given infinite statistics and no systematic errors. Treating them as

	ξ_π	ξ_ρ
$\mathcal{P}_\tau$	-0.215	-0.327
ξ_π		-0.186

Table 6.2: The correlation coefficients in the fit for $\mathcal{P}_\tau$, ξ_π, and ξ_ρ.

different simply allows one to see how the systematic uncertainties evaluated later change the information in the pion and rho separately.

The final fit over the two–dimensional parameter space ($\mathcal{P}_\tau$,ξ_h) yields the result

$$\mathcal{P}_\tau = -0.162 \pm 0.017, \tag{6.17}$$

and

$$\xi_h = -0.960 \pm 0.051. \tag{6.18}$$

The total χ^2 per degree of freedom for the fit is 1.012 for 615 degrees of freedom. The correlation coefficient between $\mathcal{P}_\tau$ and ξ_h is -0.437. The result of the fit is shown for the π–X, ρ–X, and π–ρ distributions in figures 6.1, 6.2, and 6.3 respectively. In tables 6.3 through 6.7, the composition of the data is given as estimated from Monte Carlo for the misidentified τ decays and from data for the non–τ backgrounds.

6.2.2 Evaluation of Systematic Errors

Systematic uncertainties fall into three general classes, uncertainties in the detector, uncertainties in the method, and statistical fluctuations in data. The most important systematic uncertainties have been evaluated and presented here. They are estimated by varying the branching ratios of the τ decays, the background con-

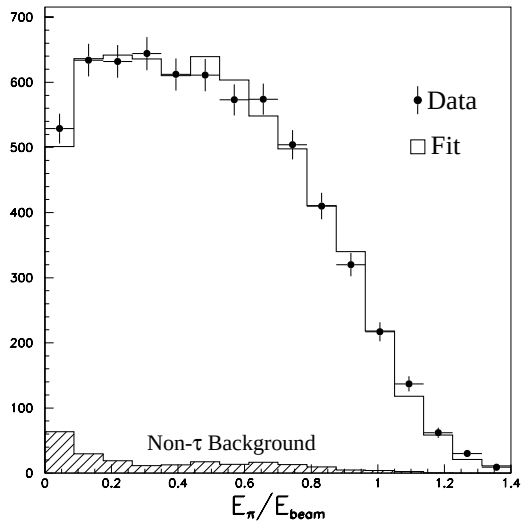

Figure 6.1: The pion normalized energy distribution along with the best fit of Monte Carlo to data.

tamination, the most important selection cuts, and the energy scales of different subdetectors. [33]

The systematic uncertainty in the composition of the background from other τ decays was evaluated by varying the branching ratios of all τ decays within the limits of L3's measurement of those branching ratios [72, 73]. Background from bhabhas, dimuons, two–photon interactions and cosmics is estimated from data, and the statistical uncertainty on the normalization is on the order of 10%. The systematic error due to the shape of the non–τ background is negligible compared to the normalization.

The accuracy of the BGO energy scale for electromagnetic clusters is estimated to be 1% at 1 GeV based on the position of the π^0 peak and 0.1% at 45 GeV from

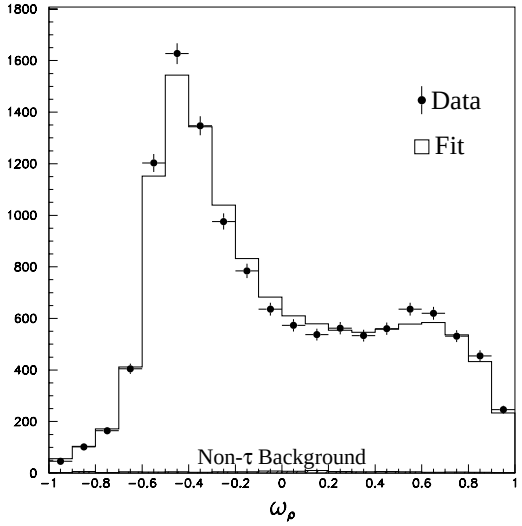

Figure 6.2: The rho distribution in the variable ω_ρ along with the best fit of Monte Carlo to data.

a study of bhabha events. From the position of the ρ invariant mass peak, the BGO and HCAL response to hadronic energy deposits may be off by as much as 1.5%. The momentum scale of the TEC is know to within 1% from 1 to 45 GeV using both low energy electrons and muons from the decay of τ's as well as Z's.

The result of varying each of the above within the uncertainties given is summarize in tables 6.8 and 6.9. In addition, there is an overall shift of -0.0032 in the measured value of $\mathcal{P}_\tau$ due to radiative corrections. These were obtained from the analytical program ZFITTER [48, 49], which takes into account initial and final state radiation, γ–exchange, and γ–Z interference. The final result, with both statistical and systematic errors, is presented in Chapter 7.

Decay	% of Signal
π	82.8
K	4.9
ρ	4.4
e	1.1
μ	1.5
a_1	0.3
K^*	1.7
Non–τ	3.4

Table 6.3: The composition of the signal in π–X events.

Decay	% of Signal
ρ	87.2
a_1	5.6
K^*	2.2
π	2.3
e	0.7
μ	0.8
K	0.1
Non–τ	0.8

Table 6.4: The composition of the signal in ρ–X events.

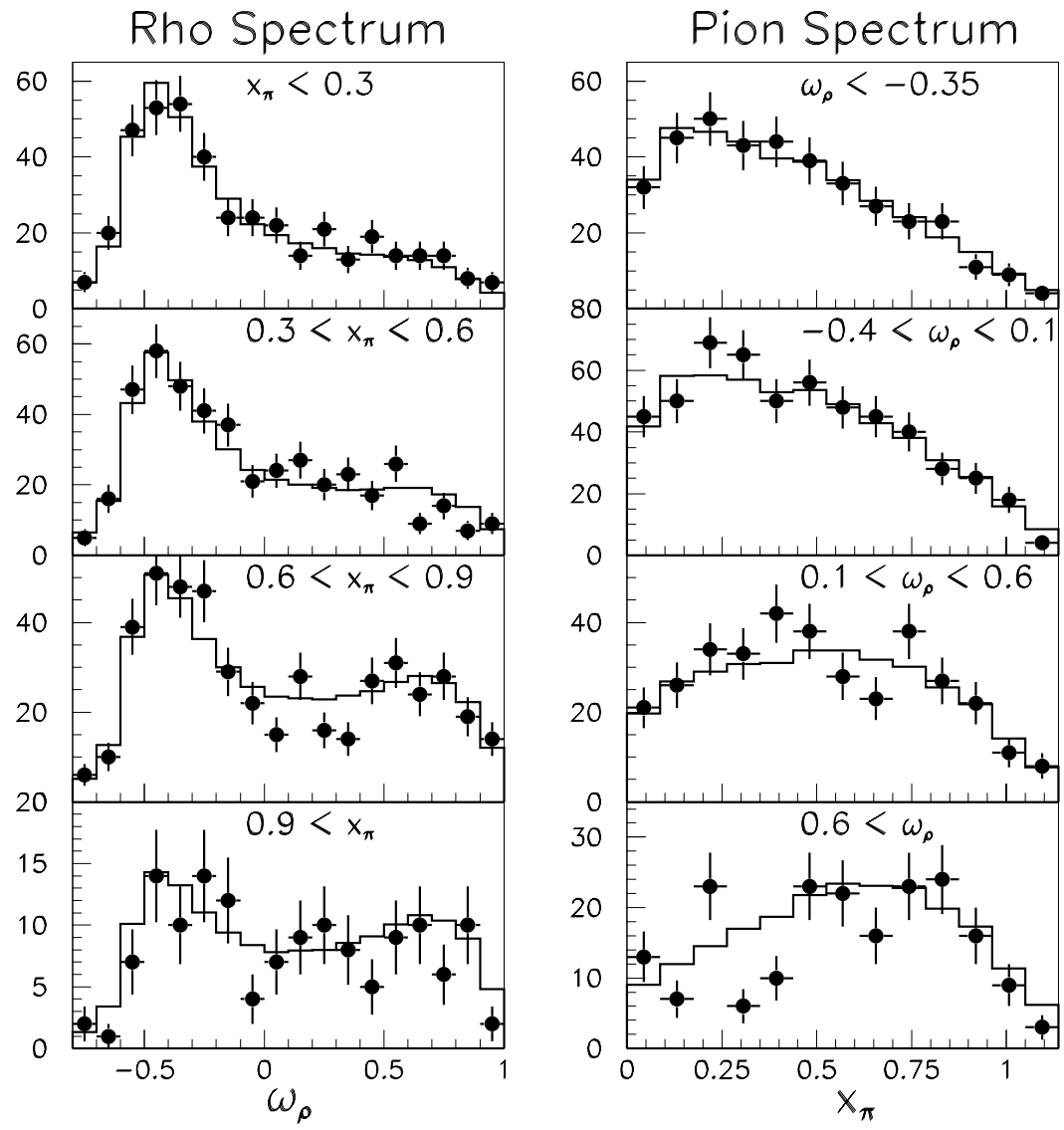

Figure 6.3: The rho and pion spectra for four different slices in distribution of the opposite hemisphere.

Decay	% of Signal
π–e	1.9
π–μ	2.6
π–ρ	7.7
π–a_1	0.6
π–K^*	3.0
π–π	73.0
π–K	8.6
X–X	2.1
Non–τ	0.6

Table 6.5: The composition of the signal in π–π events.

Decay	% of Signal
ρ–e	1.3
ρ–μ	1.4
ρ–ρ	77.3
ρ–a_1	9.9
ρ–K^*	4.0
ρ–π	4.1
ρ–K	0.2
X–X	1.5
Non–τ	0.0

Table 6.6: The composition of the signal in ρ–ρ events.

Decay	% of Signal
ρ–e	1.0
ρ–μ	1.4
ρ–ρ	3.9
ρ–a_1	0.3
ρ–K^*	1.6
ρ–π	75.4
ρ–K	4.4
e–π	0.6
μ–π	0.7
a_1–π	4.8
K^*–π	1.9
π–π	2.0
K–π	0.1
X–X	1.7
Non–τ	0.0

Table 6.7: The composition of the signal in ρ–π events.

	Systematic Error		
Quantity	Branching Ratio	Non–τ Background	Selection
$\mathcal{P}_\tau$	0.0013	0.0009	0.0034
ξ_π	0.0104	0.0046	0.0202
ξ_ρ	0.0022	0.0028	0.0142
$\mathcal{P}_\tau$	0.0013	0.0008	0.0037
ξ_h	0.0041	0.0003	0.0095

Table 6.8: Systematic errors due to statistical fluctuations and selection.

	Systematic Error			
Quantity	$E_{BGO}(\pi^0)$	$E_{BGO}(\pi^\pm)$	$E_{HCAL}(\pi^\pm)$	$E_{TEC}(\pi^\pm)$
$\mathcal{P}_\tau$	0.0036	0.0053	0.0111	0.0065
ξ_π	0.0057	0.0086	0.0200	0.0104
ξ_ρ	0.0027	0.0004	0.0055	0.0066
$\mathcal{P}_\tau$	0.0037	0.0052	0.0108	0.0063
ξ_h	0.0051	0.0039	0.0053	0.0006

Table 6.9: Systematic errors due to energy scale uncertainties in the response of the BGO to electromagnetic clusters and hadronic clusters, the response of the HCAL to hadronic clusters, and the momentum resolution of the TEC.

Chapter 7

Conclusion

The measured values reported in the previous chapter, along with the corresponding statistical and systematic errors are

$$\mathcal{P}_\tau = -0.165 \pm 0.017 \pm 0.015, \tag{7.1}$$

$$\xi_\pi = -1.005 \pm 0.095 \pm 0.034, \tag{7.2}$$

and

$$\xi_\rho = -0.935 \pm 0.067 \pm 0.020, \tag{7.3}$$

where radiative corrections have been included. If we require that the average τ neutrino helicity in $\tau^- \to \pi^- \nu_\tau$ and $\tau^- \to \rho^- \nu_\tau$ should be the same, then we obtain the following:

$$\mathcal{P}_\tau = -0.165 \pm 0.017 \pm 0.015, \tag{7.4}$$

and

$$\xi_h = -0.960 \pm 0.051 \pm 0.012. \tag{7.5}$$

This is in agreement with both the SM and the notion of lepton universality.

Collaboration	Measured ξ_h
L3 (1995)	$-0.960 \pm 0.051 \pm 0.012$
ALEPH (1994)	$-1.006 \pm 0.032 \pm 0.019$
CLEO (1994)	$\|0.99\| \pm 0.06 \pm 0.10$

Table 7.1: Recent measurements of the τ neutrino helicity ξ_h.

Other recent results have been reported by ALEPH and CLEO. These are summarized in table 7.1. The ALEPH measurement included an additional measurement of the Michel parameters for τ leptons [74]. This is a measurement that L3 hopes to incorporate into this work in the near future, however, the combined measurement has the perhaps unsatisfactory feature of allowing τ's to decay solely via V and A currents when the final state is a hadron, versus allowing it to decay by any combination of scalar, pseudoscalar, vector, axialvector, and tensor couplings when the final state is another lepton. The CLEO measurement makes use of correlations between pions in the two hemispheres of the event as does the measurement presented here [75]. CLEO quotes only the magnitude of the τ neutrino helicity because the τ polarization at CESR is zero, thus making it impossible to determine the sign of the neutrino helicity using correlated pion decays.

Clearly from table 7.1 one should conclude that the present measurements of ξ_h are in agreement with the SM. The future of this measurement on L3 looks to be better than a simple improvement in statistical errors. Incorporation of the SMD into the measurement should improve the energy resolution for the charged hadrons and yield a corresponding decrease in systematics. Improved statistics coupled with an improved analysis of the τ branching ratios would also decrease the systematic uncertainties due to branching ratios. In short, this is a measurement

worth performing again with the whole Z data set from 1991 through 1995.

Appendix A

Chirality in $\tau^- \rightarrow \pi^- \nu_\tau$

The purpose of the calculations presented here is illustrate the vector and axial vector couplings in the τ decay. Of particular importance in trying to interpret the results presented in Chapter 6 is the relationship between the decay distributions and the left $(V-A)$ and right–handed $(V+A)$ couplings of the τ.

For the decay of the τ to a π, we have the differential decay rate for the reaction

$$d, = \frac{(2\pi)^4}{2m_\tau}\frac{1}{2E_{k_\tau}}\frac{d^3k_\tau}{(2\pi)^3}\frac{1}{2E_{p_\pi}}\frac{d^3p_\pi}{(2\pi)^3} \tag{A.1}$$

$$\times\delta^4(p_\tau - p_\pi - k_\tau)\sum_{s'_\tau} \mid T \mid^2 .$$

Here the momentum of the pion in the τ rest frame is p_π and its total energy is E_π.

As pointed out elsewhere [27,30], the only four–vector available from the spin–less pion that may be used in forming the transition matrix element is the pion momentum. Thus we have

$$T = f_\pi p_{\pi\mu}\left(\frac{-ig^{\mu\nu}}{q^2 - m_W^2}\right)\bar{\nu}_\tau(k_\tau, s'_\tau)\left(\frac{-ig}{\sqrt{2}}\gamma_\nu\frac{(g_v - g_a\gamma^5)}{2}\right)\tau(p_\tau, s_\tau). \tag{A.2}$$

The unknown factor f_π must be determined from experiment. Here we have also included the possibility that coupling to the τ may be something other than strictly $V-A$. In particular, we may write the charge current coupling above as a sum of left and right-handed currents, where

$$g_v - g_a\gamma^5 = g_L(1-\gamma^5) + g_R(1+\gamma^5). \tag{A.3}$$

Clearly,

$$g_v = g_L + g_R \tag{A.4}$$

and

$$g_a = g_L - g_R. \tag{A.5}$$

Using the above equations,

$$(g_v - g_a\gamma^5)^2 = 2g_L^2(1-\gamma^5) + 2g_R^2(1+\gamma^5). \tag{A.6}$$

Summing over the spins, we obtain the transition matrix element

$$\sum_{s_\tau, s'_\tau} \mid T \mid^2 = \frac{g^2}{8m_W^4} Tr\left(\left(\frac{(1+\gamma^5 \not{s})}{2}\right)(\not{p}_\tau + m_\tau)\not{p}_\pi \not{k}_\tau \not{p}_\pi (g_v - g_a\gamma^5)^2\right), \tag{A.7}$$

where the factor

$$\frac{(1+\gamma^5 \not{s})}{2} \tag{A.8}$$

has been introduced to select the given τ spin. Here $\not{s}$ represents $\gamma^\mu s_\mu$. The three components s_i are the components of the τ spin, and $s_0 = 0$. From equation (A.6) above, we substitute for $(g_v - g_a\gamma^5)^2$ to obtain

$$\begin{aligned} \sum_{s_\tau, s'_\tau} \mid T \mid^2 &= \sum_{s_\tau, s'_\tau} \mid T \mid^2_R + \sum_{s_\tau, s'_\tau} \mid T \mid^2_L \\ &= \frac{g_R^2 g^2}{8m_W^4} Tr\left((1+\gamma^5 \not{s})(\not{p}_\tau + m_\tau)\not{p}_\pi \not{k}_\tau \not{p}_\pi (1+\gamma^5)\right) \\ &+ \frac{g_L^2 g^2}{8m_W^4} Tr\left((1+\gamma^5 \not{s})(\not{p}_\tau + m_\tau)\not{p}_\pi \not{k}_\tau \not{p}_\pi (1-\gamma^5)\right). \end{aligned} \tag{A.9}$$

After plowing through the matrix algebra, this becomes

$$\sum_{s_\tau, s'_\tau} \mid T \mid^2 = \frac{g^2}{2m_W^4} \left[(g_L^2 + g_R^2) \left(2(p_\tau \cdot p_\pi)(k_\tau \cdot p_\pi) - m_\pi^2 (p_\tau \cdot k_\tau) \right) \right. \tag{A.10}$$

$$\left. - m_\tau (g_L^2 - g_R^2) \left(2(s \cdot p_\pi)(k_\tau \cdot p_\pi) - m_\pi^2 (s \cdot k_\tau) \right) \right].$$

This we simplify later, since in the τ rest frame p_τ has no three momenta component.

To perform the integral over all of k_τ, we follow the method presented in [27] and [28] and make the substitution

$$\frac{d^3 k_\tau}{2E_{k_\tau}} = d^4 k_\tau \delta(k_\tau^2) \Theta(E_{k_\tau}). \tag{A.11}$$

Integrating over the unobserved neutrino momentum, we obtain

$$d, \ = \frac{\pi}{m_\tau} \frac{1}{2E_{p_\pi}} \frac{d^3 p_\pi}{(2\pi)^3} \delta(k_\tau^2) \sum_{s'_\tau, s_\tau} \mid T \mid^2, \tag{A.12}$$

where we now have the momentum constraint

$$k_\tau = p_\tau - p_\pi. \tag{A.13}$$

This leads to the following:

$$\begin{aligned} \sum_{s'_\tau, s_\tau} \mid T \mid^2 \ &= \ (g_L^2 + g_R^2) \frac{g^2 m_\tau}{2m_W^4} \left\{ \left(2m_\tau E_\pi^2 - E_\pi m_\pi^2 - m_\tau m_\pi^2 \right) \right. \\ &- \ h_\tau \frac{g_L^2 - g_R^2}{g_L^2 + g_R^2} \left(2m_\tau E_\pi - m_\pi^2 \right) \left(E_\pi^2 - m_\pi^2 \right)^{\frac{1}{2}} \cos\theta \left. \right\}, \end{aligned} \tag{A.14}$$

where θ is the angle between the pion flight direction in the τ rest frame and the line of flight of the τ in the lab frame and h_τ is the τ lepton helicity.

With the neutrino momentum now given by (A.13), the delta function in equation (A.12) becomes

$$\delta(k_\tau^2) = \frac{1}{2m_\tau} \delta \left(E_\pi - \frac{m_\tau^2 + m_\pi^2}{2m_\tau} \right). \tag{A.15}$$

Defining θ as the angle between the pion line–of–flight and the τ spin, we may write the differential over the pion 3-momenta as

$$d^3 p_\pi = 2\pi E_\pi^2 dE_\pi d\cos\theta. \tag{A.16}$$

Putting all of the above together and integrating over the pion energy yields the decay rate

$$\begin{aligned}\frac{d,}{d\cos\theta} &= \frac{g^2 f_\pi^2}{32\pi m_\tau m_W^4}\frac{m_\tau^2 + m_\pi^2}{2m_\tau} \\ &\times \left(g_L^2 + g_R^2\right)\left\{2m_\tau\left(\frac{m_\tau^2+m_\pi^2}{2m_\tau}\right)^2 - m_\pi^2\left(\frac{m_\tau^2+m_\pi^2}{2m_\tau}\right)\right. \\ &- \left. h_\tau\left(\frac{g_L^2-g_R^2}{g_L^2+g_R^2}\right)\left(2m_\tau\left(\frac{m_\tau^2+m_\pi^2}{2m_\tau}\right) - m_\pi^2\right)\left(\left(\frac{m_\tau^2+m_\pi^2}{2m_\tau}\right)^2 - m_\pi^2\right)^{\frac{1}{2}}\cos\theta\right\}.\end{aligned} \tag{A.17}$$

Since $m_\pi \approx 0.14$ GeV and $m_\tau \approx 1.78$ GeV, we now drop all terms on the order of m_π^2/m_τ^2 to obtain

$$\frac{d,}{d\cos\theta} = \frac{g^2 f_\pi^2 m_\tau^3}{128\pi m_W^4}\left(g_L^2 + g_R^2\right)\left\{1 - h_\tau\left(\frac{g_L^2-g_R^2}{g_L^2+g_R^2}\right)\cos\theta\right\}. \tag{A.18}$$

From the equations (A.4) and (A.5) defining g_L and g_R, we find

$$\xi_\pi = -\frac{g_L^2 - g_R^2}{g_L^2 + g_R^2} = -\frac{2g_v g_a}{g_v^2 + g_a^2}. \tag{A.19}$$

Here we dub ξ_π the chirality parameter for the pion.

Boosting to the laboratory frame, i.e. to the Z–peak, we find [30, 76]

$$\cos\theta = \frac{2u - \frac{m_\pi^2}{m_\tau^2} - 1}{(1 - \frac{m_\pi^2}{m_\tau^2})(1 - \frac{m_\tau^2}{E_{beam}^2})} \tag{A.20}$$

where

$$u = \frac{E_\pi^{lab}}{E_{beam}} \tag{A.21}$$

is the normalized pion energy in the lab frame. Again neglecting terms on the order of m_π^2/m_τ^2, we have

$$\cos\theta = 2u - 1. \tag{A.22}$$

Thus in the lab frame the normalized decay rate is

$$\frac{1}{,}\frac{d,}{du} = 1 - \mathcal{P}_\tau \xi_\pi (2u - 1). \tag{A.23}$$

We have also include the average τ polarization $\mathcal{P}_\tau$ due to the coupling at the Z–vertex.

Appendix B

The ρ Dynamics in a Single Variable

Two polarization sensitive variables for the ρ are the cosines $\cos\theta$ (show in figure 3.3) and $\cos\psi$ (shown in figure 3.4). For completeness, we list here the relationships between these variables and the lab frame quantities E_{π^-} and E_{π^0}, the decay distribution in terms of $\cos\theta$ and $\cos\psi$, and the definition of the single variable ω_ρ used in the text. All of these may be found in [41], [46] and [61].

In terms of measurable energies and momenta in the lab frame, the decay angles are given by

$$\cos\theta = \frac{4m_\tau^2}{m_\tau^2 - m_\rho^2}\frac{E_{\pi^-} + E_{\pi^0}}{E_{beam}} - \frac{m_\tau^2 + m_\rho^2}{m_\tau^2 - m_\rho^2} \tag{B.1}$$

and

$$\cos\psi = \frac{m_\rho}{\sqrt{m_\rho^2 - 4m_\pi^2}}\frac{E_{\pi^-} - E_{\pi^0}}{|\vec{P}_{\pi^-} + \vec{P}_{\pi^0}}. \tag{B.2}$$

The decay amplitude in terms of both $\cos\theta$ and $\cos\psi$ may be written in the form

$$\frac{1}{N}\frac{dN}{d\cos\theta d\cos\psi} = (1 - \mathcal{P}_\tau\xi_\rho)W^+(\cos\theta,\cos\psi) + (1 + \mathcal{P}_\tau\xi_\rho)W^-(\cos\theta,\cos\psi), \tag{B.3}$$

where

$$W^{\pm} = w_1^{\pm}(\theta)h_1(\psi) + w_0^{\pm}(\theta)h_0(\psi). \tag{B.4}$$

These terms are all defined by the following:

$$h_0(\psi) = 2\cos^2\psi \tag{B.5}$$

$$h_1(\psi) = \sin^2\psi \tag{B.6}$$

$$w_0^{+}(\theta) = \left[m_\tau \cos\eta \cos\frac{\theta}{2} + m_\rho \sin\eta \sin\frac{\theta}{2}\right]^2 \tag{B.7}$$

$$w_0^{-}(\theta) = \left[m_\tau \cos\eta \sin\frac{\theta}{2} - m_\rho \sin\eta \cos\frac{\theta}{2}\right]^2 \tag{B.8}$$

$$w_1^{+}(\theta) = \left[m_\tau \sin\eta \cos\frac{\theta}{2} - m_\rho \cos\eta \sin\frac{\theta}{2}\right]^2 + m_\rho^2 \sin^2\frac{\theta}{2} \tag{B.9}$$

$$w_1^{-}(\theta) = \left[m_\tau \sin\eta \sin\frac{\theta}{2} + m_\rho \cos\eta \cos\frac{\theta}{2}\right]^2 + m_\rho^2 \cos^2\frac{\theta}{2}. \tag{B.10}$$

The angle η is defined by

$$\cos\eta = \frac{m_\tau^2 - m_\rho^2 + (m_\tau^2 + m_\rho^2)\cos\theta}{m_\tau^2 + m_\rho^2 + (m_\tau^2 - m_\rho^2)\cos\theta}. \tag{B.11}$$

The single variable is formed by expressing equation (B.3) in the form

$$\frac{1}{N}\frac{dN}{d\omega_\rho} = \hat{f}(\omega_\rho)\left(1 - \mathcal{P}_\tau \xi_\rho \omega_\rho\right). \tag{B.12}$$

Where we have used

$$\omega_\rho = \frac{W^+ - W^-}{W^+ + W^-} \tag{B.13}$$

and

$$\hat{f}(\omega_\rho) = \int \left(W^+ - W^-\right)\delta\left(\omega_\rho - \frac{W^+ - W^-}{W^+ + W^-}\right) d\cos\theta\, d\cos\psi. \tag{B.14}$$

Following [41], we also write this as

$$\omega_\rho = \frac{b_0(\theta)h_0(\psi) + b_1(\theta)h_1(\psi)}{a_0(\theta)h_0(\psi) + a_1(\theta)h_1(\psi)}, \tag{B.15}$$

where the a's and b's are defined by

$$a_0(\theta) = m_\rho^2(F-G) + m_\tau^2 G \tag{B.16}$$

$$a_1(\theta) = m_\rho^2(F+G) + m_\tau^2(F-G) \tag{B.17}$$

$$b_0(\theta) = (m_\tau^2 - m_\rho^2)(F-G) + m_\tau^2 F\cos\theta \tag{B.18}$$

$$b_1(\theta) = -(m_\tau^2 - m_\rho^2)(F-G) - 2m_\tau^2 F\cos\theta, \tag{B.19}$$

with F and G given by

$$F(\theta) = \left[m_\tau^2 + m_\rho^2 + (m_\tau^2 - m_\rho^2)\cos\theta\right]^2 \tag{B.20}$$

$$G(\theta) = \left[m_\tau^2 - m_\rho^2 + (m_\tau^2 + m_\rho^2)\cos\theta\right]^2. \tag{B.21}$$

Appendix C

The L3 Plastic Scintillating Fiber System

The L3 Plastic Scintillating Fiber System (PSF) was designed with the purpose of studying the drift velocity and behavior of the TEC. The PSF provides a single external measurement of the track position in the $r - \phi$ plane that remains independent of any changes in the chamber itself. Here we provide an overview of the hardware that constitutes the PSF and describe its use in 1991-93 data for detecting changes in drift velocity in the central tracker.

C.1 PSF Hardware

For each of the 24 outer sectors of the TEC, a PSF ribbon is mounted between the TEC and the Z chamber [66] as shown in figures C.1 and 4.8, along with two multi-anode micro-channel-plate photomultipliers (MCP) and analog readout electronics. The ribbons, consisting of 143 fibers, are approximately 100mm wide, 1.3m long, and 1mm thick. They are instrumented at one end only, by the two

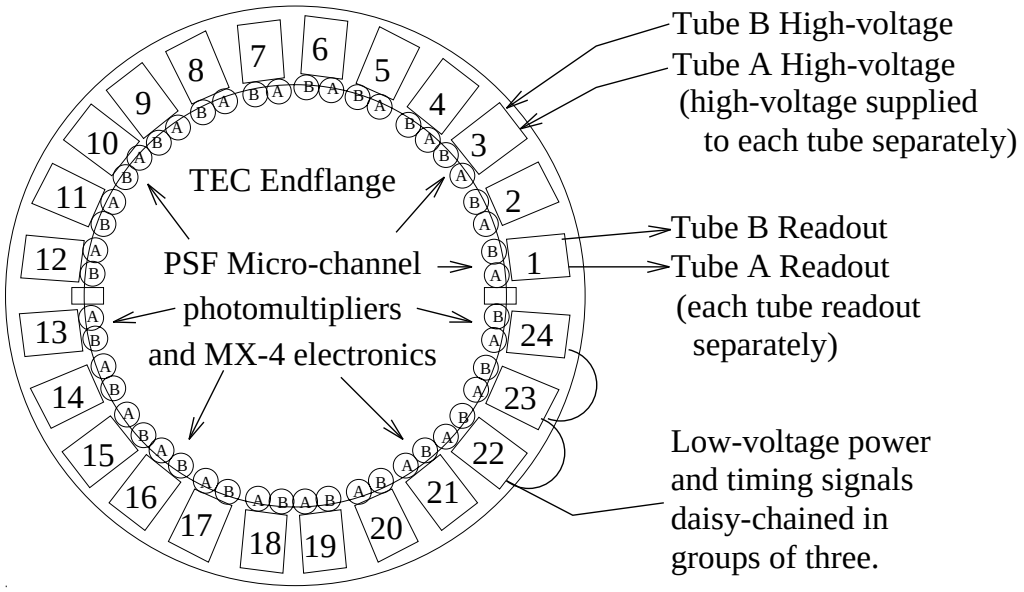

Figure C.1: TEC and PSF endflange view.

MCP tubes. The other end is mirrored to reduce light loss as shown in figure C.2.

On the readout side, the fibers are separated and threaded into two faceplates each having a 10×10 square array of holes. The two faceplates hold fibers 1-72 and 73-143, leaving 28 and 29 free holes respectively. The possibility that fibers have been misthreaded was examined by matching PSF hits to TEC tracks in real data from 1990 and '91. Those fibers determined to be misthreaded are listed in table C.1. The misthreading is corrected for in this analysis. Each faceplate is optically coupled to an MCP tube. This interface must be carefully aligned to ensure the correct fiber-anode correspondence. Each of the 48 tubes are read out via a multiplex amplifier chip (MX–4).

The analog signal generated is a measure of the charge collected in each channel of the MCP during a window in time defined by two gates, S1 and S2. These are

Sector	Nominal fiber no.	Actual fiber no.	Comment
2	82	77	fiber misthreaded →
	78→81	79→82	sequence error
8	63	64	Two fibers swapped
	64	63	
9	55	56	Two fibers swapped
	56	55	
16	73→121	74→122	Threading out of sequence
17	133	134	Two fibers swapped
	134	133	
	135	136	Two fibers swapped
	136	135	

Table C.1: Faceplate fiber threading errors

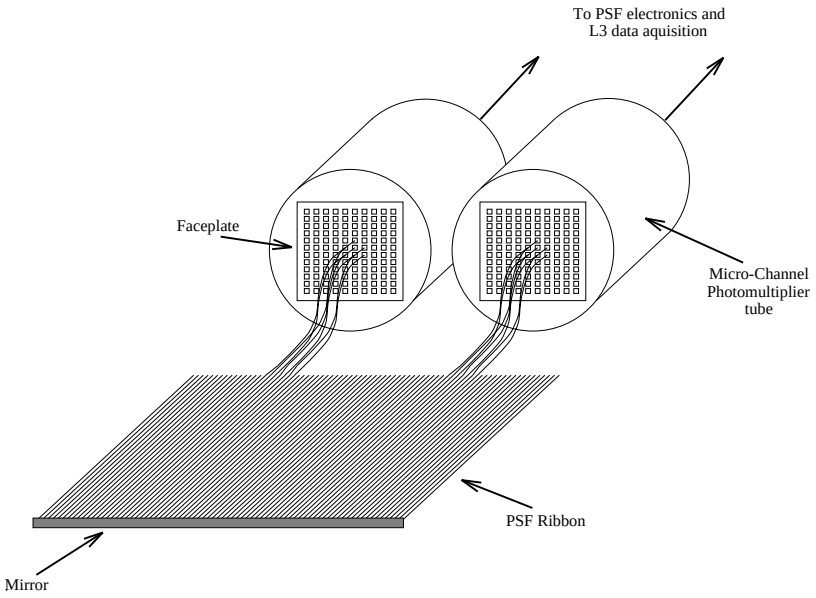

Figure C.2: PSF Ribbon and Micro–Channel Photomultiplier Tubes.

generated by the PSF readout electronics located in the U1 blockhouse and are accompanied by a RESET signal, which clears the analog electronics for the next event. A typical timing diagram for these gates is shown in figure C.3, with LEP operating in 8×8 bunch mode. An event is read out if a trigger-level-1-yes (TL1Y) is received before the end of RESET.

The signal from each MX–4 is fed into an A/D converter in the U1 blockhouse, shown in figure C.4. There are 24 A/D boards, each of which handles two MX–4 chips and thus a single PSF ribbon. The A/D boards store in memory the analog signals from a single reference event, establishing a pedestal level for each PSF fiber which is subtracted in all subsequent events. The commands to reset the electronics and load a new reference event are issued via the terminal console located beneath the readout electronics in the blockhouse. As shown in table C.2, the commands

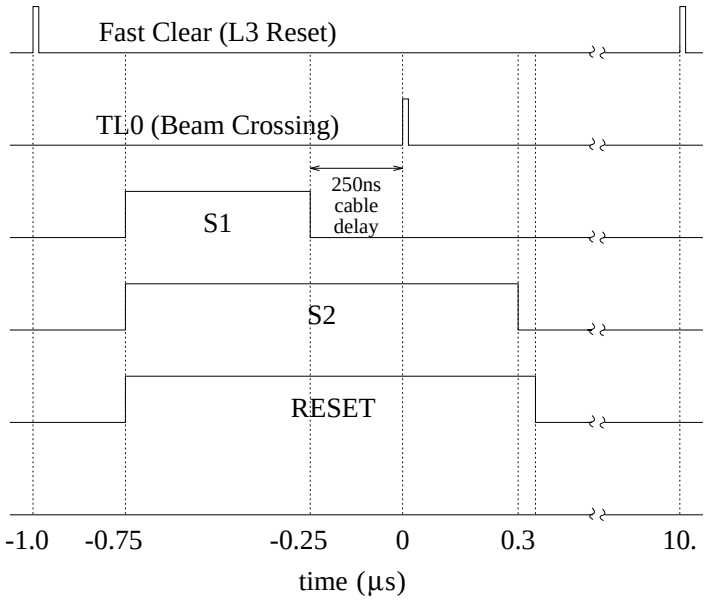

Figure C.3: PSF timing signals.

instruct the A/D boards to select a signal-above-pedestal threshold from either (a) the master threshold or global threshold shown in figure C.4 or (b) the sector-by-sector dip switches located on each A/D board. A fiber is considered to be hit if

Global Threshold		Sector by Sector Threshold	
W015C	Store Pedestals	W015C	Store Pedestals
W02F6	Select Master Threshold	W02FE	Select Dip Switchs
W0106	Run	W0106	Run

Table C.2: PSF Console Commands and Run Modes

its signal-above-pedestal exceeds the threshold setting. A single bit is set for each fiber according to whether or not it was hit. No pulse height information is stored.

The PSF readout system is described in more detail elsewhere. [77]

As shown in figure 4.8, each of the 24 PSF ribbons covers 83% [77] of a sector in azimuth. The fibers have a polystyrene base doped with 1% butyl-PBD and 0.02% BDB. The pitch of the fibers, defined as the distance between equivalent points of neighboring fibers, is nominally 700μm[1], giving a total ribbon width of 100.1mm. Each fiber has an active width of 530μm and is surrounded by opaque cladding (to prevent crosstalk) and glued to the adjacent fibers. The manufacturer, namely The Kyowa Gas Company of Japan, has estimated that the position of the active fiber element may fluctuate by up to 35μm within any fiber + cladding + glue unit of width 700μm.

Each ribbon is glued to a G10 mount which is attached to four mounting blocks fixed to the outer cylinder of TEC, as shown in figure C.5. The space between the ribbon and the outer casing of the mount is used for signal and control cables serving the high-voltage side of the TEC, *e.g.* for the temperature control system. Nominally, the ribbon is parallel to the z-axis and perpendicular to the extrapolated outer TEC anode plane which intersects the center of the ribbon. The ribbon, of width 100.1mm, is glued to the edge of the G10 bed of width 102mm. This results in a lateral offset of almost 1mm compared to the nominal geometry. There may be additional offsets from uncertainties in the mounting procedure. The G10 between the TEC cylinder and the PSF ribbon is 2mm thick. Thus, given $r_{TEC} = 456.75 \pm 0.50$mm, the PSF radius measured along the anodes to the center of the fibers is $r_{PSF} = (459.25 \pm 0.50)$mm.

[1]Measured to be 697μm $\pm$ 2μm by *ETH Zürich*.

C.2 Drift Velocity Monitoring

The calibration of the L3 central tracker, the TEC, assumes that the TEC is essentially linear outside of the amplification region between the two grids shown in figure C.6. The measured quantity in the TEC is the time, t_{hit}, it takes for the ionization due to a charged particle to reach the anodes. The distance, d, from the anode to the track then has the simple form

$$d_{hit} = d_{grid} + (t_{hit} - t_{grid}) \cdot v_{drift}, \tag{C.1}$$

where d_{grid} is the effective distance from the anodes to the grid plane, t_{grid} is the time required for the ionized electrons to drift from the grid plane to the anodes, and v_{drift} the drift velocity of the ionization electrons used in reconstructing the particle track.

To a first approximation, the distance from the anodes at which a reconstructed track crosses the PSF ribbon, as shown in figure C.6, is also linear in drift time, and the distance between a reconstructed track and the PSF hit generated by the particle, denoted the *track residual* r, can be expressed as

$$r = (n_{hit} - n_{anode}) \cdot pitch - [d_{grid} + (t_{hit} - t_{grid}) \cdot v_{drift}]\,. \tag{C.2}$$

Here, n_{hit} and n_{anode} are, respectively, the number of the fiber hit by the particle and the number of the fiber lined up the with anodes. The $pitch$ above is simply the distance from fiber to fiber. For odd outer half-sectors of TEC, d_{grid}, t_{grid} and t_{hit} are defined to be negative while for even outer half-sectors they are positive.

To obtain the error on v_{drift}, the finite derivative with respect to fiber number is taken to obtain

$$\frac{\triangle r}{fiber} = pitch - v_{drift}\frac{\triangle t}{fiber}, \tag{C.3}$$

where $\triangle t$ is the time required for ionized electrons to drift over a length corresponding to the fiber pitch. Division by *pitch* leads to

$$\frac{\triangle r}{pitch} = 1 - \frac{v_{drift}}{v_{actual}}. \tag{C.4}$$

Here the relationship

$$v_{actual} = \frac{pitch}{\triangle t} \tag{C.5}$$

has been used.

The interesting quantity above is the correction factor

$$g_{shift} = \frac{v_{actual}}{v_{drift}} = \frac{1}{1 - \frac{\triangle r}{pitch}} \tag{C.6}$$

that must be applied to the drift velocity used in reconstruction. This quantity has been dubbed the g_{shift} by L3, since its first application was to correct for shifts in the gas pressure in the TEC in 1992. With this correction, equation C.1 becomes

$$d_{hit} = d_{grid} + (t_{hit} - t_{grid}) \cdot v_{drift} \cdot g_{shift}, \tag{C.7}$$

with the assumption that any changes in t_{grid} due to small changes in drift velocity are undetectable.

In practice, the measurement of g_{shift} is accomplished in the following way. First, a sample of tracks within 5mm of a PSF hit are collected and grouped on a Fill-by-Fill basis. A second pass is made over the sorted tracks with the requirement that the tracks be within 2mm of a PSF hit. Here, the inner-TEC hits and the last 3 outer-TEC hits are not used in determining the track trajectory. These tracks are then divided into time groups with a minimum of 15,000 tracks per group and a minimum of one hour between the last track in one group and the first track in the next.

Within each time group, the track residual for each PSF hit is calculated and binned in terms of distance from the anode rather than fiber number. This allows all sectors to be folded together with the use of the alignment corrections determined previously [78]. Groups of bins are then formed so that each group contains a given minimum number of hits. Usually this minimum is set to either 250 or 500 hits, with the exception that all hits between the grid planes are placed in a single group regardless of their number. The position of the group is then simply taken to be the average position of the fiber hits within the group. The track residuals in each group are fit with the following function to obtain their central value:

$$f(r) = a + b \cdot exp\left(\frac{-(r - r_\circ)^2}{2\sigma^2}\right). \tag{C.8}$$

This yields a set of discrete points for the value of the track residual versus distance from the anodes.

For each half-sector, i.e. for each side of the anode plane, the points determined above are fit separately with a straight line of the form

$$r(x) = r_{miss} + \frac{\triangle r}{pitch} \cdot x, \tag{C.9}$$

where x is the distance from the anode and is defined to be negative for odd outer TEC half-sectors and positive for even outer TEC half-sectors. The quantity r_{miss} should ideally be zero. As may be seen from equation C.2, non-zero values of r_{miss} may arise from errors in PSF alignment, i.e. n_{anode}, errors in the effective distance to the grid, d_{grid}, or errors in the drift time from the grid to the anodes, t_{grid}. The point between the grid planes is excluded in both fits as well as the first point outside of the grid planes, since this first point may be shifted due to the same errors discussed above. Typical fits for both the residuals in a given fiber group and for the residuals in a given time group are shown in figure C.7. For 1991, '92,

and '93 data, the measurement of $\frac{\triangle r}{pitch}$ versus fill number has been made using PSF. The resulting g_{shift} has been plotted for these years. These results are shown in figures C.8, C.9 and C.10.

The largest source of uncertainty in this measurement is the *pitch* of the PSF fibers. For the data presented in figures C.8 through C.10, the pitch was set to the *ETH* measured value of $697\mu m$. An error in the pitch simply shifts the measurement of g_{shift} up or down. This represents an 0.4% shift in pitch and is $1\mu m$ larger than the error quoted in the *ETH* measurement of $697\mu m \pm 2\mu m$. As expected, the 0.4% change in pitch results in a shift of 0.4% in the measured g_{shift}. Since this source of error causes all points in the plots presented to move up or down together, and since the real interest here is in the change of drift velocity as a function of time, this source of error has not been included in the error bars shown.

The work presented here was essential in sorting out which of two pressure gauges provided the correct readings for the TEC gas pressure in 1992. This work also provided clear indications of the time scale over which the calibration of the central tracking should be performed. In addition, the results from 1993 were the first indication of a problem in the early part of the year. Thus the PSF has proven important as an external test of changing conditions within the TEC.

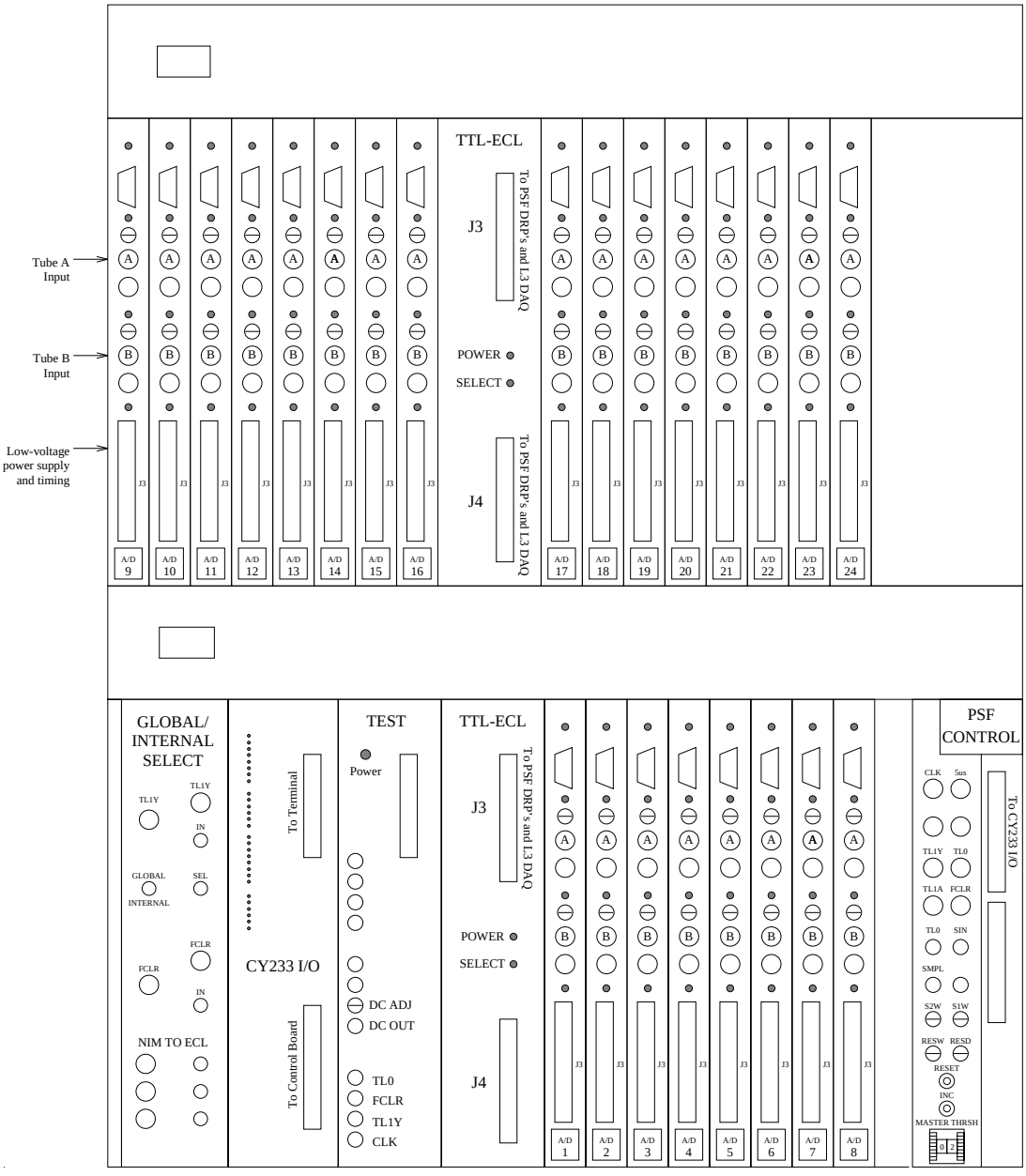

Figure C.4: PSF VME Crate.

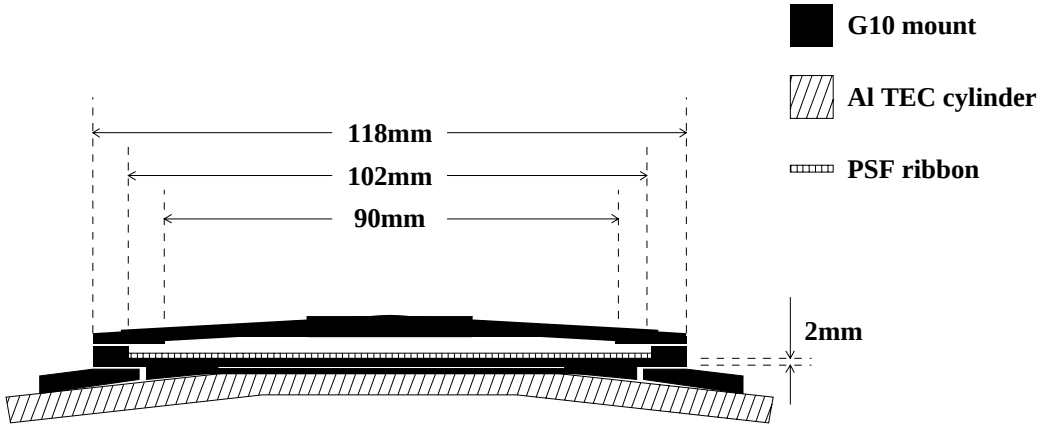

Figure C.5: PSF G10 mount.

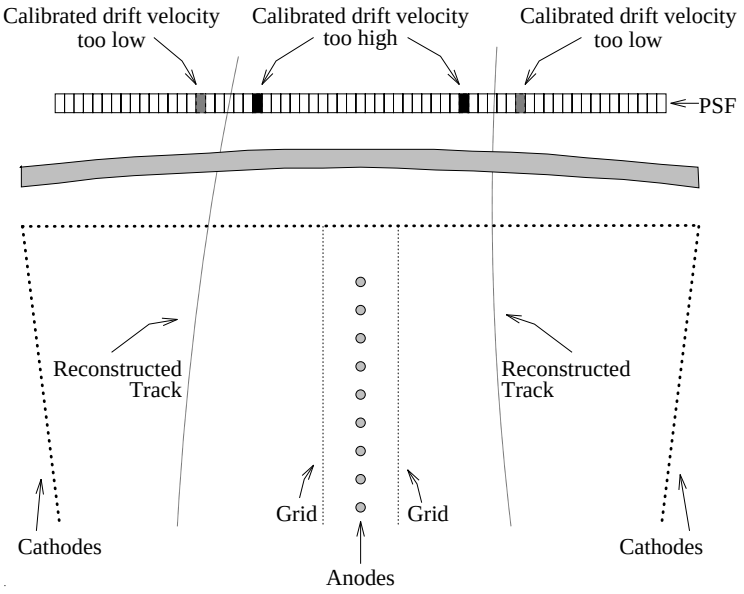

Figure C.6: PSF hits and drift velocity errors.

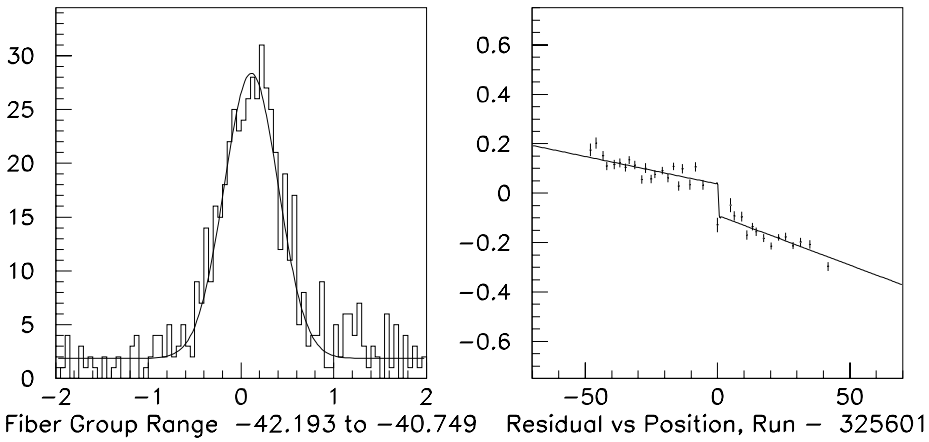

Figure C.7: Fit to PSF residuals for one fiber group and for one time group.

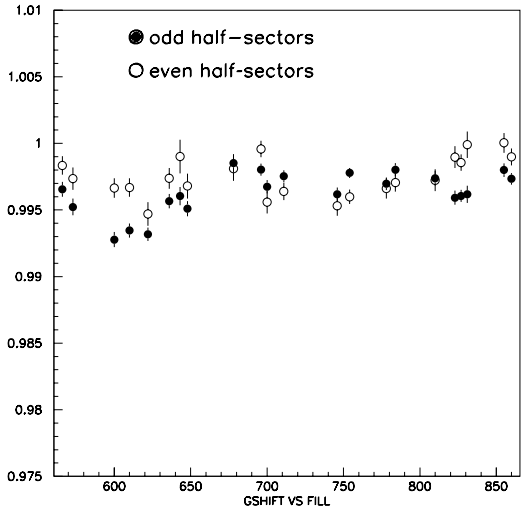

Figure C.8: 1991 drift velocity correction factor versus fill.

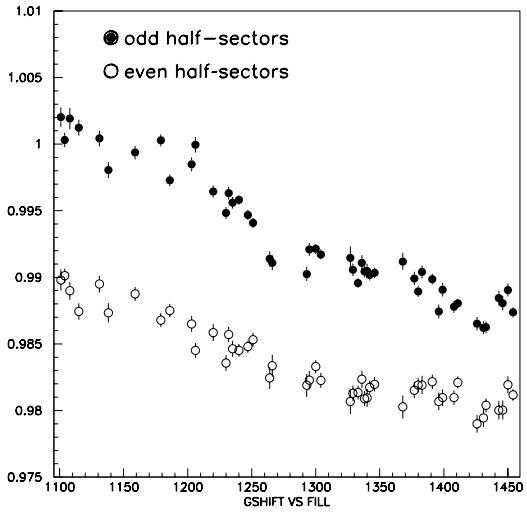

Figure C.9: 1992 drift velocity correction factor versus fill.

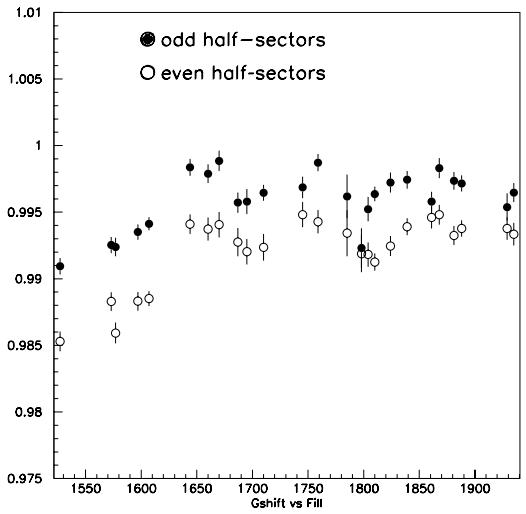

Figure C.10: 1993 drift velocity correction factor versus fill.

Appendix D

The L3 τ-group Software Package

In 1994, the L3 Collaboration began shifting its computer usage from an Apollo cluster to new HP RISC machines, SGI workstations, and an SGI Challenge mainframe. In moving the τ group software from the Apollo's to the HP's and SGI's, the decision was made to consolidate the existing software into a single, user friendly package. The result of this effort was dubbed the *col3* analysis package.

The first version of this software has been documented in L3 Note 1665. Documentation for subsequent versions exists on the L3 HP cluster in the directory */l3/anal/tau/doc*. Copies may be obtained from either J. Gerald or D. Kim.

The original version contained almost no changes in the event selection or reconstructed quantities other than those FORTRAN changes required by the new compilers. The τ software on the Apollo's embodied in *sele.car* and *spol.car* migrated to the HP's as *sel3v300* and *spl3v300* respectively. The most current version incorporates the most recent enhancements of the selection software.

The user interface, through which one controls the selection of events and the information output for each event, has proven to be versatile enough to satisfy

the needs of the τ polarization group. Individual decay channels of the τ may either be selected or deselected. Within each selection, the final cuts against non–τ backgrounds may be turned on or off. The information output is grouped into 24 predefined banks plus one user defined bank, each of which may be turned on or off event–by–event.

This last feature was made possible by changing the data structure from the original row–wise ntuple format to the new column–wise ntuple format. This new format provides room for the extension of the τ analysis at L3 to 3–pronged decays of the τ. It also provides for the addition of SMD information for 1994 data and beyond and for the compression of the present data set into a smaller space.

This software formed the backbone for the selection studies, background studies, and detector studies conducted for the measurement presented in Chapter 6. It is the author's hope that the next set of students will find the *col3* analysis package just as useful as he did.

Bibliography

[1] S. Glashow, *Nucl. Phys.*, **22**, (1961) 579.
S. Weinberg, *Phys. Rev. Lett.*, **19** (1967) 1264.
A. Salam and J. C. Ward, *Phys. Lett.*, **13**, 168 (1964).

[2] C. S. Wu *et al.*, *Phys. Rev.* **105**, 1413 (1957).

[3] R. W. Birge *et al.*, *Phys. Rev.*, **99**, 329 (1955).

[4] W. W. Chupp *et al.*, *Phys. Rev.*, **99**, 1042 (1955).

[5] E. L. Iloff *et al.*, *Phys. Rev.*, **99**, 1617 (1955).

[6] L. W. Alvarez and S. Goldhaber, *Nuovo Cimento IV*, **X,2**, 33 (1956).

[7] L. W. Alvarez *et al.*, *Phys. Rev.*, **101**, 503 (1956).

[8] V. Fitch and R. Motley, *Phys. Rev.*, **101**, 496 (1956).

[9] R. N. Cahn and G. Goldhaber, "The Experimental Foundations of Particle Physics," Cambridge University Press, 1989.

[10] R. L. Garwin *et al.*, *Phys. Rev.*, **105**, 1415 (1957).

[11] J. I. Friedman and V. .L. Telegdi, *Phys. Rev.*, **105**, 1681 (1957).

[12] H. Frauenfelder *et al.*, *Phys. Rev.*, **106**, 386 (1957).

[13] M. Goldhaber *et al.*, *Phys. Rev.*, **109**, 1015 (1958).

[14] M. T. Burgy *et al.*, *Phys. Rev.*, **120**, 1829 (1960).

[15] F. Reines and C. L. Cowan, Jr., *Phys. Rev.*, **113**, 273 (1959).

[16] G. Danby *et al.*, *Phys. Rev. Lett.*, **9**, 36 (1962).

[17] J. J. Aubert *et al.*, *Phys. Rev. Lett.*, **33**, 1404 (1974).

[18] J.-E. Augustin *et al.*, *Phys. Rev. Lett.*, **33**, 1406 (1974).

[19] M. L. Perl *et al.*, *Phys. Rev. Lett.*, **35**, 1489 (1975).

[20] S. W. Herb *et al.*, *Phys. Rev. Lett.*, **39**, 252 (1977).

[21] UA 1 Collab., *Phys. Lett.*, **122B**, 103 (1983).
UA 1 Collab., *Phys. Lett.*, **126B**, 398 (1983).
UA 1 Collab., *Phys. Lett.*, **134B**, 469 (1984).
UA 1 Collab., *Phys. Lett.*, **147B**, 241 (1984).
UA 1 Collab., *Phys. Lett.*, **166B**, 484 (1986).

[22] UA 2 Collab., *Phys. Lett.*, **122B**, 476 (1983).
UA 2 Collab., *Phys. Lett.*, **129B**, 130 (1983).
UA 2 Collab., *Phys. Lett.*, **186B**, 440 (1987).

[23] CDF Collab. FERMILAB-PUB-95-022-E (1995).

[24] D0 Collab. FERMILAB-PUB-95-028-E (1995).

[25] L3 Collab., *Phys. Lett.*, **B292**, 463 (1992).
L3 Collab., *Phys. Lett.*, **B275**, 209 (1992).

[26] E. Fermi, *Nuovo Cimento*, **11**, 1 (1934).
E. Fermi, *Z. Phys.*, **88**, 161.

[27] O. Nachtmann, "Elementary Particle Physics," Springer-Verlag (1989).

[28] I.J.R. Aitchison and A.J.G. Hey, "Gauge Theories in Particle Physics," Adam Hilger (1989).

[29] K. Grotz and H. V. Klapdor, "The Weak Interaction in Nuclear, Particle, and Astrophysics," Adam Hilger (1990).

[30] F. Halzen and A. D. Martin, *Quarks and Leptons*, John Wiley & Sons, New York (1984).

[31] J. D. Bjorken, *Relativistic Quantum Mechanics*, MacGraw–Hill, New York (1964).

[32] O. Adriani *et al.*, " A Measurement of τ Polarization", L3 Note 1637 (1994).

[33] L3 Collaboration, M.Acciarri *et al.*, *Phys. Lett.* **B341** (1994) 245.
L3 Collaboration, O.Adriani *et al.*, *Phys. Lett.* **B294** (1992) 466.

[34] J. Gerald *et al.*, "A Preliminary Measurement of $\mathcal{A}_\tau$ and $\mathcal{A}_\mathrm{e}$ Using 1994 Data", L3 Note 1793 (1995).

[35] ALEPH Collaboration, D. Buskulic *et al.*, *Z. Phys.* **C59** (1993) 369.

[36] DELPHI Collaboration, P. Abreu *et al.*, *Z. Phys.* **C55** (1992) 555.

[37] OPAL Collaboration, R. Akers *et al., Z, Phys.* **C56** (1995) 1.
G. Alexander, *et al.*, *Phys. Lett.*, **B266** (1991) 201.

[38] SLD Collaboration, K. Abe *et al.*, *Phys. Rev. Lett.*, **70** (1993) 2525.

[39] Particle Data Group, L. Montanet *et al.*, Review of Particle Properties, *Phys. Rev.*, **D50** (1994) 1173.

[40] G. Altarelli *et al.*in "Z Physics at LEP 1, Volume 1: Standard Physics," report CERN 89-09 (1989).

[41] M. Davier *et al.*, *Phys. Lett.*, *B 306* (1993) 411.

[42] Y. Tsai, *Phys. Rev.*, *D4*, (1971) 2821.

[43] C. Nelson, *Phys. Rev.*, **D40**, (1989) 123; *Erratum: Phys. Rev.*, **D41**, (1990) 2327.

[44] W. Fetscher, *Phys. Rev.*, **D42**, (1991) 1544.

[45] K. Mursula, M. Roos, and F. Scheck, *Nucl. Phys.* **B219**, (1983), 321.

[46] K. Hagiwara, *et al.*, *Phys. Lett.*, **B235**, (1990), 198.

[47] ARGUS Collaboration, H. Albrecht *et al.*, *Phys. Lett.*, **B250** (1990) 164.
ARGUS Collaboration, H. Albrecht *et al.*, *Z. Phys.***C58** (1993) 61.

[48] D. Bardin *et al.*, FORTRAN package ZFITTER; CERN–TH 6443/92.
D. Bardin *et al.*, *Z. Phys.***C44** (1989) 493.
D. Bardin *et al.*, *Nucl. Phys.* **B351** (1991) 1.
D. Bardin *et al.*, *Phys. Lett.*, **B255** (1991) 290.

[49] S. Kirsch, Ph.D. thesis, University of Berlin (1994).

[50] C.M.G. Lattes *et al.*, *Nature* **160** (1947) 453.

[51] L. Michel, *Proc. Phys. Soc.* **A63**, (1950) 514.

[52] W. Dudziak *et al.*, *Phys. Rev.*, **114** (1959) 336.

[53] D. Fryberger, *Phys. Rev.*, **166**, (1968) 1379.

[54] P. C. Macq *et al.*, *Phys. Rev.*, **112** (1958) 2061.

[55] D. M. Schwartz, *Phys. Rev.*, **162**, (1967) 1306.

[56] H. Burkard *et al.*, *Phys. Lett.*, **B160**, (1985) 343.

[57] A. Jodidio *et al.*, *Phys. Rev.*, **D34**, (1986) 1967.

[58] B. Balke *et al.*, *Phys. Rev.*, **D37**, (1988) 587.

[59] S. R. Mishra, *Phys. Lett.*, **B252**, (1990) 170.

[60] CHARM II Collab. *Phys. Lett.*, **B247**, (1990) 131.

[61] A. Rougé, Workshop on Tau Lepton Physics, Orasy 1990, *Editions Frontières* (1991) 213.
A. Rougé, *Z. Phys.*, **C48** (1990) 45.

[62] P. R. Bevington, *Data Reduction and Error Analysis for the Physical Sciences*, **McGraw–Hill Book Company**, New York (1969).

[63] F. James, MINUIT Reference Manual, CERN Program Library, long writeup D506 (1992).

[64] LEP design report, " The LEP injector chain," CERN-LEP/TH/83-29 vol. I (1983)
LEP design report, "The LEP main ring," CERN-LEP/TH/84-01 vol. II (1984).

[65] P.J. Franzini *et al.*in "Z Physics at LEP 1, Volume 2: Higgs Search and New Physics," report CERN 89-09, G. Altarelli, R. Kleiss and C. Verzegnassi Ed. (1989).

[66] L3 Collab., B. Abeva etal., "The construction of the L3 detector at LEP", *Nucl. Inst. Meth.* **A 289**, 35 (1990).

[67] F. Beissel *et al.*, *Nucl. Inst. Meth.* **A332** (1993) 33.

[68] R. Sumner *et al.*, *Nucl. Inst. Meth.* **A265** (1988) 252.

[69] L3 Collab., O. Adriani *et al.*, *Physics Reports* **236** Nos. 1 & 2 (1993).

[70] J. Swain and L. Taylor, "L3 Computing Guide," Vers. 1, (1993) 290.

[71] S. Jezequel and Y. Karyotakis, L3 Note 1272 (1992).

[72] L3 Collaboration, B. Adeva *et al.*, *Phys. Lett.*, **B265** (1991) 451.

[73] L3 Collaboration, A. Acciari *et al.*, *Phys. Lett.*, **B345** (1995) 93.

[74] Aleph Collaboration, D. Buskulic *et al.*, *Phys. Lett.*, **B346** (1995) 379.

[75] CLEO Collaboration, R. Balest *et al.*, CLEO–CONF–94 (1994).

[76] T. C. Paul, Ph.D. Thesis, Johns Hopkins University (1994).

[77] H. Akbari *et al.*, *Nucl Instr. and Meth.* **A 302** (1991) 415-426.

[78] G. Alverson *et al.*, L3 Note **1105** (1992).